Structural studies of BK ion channel in a lipid environment

Lige Tonggu

A dissertation

submitted in partial fulfillment of the

requirements for the degree of

Doctor of Philosophy

University of Washington

2018

Reading Committee:

Liguo Wang, Chair

Sharona Gordon

Wenqing Xu

Program Authorized to Offer Degree:

Molecular and Cellular Biology

University of Washington

Abstract

Structural studies of BK ion channel in a lipid environment

Lige Tonggu

Chair of Supervisory Committee:

Assistant Professor Liguo Wang

Department of Biological Structure

Membrane proteins carry out a variety of functions, including transport, signal transduction, and a variety of metabolic pathways. For human beings, around 18.5% proteins are membrane proteins and they play important roles. However, according to the membrane protein database by Stephen White[1], only about 200 unique membrane protein structures had been identified before the start of my study. This is mainly due to the technical challenges associated with expressing membrane proteins in large quantities, solubilizing them in appropriate detergents and crystallizing them for X-ray crystallography[2]. Cryo-Electron Microscopy has emerged as a powerful method for structural studies of membrane proteins. A central goal of my graduate research was to determine the structure of the human large-conductance voltage- and Ca^{2+} -activated potassium (hBK) channel in a lipid environment using cryo-EM. To restore the asymmetric lipid membrane environment of membrane proteins, a method called "random spherically constrained" (RSC) single-particle cryo-EM was developed. Voltage-gated ion

channels sense the changes in membrane potential and undergo conformational changes that regulate ion flux across membranes in excitable cells. Due to the lack of methods to apply transmembrane potentials for structural studies, the mechanism under which voltage-gated ion channels respond to the voltage change across the membrane is not fully understood. The liposome system I am using can establish a native lipid environment for membrane proteins and make it possible to apply transmembrane potentials to trap voltage-gated ion channels in desired functional states for structural analysis. An intermediate state of hBK was determined in my study to 3.5 Å resolution. Overall, my graduate research has increased our knowledge of the human BK channels and developed the sample preparation pipeline for RSC cryo-EM method. More broadly, this work lays the foundation of transmembrane voltage manipulation at the grid level and will provide insights into other voltage-gated channels.

Acknowledgements

First, I would like to thank my mentor Dr. Liguo Wang for his close mentorship at every step of this challenging project and all the support he gave me through the stressful period in the graduate school. I leave having learned a great deal of bench work and data analysis from Dr. Wang, in general about how to design experiments logically and conduct experiments cautiously.

Next, I would like to thank my committee members: Dr. Kelly Lee, Dr. Ning Zheng, Dr. Sharona Gordon and Dr. Wenqing Xu. They bore with me when my experiments got stuck and gave me insightful suggestions to guide me though graduate school. Dr. Kelly Lee also allowed me to gain access to Vitrobot in his lab, which is a great aid for the reproducibility for my project. Dr. William Zagotta was in my committee panel in the first year but was reassigned due to conflict of interests. I want to thank Dr. Zagotta for many helpful discussions and for allowing me gain access to fluorometer.

I would also like to thank the other members of Wang Lab, both past and current. Lan Tang and Mo Li taught me how to culture cells and purify proteins. And discussion with Xi Zhan and Weibin Zhou were also inspiring.

I also appreciate the technical support from Joel Quispe at UW Biochemistry Cryo-EM center and Yanxiang Cui at UCLA Electron Imaging Center. The work would not have been done without the excellent equipment, service and helpful cryo-EM community.

Last but not least, I would like to thank Dr. John Clark and Dr. Hong Shen for their precious advice both on research and on life. Also special thanks to my collaborators, Dr. Fred Sigworth and Dr. Goragot Wisedchaisri.

List of Tables

List of Figures

Table of Contents

Chapter 1. Introduction to BK ion channel

1.1 Potassium Ion Channel Family

Potassium ion channels allow potassium ions but not sodium ions to cross the cell membrane. Over 100 members are found in this family in eukaryotic, eubacterial as well as archaeal genomes[3,4]. And they respond to different physiological signals, such as a change of membrane potential and calcium concentration[3, 5]. The potassium channels are one of the most diverse ion channels due to the large number of genetic codes, splicing of mRNA, heteromeric assembly as well as post-translational modification[6]. They can be further divided into many molecular subfamilies, such as voltage-gated, calcium-activated, inwardly rectifying and tandem pore domain potassium ion channels.

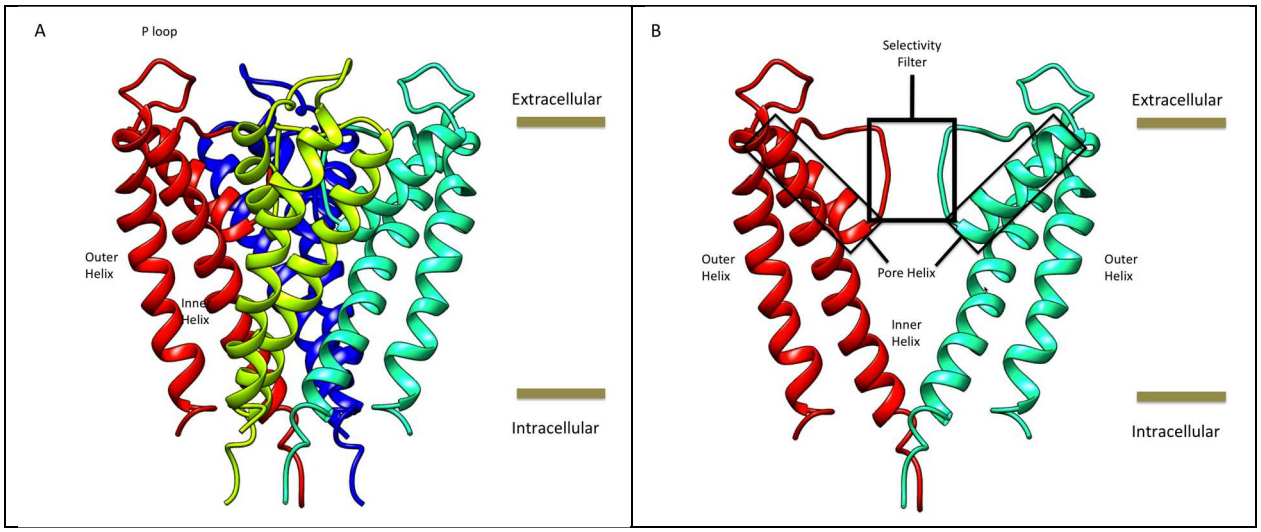

Figure 1.1 Ribbon representation of 2TM/P structure from KcsA (protein data bank PDB accession code 1BL8)[5]. (A) Four α subunits are shown in red, green, cyan and blue. (B) Only two opposing α subunits are shown in red and cyan for clarity. Structural representations in all figures were generated using UCSF Chimera[7].

A typical potassium channel is composed out of four primary subunits (also called α subunits) as shown in Figure 1.1.A. Four of them comprise a pore allowing ions to cross the membrane. The pore domain is conserved between all potassium channels from bacteria to human[8] and

responsible for ion selectivity[5]. The trademark architecture of the α subunits is two transmembrane helices and a membrane reentrant P-loop between them[9]. As Figure 1.1.B shows, each 2TM/P has one outer helix and one inner helix connected by a P-loop. The P-loop has an N-terminal extracellular linker following the outer helix, a pore helix, a short turn exposed to the cavity inside of the pore, a pore-facing selectivity filter region, and a linker between the selectivity filter region and the inner helix. A remarkably conserved signature sequence (-TXXTXGYG-) has been found in more than 50 potassium channels[4,5] in the selectivity filter region. The P-loop only goes halfway through the cell membrane while the other two helices span the entire membrane.

Based on membrane topology, potassium ion channels can be classified into four distinct structural groups (see Figure 1.2.A). The 6TM/P group has six transmembrane segments and one P-loop. It includes voltage-gated potassium channels (Kv) and calcium-activated potassium channels. Both amino and carboxyl terminals are intracellular for the 6TM/P group. The 2TM/P group has two transmembrane segments and one P-loop, including the inward rectifiers (IRK), the adenosine triphosphate (ATP)-dependent K^+ channels (KATP) and bacterial K^+ channels. The 4TM/2P group is composed of four transmembrane segments and two P-loops. The 8TM/2P channels consist of eight

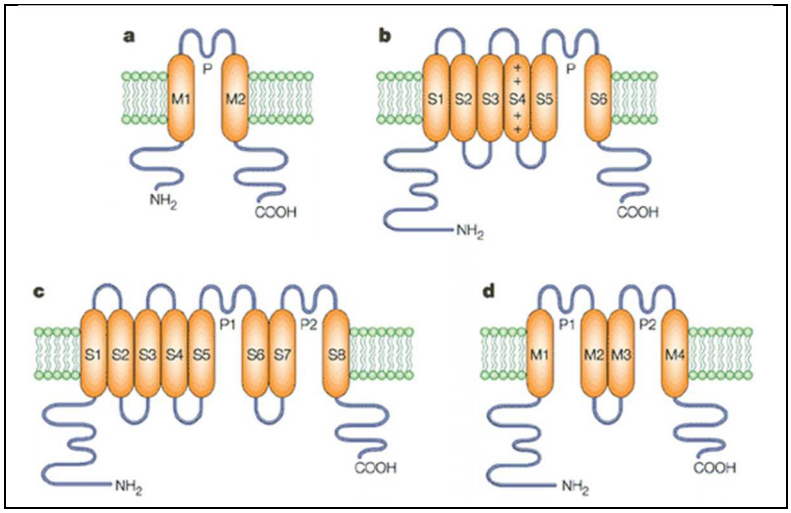

Figure 1.2 Classification of potassium channels α subunits[9]. (a) 2TM/P channels (b) 6TM/P channels (c) 8TM/2P channels (d) 4TM/2P channels.

transmembrane segments and two P-loops. 4TM/2P and 8TM/2P channels are discovered more recent and are thought to form dimers[6,9,10] instead of tetramers.

From an evolutionary point of view, the 6TM/P group may have arisen by adding to 2TM/P core a 4TM portion (S1-S4) which included several positively charged residues as primitive voltage sensor[4]. Cloning of potassium channels enabled the findings of many potassium channels and the sequences indicated that potassium channels formed tetramers and the similarities between sodium or calcium ion channels and potassium channels[4]. The sodium and calcium ion channels would have derived by two rounds of tandem gene duplication of 6TM/P channels[4] (see Figure 1.3.A).

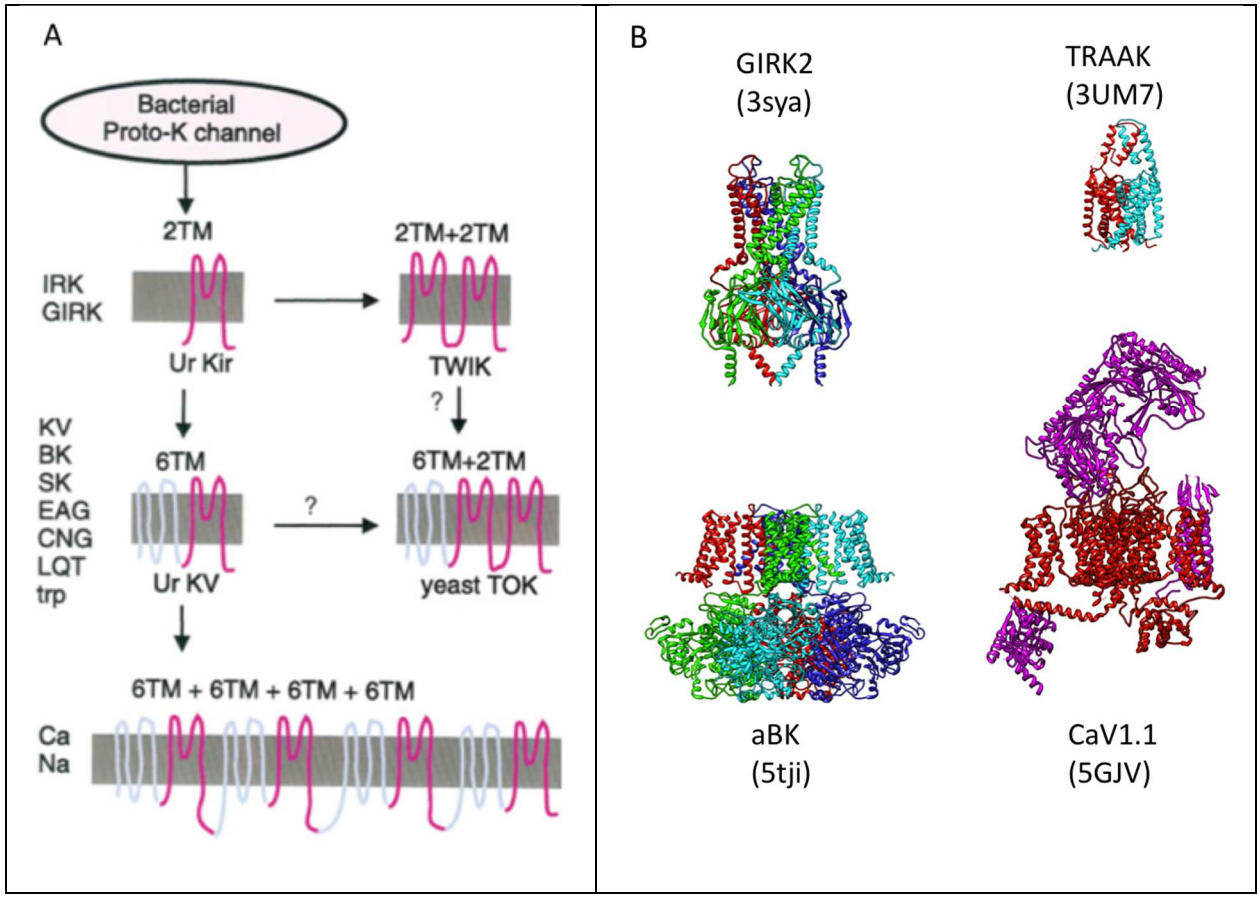

Figure 1.3 Evolution of the superfamily of voltage-gated channels. (A) Topologies of channels[4] (B) Ribbon representations for 2TM/P, 4TM/2P, 6TM/P and CaV channels: GIRK (PDB: 3sya)[11], TRAAK (PDB: 3UM7)[12], aBK (PDB: 5tji)[13], CaV1.1 (PDB: 5GJV)[14].

Regulatory β subunits, also known as auxiliary subunits, may also play an important role in the modulation for many potassium ion channels. They alter the functions of α subunits by interacting with α subunits[6,15,16]. For example, Kv1 family channels interact through their N-terminal tetramerization domain with Kvβ1–3 proteins[16] (see Figure 1.5.C). Some auxiliary subunits are membrane proteins and are intimately associated with the pore domain (see Figure 1.5.D).

Many human diseases have been associated with malfunctions of potassium ion channels, such as cardiac arrhythmias, epilepsy, autoimmune diseases, and misregulation of blood pressure[17]. A number of drugs are used therapeutically on potassium channels[18]. Examples are Class III antiarrhythmic agents such as dofetilide and MK-499 for cardiac-delayed rectifier K+ currents, KCOs such as pinacidil for ATP-sensitive K+ channel, and polyamines for the inward rectifier channels.

1.2 Voltage-gated Potassium Ion channels

Excitable cells give us the ability to catch a basketball or feel pain. Examples of excitable cells

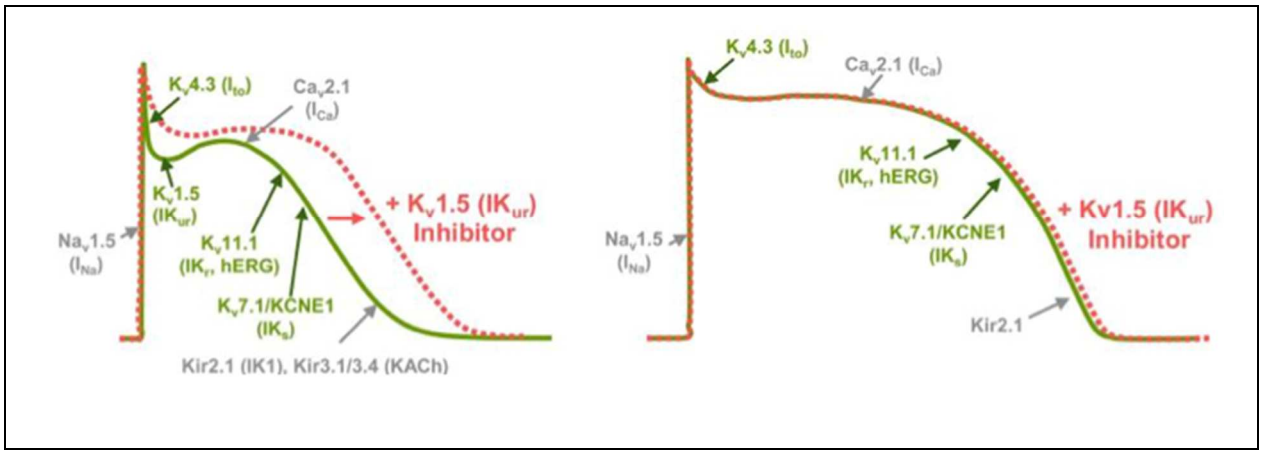

Figure 1.4 Action potential examples: Schematic of a human atrial (left) and ventricular (right) action potential[16]

are neurons, muscle cells, and some endocrine cells. They are cells that can be electrically

excited resulting in the generation of action potentials. An action potential is the transient, rapid rise and fall of the membrane voltage as shown in Figure 1.4. To send a signal, voltage-gated sodium channels open, allowing sodium to enter the cell and thus reducing the voltage across the membrane. Then voltage-gated potassium channels are open as the membrane is depolarized (HCN channels are open when the membrane is hyperpolarized), letting the potassium ions efflux and membrane potential is restored. The action potential can be propagated as Hodgkin and Huxley described in their model in 1952[19]. Their experiments on squid giant axons also observed the negative transmembrane potential which led to the hypothesis that the cell was predominantly selective for potassium at rest[20]. In most neurons, the resting transmembrane potential is around -70 mV. The difference is observed in different species, tissues and conditions.

The Hodgkin-Huxley model provided a mathematical view that how action potentials in neurons worked. Hodgkin and Huxley came up with a model with four currents (capacitance, K^+, Na^+, and leak)[21]. They found that putting n4 in the model, which means four charged particles moved

Hodgkin and Huxley model:

$$I = C_m \frac{dV_m}{dt} + g_K n^4 (V_m - V_K) + g_{Na} m^3 h (V_m - V_{Na}) + g_l (V_m - V_l)$$

where I is the total membrane current per unit area, V_m is membrane potential, C_m is the membrane capacitance per unit area, g_K and g_{Na} are the conductances per unit area for K^+ and Na^+, respectively, V_K and V_{Na} are K^+ and Na^+ reversal potentials, respectively, g_l is the leak conductance per unit area, and V_l is the leak reversal potential, n, m and h are dimensionless quantities between 0 and 1 that are associated with potassium channel activation, sodium channel activation, and sodium channel inactivation.

for activation, introduced the appropriate delay to the onset kinetics to produce a good experimental fit to their voltage-clamp data for K^+ current. Similarly, for the Na^+ current, the activation was fitted well by moving three charged particles (putting m3 in the model) for

activation. Each component of the current obeyed Ohm's law[4], which states that the current is proportional to the voltage.

Given the mathematical model of action potential, it is critical to understand how voltage-gated potassium channels respond to the change of transmembrane potential at a molecular level. Let's first look at the structure of Kv channels. Voltage-gated ion channels belong to 6TM/P family. Each channel is composed of four α subunits, and each subunit has six membrane-spanning α helices (S1–S6). The first four transmembrane helices form the voltage sensor domain (VSD) as

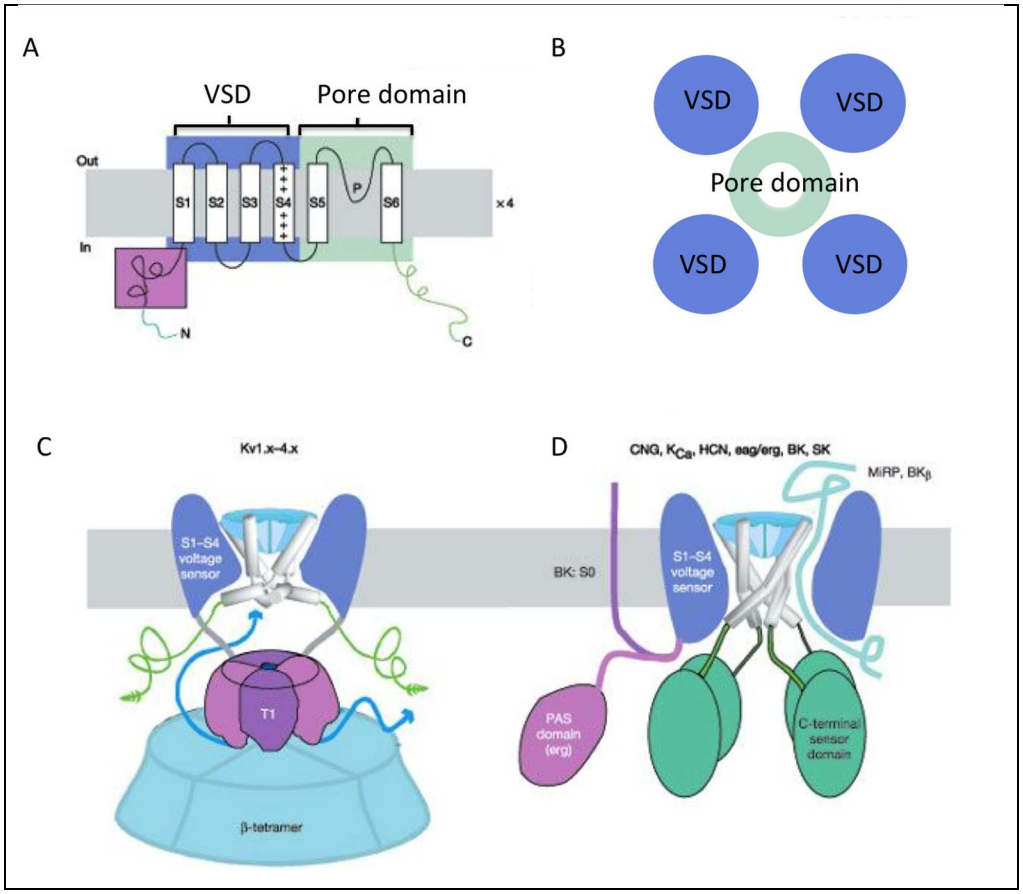

Figure 1.5 The architecture of voltage-gated potassium channels. (A) Topology of a typical Kv channel viewed along the membrane[22]. (B) Membrane topology viewed from extracellular side. (C) Architecture of a typical Kv1-Kv4 channel[22]. (D) Architectures of other Kv channels[22].

shown in Figure 1.5.A. The last two helices S5 and S6 are corresponding the outer and inner helices in KcsA, respectively (see Figure 1.5.B). At the N terminus some family members, such as BK, have an additional transmembrane region (S0) or an additional sensor domain as illustrated in Figure 1.5.D.

How does the VSD translocate the charges across the membrane when the membrane potential changes? Experimental measurements of 'gating currents' shows that the total charge displacement is about 13 elementary charges per channel[23]. The S4 helix is highly positively charged, around four to seven positive charges. Most of the charges are from arginine amino acids, as shown in Figure 1.6. S4 senses the change of membrane potential and moves, thus causing the channel to open and close. The mechanism is still not fully understood.

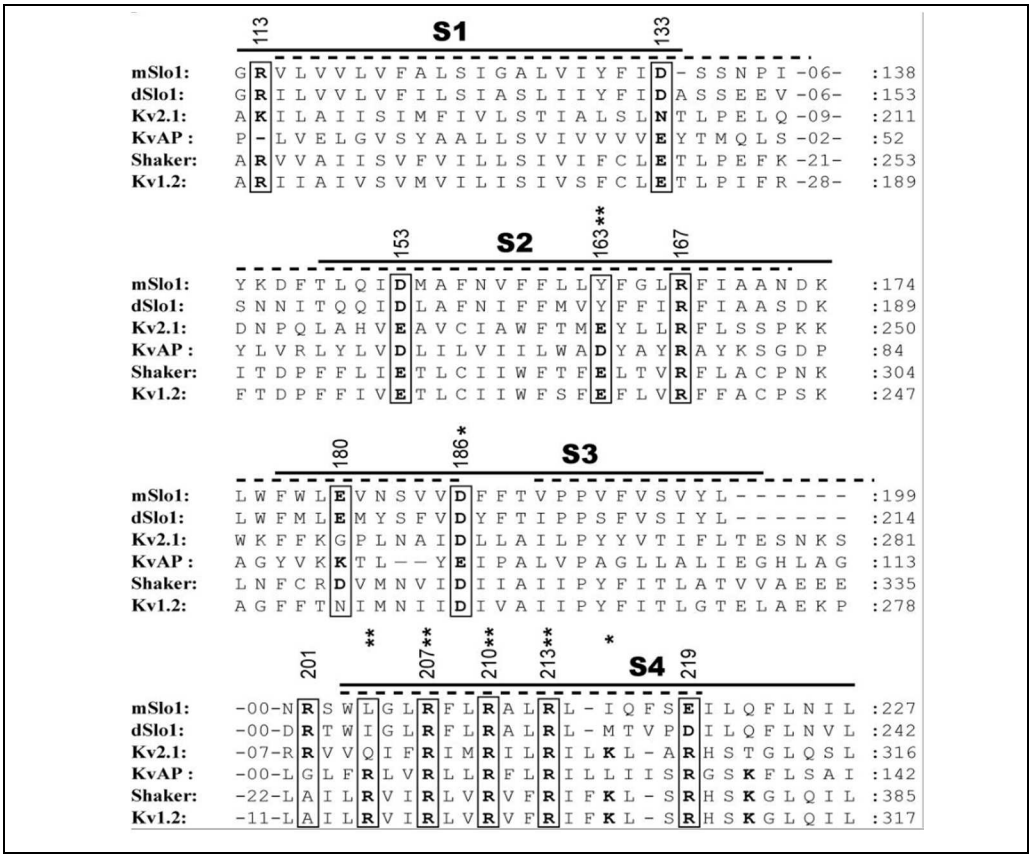

Figure 1.6 Multiple sequence alignment of VSD from mouse and *Drosophila* homologues of Slo1 and Kv2.1, KvAP, shaker and Kv1.2[24]. Charged residues that are highly conserved are bold.

1.3 Calcium-activated Potassium Ion channels

Ca^{2+} is an important intracellular second messenger. Calcium-dependent component potassium currents from single channel recordings[25,26] as well as the *Drosophila* mutant termed slowpoke (slo)[27] led to the identification of the first gene that encodes a calcium-activated potassium channel, which is the large-conductance voltage- and calcium-activated potassium (BK). Genes that encode small-conductance (SK) and intermediate-conductance (IK) calcium-activated potassium channels were discovered later by screening cDNA libraries for sequence resemblance[28]. Slo2.1, Slo2.2 and Slo3 were also assigned to this family as they were predicted to resemble the structure of BK[28]. As a result, eight potassium channels, which are listed in Table 1.1, were designated as calcium-activated potassium channels (K_{Ca}).

Table 1.1. Calcium-activated potassium family channels*

Channel	Alternating names	Gene Symbol (human)	Location
Slo1	BK, K_{Ca}, Maxi-K, Kca1.1	KCNMA1	10q22.3
Slo2.1	Slick, K_{Na}1.2, K_{Ca}4.2	KCNT2	1q31.3
Slo2.2	Slack, K_{Na}1.1, K_{Ca}4.1	KCNT1	9q34.3
Slo3	K_{Ca}5.1, pH-sensitive maxi-K	KCNU1	8p11.2
IK	SK4, Kca3.1	KCNN4	19q13.31
SK1	Kca2.1	KCNN1	19p11.3
SK2	Kca2.2	KCNN2	5q22.3
SK3	Kca2.3	KCNN3	1q21.3

* From HUGO Gene Nomenclature Committee.

More recent studies have documented that not all members are sensitive to calcium. Slo2.1 and Slo2.2 are activated by sodium and chloride. In 2017, International Union of Basic and Clinical Pharmacology proposed a new nomenclature K_{Na} for them[28]. High-resolution cryo-EM structures

of Slo2.2[29,30] confirmed that the structure of slo2.2 indeed looks like that of BK (see Figure 1.7). Slo1, Slo3 and K_{Na} channels all have regulator of conductance for K^+(RCK) domains, whereas SK and IK do not have RCK domains. Instead, they interact with calmodulin (CaM)[31].

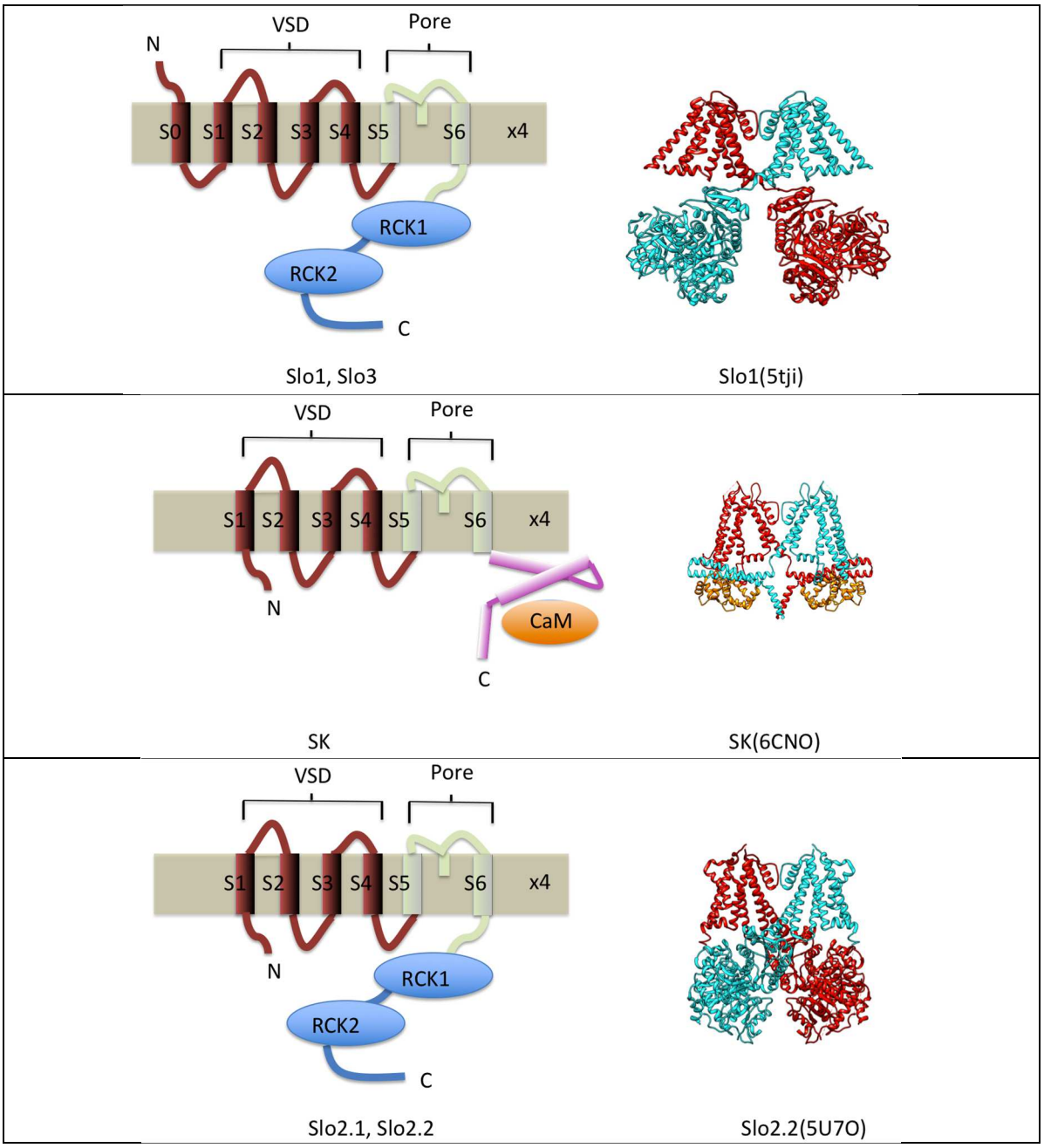

Figure 1.7 Topologies and ribbon representatives of calcium-activated potassium channel family. For ribbon representations (Slo1 PDB: 5tji[13], SK PDB: 6CNO[31], Slo2.2 PDB: 5U7O[28]), only two opposing α subunits colored in red and cyan are shown for clarity. Calmodulins are shown in orange.

The RCK domains, which regulate the conductance of potassium ion, were first solved to high-resolution from prokaryotic calcium-gated potassium channels[32,33] as shown in Figure 1.8.

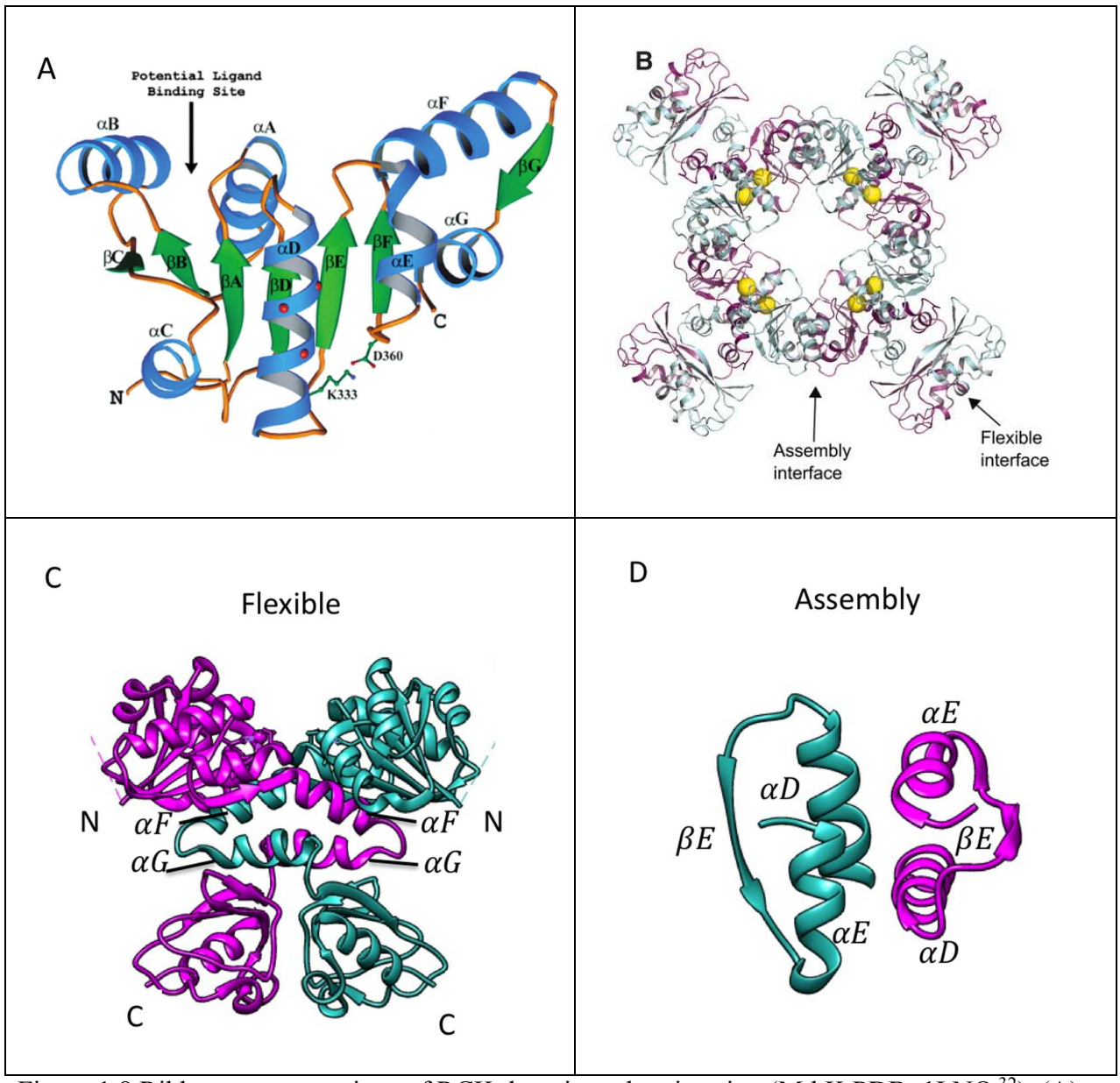

Figure 1.8 Ribbon representations of RCK domain and gating ring (MthK PDB: 1LNQ [32]). (A) Ribbon diagram of the *E.coli* K^+ channel RCK domain[32]. (B) Open gating ring from the MthK[34] with arrows pointed to the interfaces. Calcium ions are shown as yellow spheres. (C) Flexible interface. (D) Assembly interface.

The RCK domain has a Rossmann fold. Five α helices (αA- αE) are on the two sides of a six stranded parallel β sheet (βA- βF) while αF and αG form a helix-strand-helix structure with βG that extends from the six stranded parallel β sheet. Two RCK domains form a homodimer due to

the strong interactions at the dimer interface as shown in Figure 1.8.C. Four such dimers build up the octameric gating ring (see Figure 1.8.B). Two kinds of interfaces exist in the gating ring. The interface formed by αF, αG and C terminal domains within the homodimer is called flexible interface and the interface between αD and αE of two adjacent dimers is called assembly interface (also called fixed interface).

A high-affinity calcium-binding site, called 'calcium bowl', is located in the Rossmann fold of RCK2 near the C terminus. A second high-affinity calcium-binding site is located in RCK1.

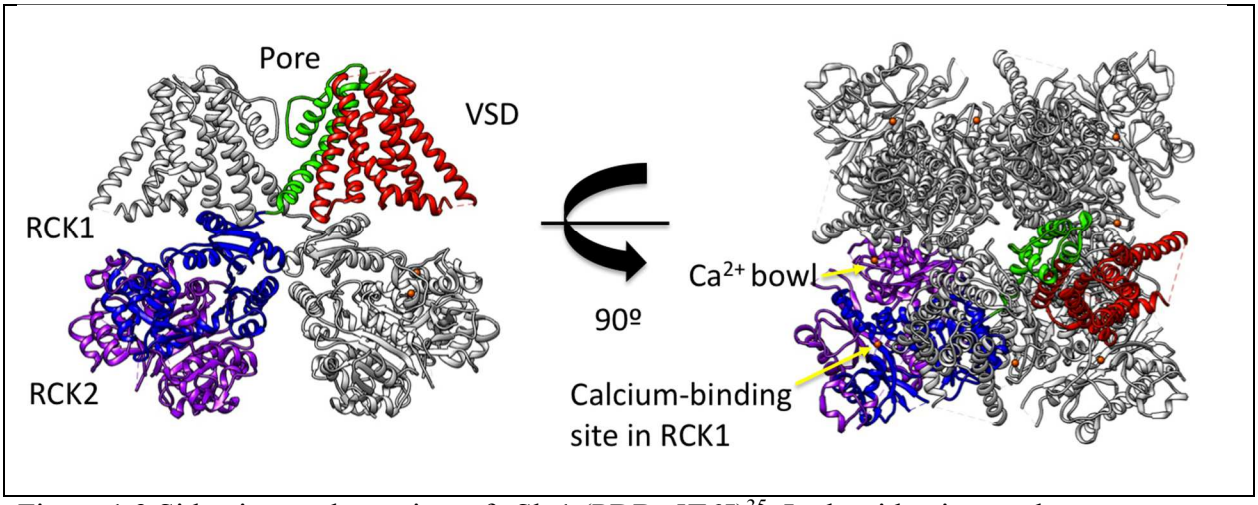

Figure 1.9 Side view and top view of aSlo1 (PDB: 5T6J)[35]. In the side view, only two opposing α subunits are shown for clarity. One α subunit is colored in green, red, dark blue, and purple for pore domain, VSD, RCK1 and RCK2, respectively. Calcium ions are colored in orange.

Although all calcium-activated potassium channels are dependent on calcium for their activation, some of them are synergistically gated by voltage, whereas others are insensitive to voltage. As shown in Figure 1.6, the S4 helixes of BK ion channels are also positively charged and BK channels have voltage dependence.

1.4 My approach to study BK in a lipid environment

The large conductance voltage- and calcium-activated potassium (BK) channel belongs to the voltage-gated potassium channel family as well as calcium-activated potassium channel family.

It can be found in many cells, and functions as a feedback regulator of membrane potential and thereby Ca^{2+} influx [36-38]. Like other members of the voltage-gated potassium channel family, it has VSDs that confer the primary sensitivity to membrane potential. The BK channel also contains RCK domains in the large intracellular C-terminal region like other members of calcium-activated potassium channel family. RCK domains confer [39] the sensitivity to Ca^{2+} and form a "gating ring", which has been determined by X-ray crystallography[40] and Cryo-EM[13,35]. Unlike most 6TM/P α-subunits, α subunit of BK has an additional transmembrane segment S0. Figure 1.7 shows that the N-terminus of BK is extracellular.

In our lab, a method called the random spherically constrained (RSC) cryo-Electron Microscopy method has been used to obtain the structure of BK ion channel to 17 Å resolution[17,41]. This method offers the opportunity to determine the structure of the intact channel in lipid environments. RSC involves reconstituting membrane proteins in artificial liposomes, which are then flash-frozen in liquid ethane. Thousands of cryo-EM micrographs are taken. Then liposome information is computationally subtracted from those micrographs. From liposome-subtracted images, protein particles are manually/semi-automated picked and used to determine membrane protein structures with the use of the geometric constraints of spherical liposomes. With the technological development for both the microscope and the electron detector, I aimed at obtaining a structure of BK ion channel in the range of near-atomic and moderate resolution (3-8 Å).

Although during my study, two cryo-EM structures[13,35] of *aplysia californica* BK channels were determined with and without Ca^{2+} by another lab, my approach was still unique thanks to the lipid environment provided by liposome. To obtain a more refined understanding of the mechanisms of voltage sensing and gating, an actual structure of a voltage-sensing domain in the

resting state is required. Sadly, it was experimentally difficult to obtain the structure of ion channels in the resting state. My study of BK in liposomes provided a way to trap the VSD in desired functional states. I listed my aims below and my timeline is illustrated in Figure 1.10.

Aim1. Established the sample preparation workflow for proteoliposomes vitrification. To achieve high particle density per micrograph for cryo-EM data collection, sample vitrification procedures for liposome system has been optimized.

Aim2. Determined the structure of BK channel at 0 mV transmembrane potential with EDTA. This success of obtaining a high-resolution cryo-EM structure of BK reconstituted in liposomes shed light on structural studies of other membrane proteins and provided a potential cryo-EM lipid system for voltage manipulation.

Aim3. Designed and established a method to manipulate the transmembrane voltage of proteoliposomes. To close the majority of BK channels, a highly negative transmembrane voltage need be applied on the proteoliposomes. To endow the negative potential, a gradient of potassium was induced across the lipid bilayers. The result was validated by fluorescence flux assay.

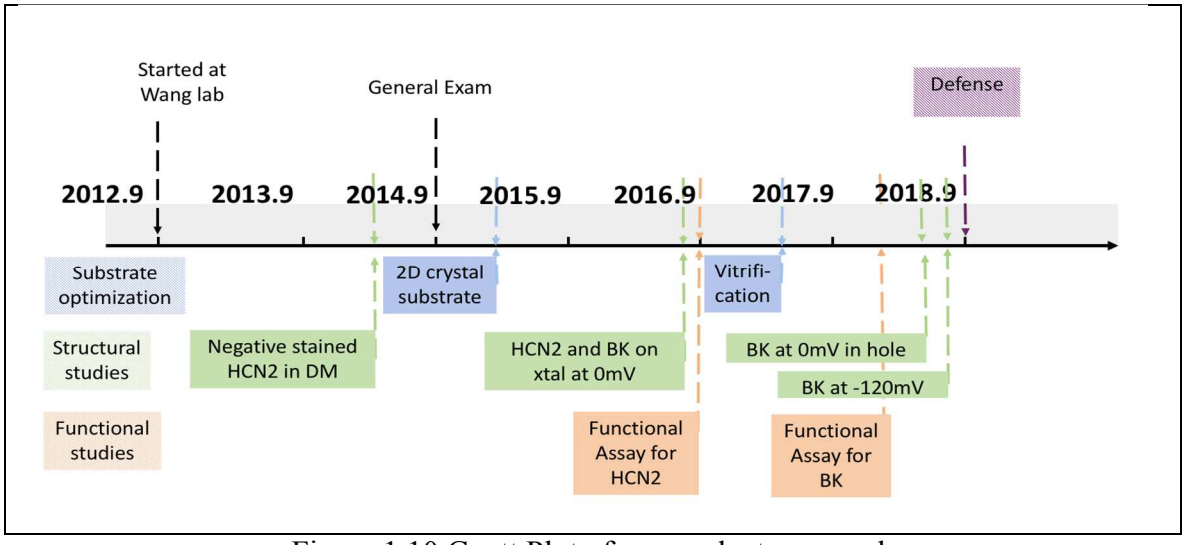

Figure 1.10 Gantt Plot of my graduate research

Chapter 2. Reconstitution of BK channels into liposomes

A review version of this chapter has been previously published as:
Liguo Wang, Lige Tonggu. Membrane protein reconstitution for functional and structural studies. *Sci. China Life Sci.,* (2015) 58:66.

2.1 Introduction

Liposomes are artificial spherical structures enclosed by lipid bilayers, and are used widely as a scaffold for biochemistry researches, as models in theoretical biophysics as well as delivery systems for pharmaceutical uses. Compared to solubilizing membrane proteins in detergent, reconstituting membrane proteins into liposomes has several advantages: First, it provides a lipid environment that mimics the native lipid environment of cells with the flexibility to vary the lipid composition, liposome size and surface charge in preparation. Second, the inside content of liposome can be different from the outside, which makes it perfect to study the function of membrane proteins. Third, they are dynamic thus external stimulus such as pH, heat or ionic strength can be used to trigger changes in liposome structure and changes of membrane proteins. Therefore, reconstitution of purified membrane proteins into liposomes has been developed and served as a powerful tool for elucidating both functional and structural aspects of membrane proteins. This method has been employed successfully to study the function of various ion channels and receptors, such as sodium channels[42], potassium channels[12,41,43] , calcium channels[44], and IP3Rs[45], assessed by measuring the movement of radioactive ions/calcium ions, or protons. In structural studies, this approach has been used to determine the BK structure at 17 Å [41] resolution and Kv1.2 at 12 Å resolution[46]. Prior to my study, there was no structure of membrane protein determined at atomic to high-resolution range (3-6 Å) with this approach though.

Studies of membrane protein functions in reconstituted liposomes started in the 1970s by the pioneering work of Racker and colleagues[42,47]. Reconstitution of membrane proteins into liposomes usually starts with the isolation of cellular membranes. The isolated membranes are dissolved in either organic solvent (organic solvent-mediated reconstitution) or detergents (detergent mediated-reconstitution). Due to the exposure of membrane proteins to organic solvents (e.g., ether and pentane) in the organic solvent-mediated reconstitution process, membrane proteins are usually denatured. This precludes detailed functional studies of the reconstituted proteins. The most successful and widely used strategy for membrane protein reconstitutions is the detergent-mediated reconstruction, which I am applying to BK ion channels reconstitution. In the standard detergent mediated-reconstitution procedure, purified membrane proteins in the presence of detergents are mixed with detergent-solubilized lipids to form an isotropic solution of lipid-detergent-protein and lipid-detergent micelles. The detergent is then removed, resulting in the formation of proteoliposomes.

For the structural study of BK, my goals were: 1) Form liposomes with diameter of 20-40 nm, which are large enough to reconstitute BK channels and small enough to maintain a layer of thin ice for cryo-EM sample; 2) Have lipid recovery yield as high as possible; 3) Have proteoliposomes population dominant in the empty liposome and proteoliposomes mixture.

In this chapter, I will talk about the results for the lipid-detergent system, then the results for the lipid-detergent-BK system in the aspect of liposome size and lipid yield, lipid to protein ratio (LPR) as well as protein orientation.

2.2 Results and Discussion

2.2.1 The properties and choice of detergent for BK purification

It is crucial to understand the properties of detergents for the study of membrane proteins. Based on the type of the head group, detergents can be classified into three groups: ionic (cationic or anionic), nonionic, and zwitterionic. Ionic detergents such as sodium dodecyl sulfate (SDS) interrupt protein-protein interactions thus denature proteins. Nonionic and zwitterionic detergents are considered mild when used to solubilize membrane proteins due to the preservation of the protein-protein interactions.

Detergent molecules start to self-associate and form micelles at a threshold of monomer concentration, which is called the critical micelle concentration (CMC). The CMCs of a few commonly used detergents are listed in Table 2.1. The concentration of detergent monomers stays constant at CMC as more detergent is added to the solution; only the concentration of detergent micelles increases. In order to solubilize hydrophobic or amphipathic molecules, such as proteins and lipids, the detergent concentration must exceed the CMC[48].

Table 2.1. Properties of common detergents*

Detergent	Category	Mw (Da)	CMC (mM)	Micelle Mw (Da)
sodium dodecyl sulfate (SDS)	Ionic	288	6-10	18,000
Sodium Cholate	Ionic	431	9-15	900-1300
Triton X-100	Zwitterionic	615	0.2-0.9	80,000
n-Decyl-β-D-Maltoside (DM)	Nonionic	483	1.8	72,000
n-Dodecyl β-D-maltoside (DDM)	Nonionic	511	0.15	50,000
Digitonin	Nonionic	1229	<0.5	70,000

*Data are from Sigma Aldrich and Anatrace websites.

From Rigaud and colleagues[49], the solubilization of pure phospholipid membranes by detergents involves three stages. In Stage I, detergent monomers partition into lipid membranes (i.e., liposomes), which results in larger liposome size evidenced by the slight increase of the optical density. In Stage II, lipid membranes saturated with incorporated detergents begin to dissolve, which results in the coexistence of detergent-saturated liposomes and lipid-detergent micelles. In Stage III, lipid membranes are fully solubilized into lipid-detergent micelles. There are three schemes as shown in Figure 2.1.A.

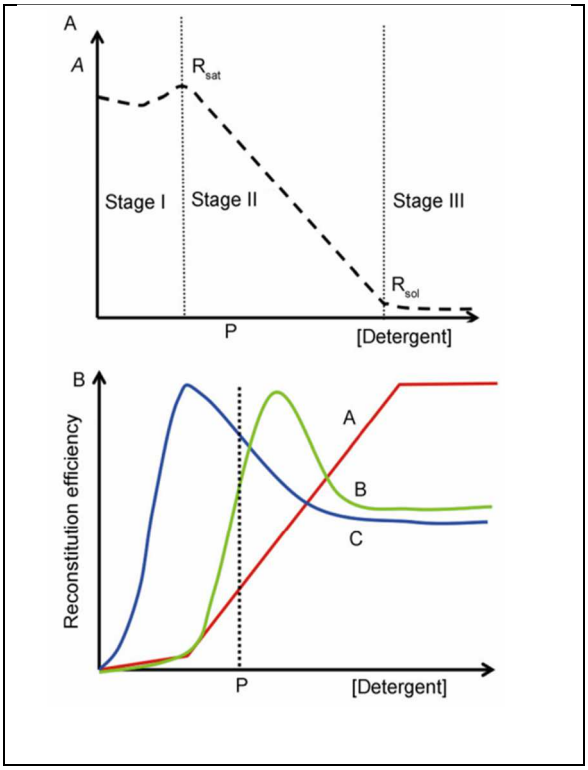

Figure 2.1 Schematic representations of the protein reconstitution mechanisms adapted from Rigaud[49]. (A) Optical density of lipid-detergent suspension. (B) Reconstitution efficiency of membrane proteins using detergent A, B and C. The main lipid phase is the lipid bilayer in stage I. Bilayers and micelles coexist in stage II. Complete solubilized lipid in mixed micelles in stage III.

It is well known that the binary lipid-detergent system behaves differently from those of the pure components. The addition of a membrane protein to the lipid-detergent mixture further complicates the interactions. Thus, detergent behavior, during and after protein extraction from a bilayer, will impact the isolation, characterization, and stability of membrane proteins.

To extract membrane protein from cellular membranes, detergents are added, while to reconstitute membrane proteins into liposomes, detergents are removed.

Figure 2.1.B shows that the reconstitution efficiency (i.e., whether the membrane protein is reconstituted into liposomes) depends strongly on the initial detergent concentration. For example,

the reconstitution efficiency for detergent C (blue curve) is much higher at Rsat than at Rsol. Second, the reconstitution efficiency depends on the nature of the detergent used. At point P, the reconstitution efficiency with detergent C is higher than that with detergent A. Also, the maximum reconstitution efficiency occurs at different detergent concentrations. Lastly, the reconstitution efficiency also depends on the membrane protein of interest, the composition of the lipids, the removal rate of detergent, the ionic conditions and the precise conditions of the initial detergent solubilization.

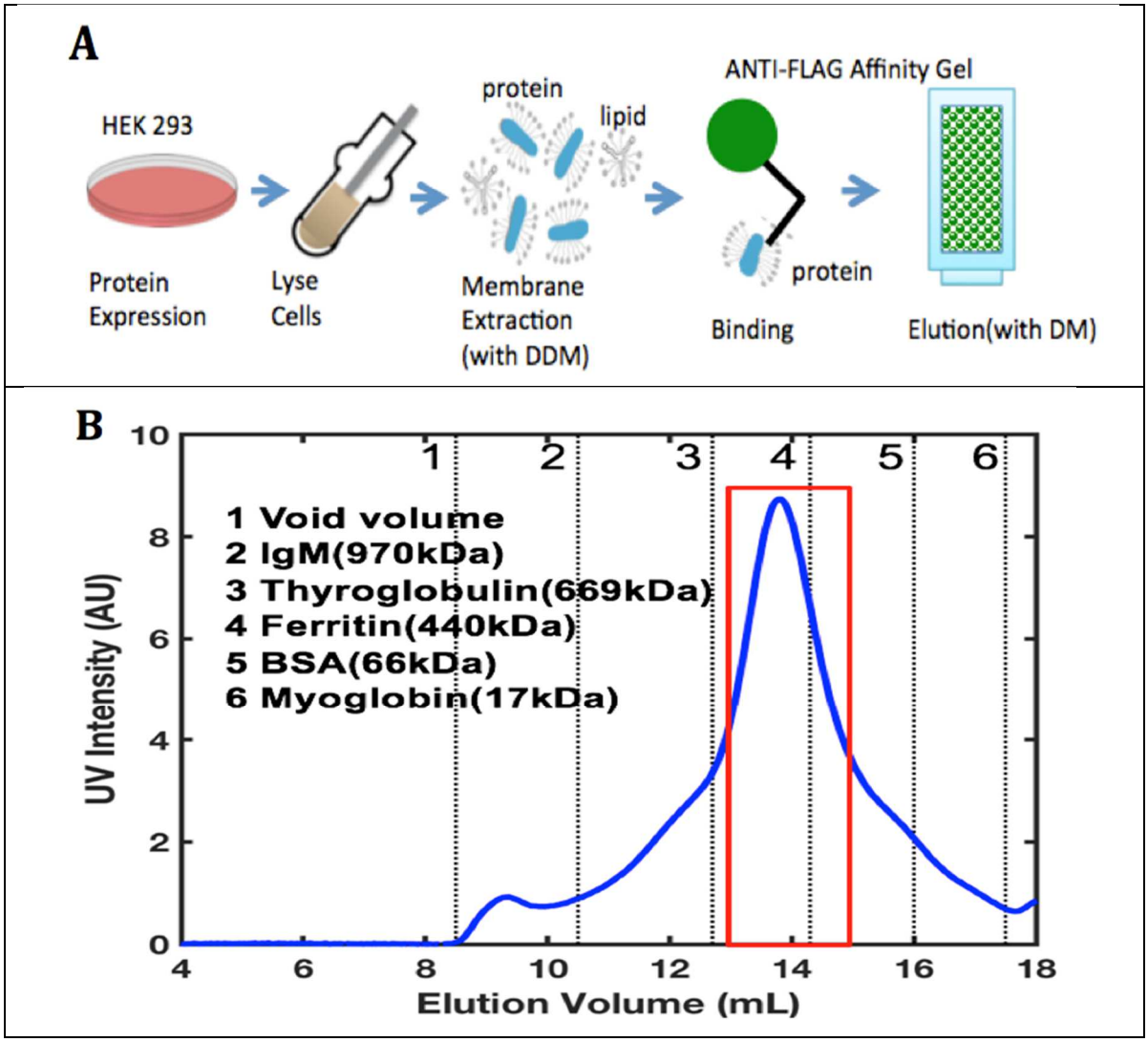

Figure 2.2 BK purification procedure and elution profile (A) flow chart (B) elution profile from Superose 6. BK fractions within red box were collected.

During BK ion channel membrane extraction step, mild nonionic detergent DDM is used. Due to the low CMC of DDM, it is hard to be removed from the lipid-detergent-BK mixture during the reconstitution step. To ensure the complete removal of detergent later in the reconstitution step, I switched the detergent from DDM to DM after the washing step on anti-FLAG affinity column. The elution was then concentrated and further purified by running through Size Exclusion Column Superose6 (GE Healthcare, Chicago, IL) with 4 mM DM in the running buffer to further obtain the peak corresponding to tetrameric BK as shown by Figure 2.2.B.

2.2.2 Detergent-mediated reconstitution for lipid-detergent binary system

Although the lipid-detergent system is very simple compared with the lipid-detergent-protein system, it can serve as a starting point to understand the protein reconstitution process. Dialysis and Gel Filtration are two of the most common techniques to remove detergents.

In a standard dialysis procedure, the lipid/detergent mixture is dialyzing against detergent-free buffer (in ~200-1000 fold excess) in a dialysis bag (high permeability cellulose membrane) under slow stirring. This technique works well for detergents with high CMCs but it's unsuitable for detergents with low CMCs such as DDM or Triton X-100. Dialysis is a very gentle method and is recommended when labile and unstable molecules are incorporated into liposomes. In a standard gel filtration procedure, liposomes can be separated based on the size differences between mixed micelles and liposomes. Gel filtration uses a detergent-free buffer for elution. The molecular diffusion and faster access to the smaller aggregates (monomers, mixed micelles) to the gel pores result in the formation of liposomes.

Both methods have their own advantages and disadvantages. Dialysis is cost efficient and simple to use, but there exist two major drawbacks: (i) uncontrolled detergent removal rate, thus poor

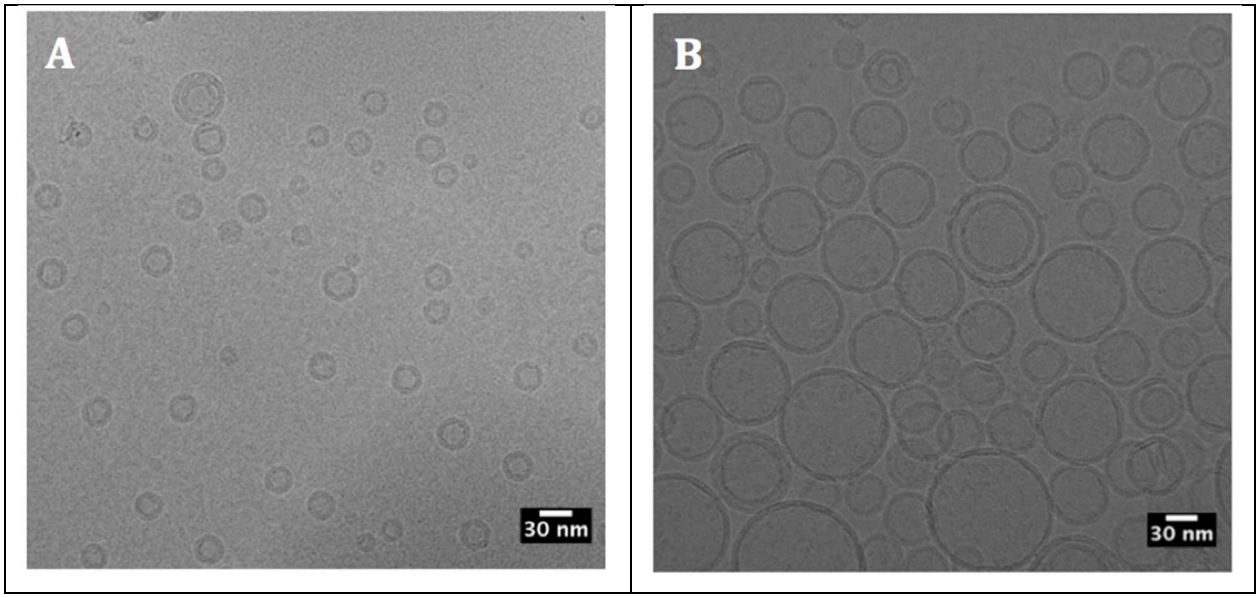

Figure 2.3 Cryo-EM images of dialyzed liposomes: (A) empty liposomes with lipid-DM mixture at the beginning. (B) BK proteoliposomes with lipid-DM-BK at the beginning.

reproducibility, (ii) long duration of dialysis due to the number of changes of buffer (3 days to a week). In comparison, gel filtration is very fast and highly reproducible. It only takes 10-30 min using a 24 ml Sephadex G-50 column. However, based on my experiments, the lipid recovery rate of gel filtration (~50%) is usually lower than that of dialysis (~80%). What's more, the sample is diluted after gel filtration; so, an extra concentration step is needed.

The dialyzed BK proteoliposomes have a mean diameter of 52 nm, with most of the liposomes bigger than 30 nm. Histogram also shows that the size distribution of dialyzed liposomes is quite wide, with a standard deviation at 22 nm for diameter (Figure 2.4). As I mentioned earlier, for cryo-EM structural studies, I want to obtain a layer of vitrified ice film thinner than 40 nm to ensure good particle contrast. The fact that the liposomes are big makes it impossible to embed liposome in ice and prepare a thin layer of ice at the same time. Another important reason I did not choose dialysis is that it took a longer time to prepare. Compared with dialyzed BK proteoliposomes, proteoliposomes generated by gel filtration have a mean diameter of 21 nm

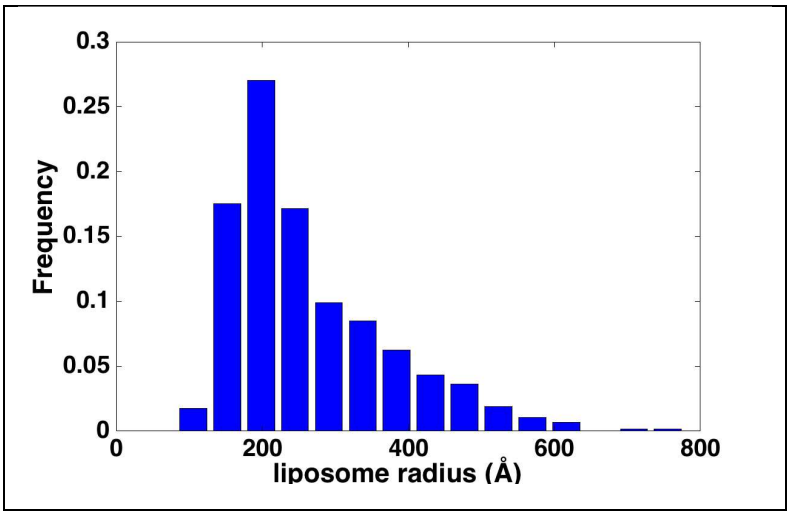

Figure 2.4 Histogram of dialyzed proteoliposomes.

with most of the liposomes smaller than 40 nm (Figure 2.10). With all those in mind, I used gel filtration instead of dialysis for proteoliposomes formation for structural studies. For functional flux assay, as two kinds of phospholipids were used, gel filtration might result in phase separation. Thus, dialysis was used instead. More about flux assay will be found in the next chapter.

In order to investigate the loading volume effect on gel filtration column, I firstly loaded the same amount of lipids (20 µl of 10 mM POPC stock solution containing 30 mM DM stock) but in variable total volume ranging from 250 µl to 2 ml to a 24 ml Sephadex G50 column. As shown in the Figure 2.5.A, smaller total volume gave sharper elution profile which indicated better efficiency; while larger total volume showing a broader profile. This is similar to the behavior of classical protein separation in gel filtration chromatography.

In another experiment, the total loading volume is kept constant at 2 ml, but the lipids amount is varied from adding 20 µl of lipid stock to 80 µl of lipid stock. The result is shown in Figure 2.5.B. The larger amounts of lipids (larger initial volume of lipid stock), the higher lipid concentration was observed at relatively similar elution volume gave a stronger signal, which indicated similar efficiency for all the conditions.

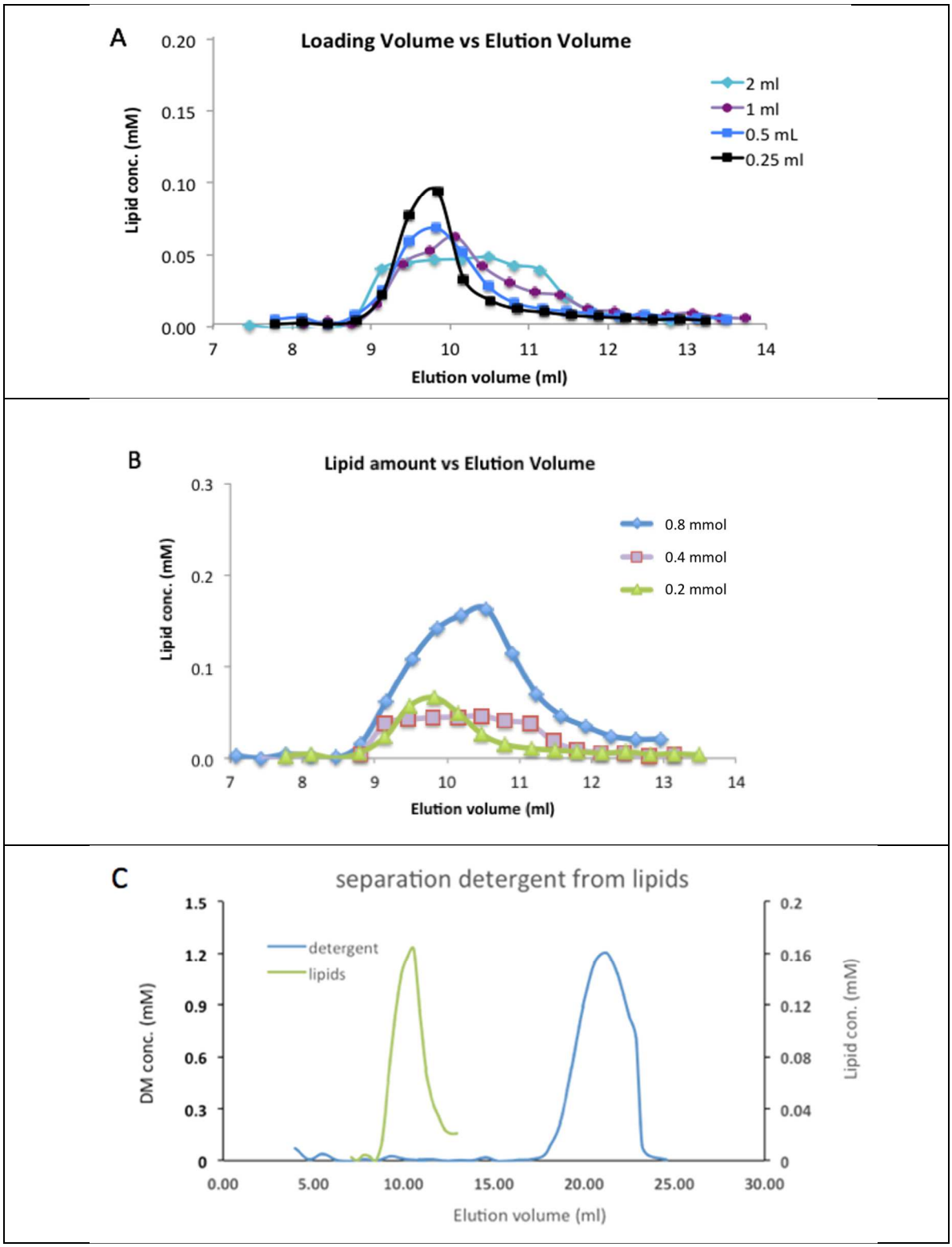

Figure 2.5 Removal of detergent by gel filtration. (A) Lipid elution profiles for different loading volumes (0.25 ml to 2 ml). (B) Lipid elution profiles for different initial lipid stock volume (initial lipid concentration from 0.1 mM to 0.4 mM). (C) Lipid and detergent elution profiles.

As shown in Figure 2.5.C, the peak of detergent DM is at the end of elution while the peak of liposomes is right after the void volume. No detectable overlap of lipid and detergent were observed.

Table 2.2 Summary of gel filtration conditions

Loading volume (ml)	DM conc. (mM)	Lipid conc. (mM)	Flow rate (ml/min)	Lipid yield (%)
0.25	5.3	0.8	0.25	48
0.5	5.3	0.4	0.25	50
1	4.5	0.2	0.24	54
2	4.3	0.1	0.25	57
2	5.1	0.2	0.25	48
2	5.0	0.4	0.25	43

As shown in Table 2.2, the recoveries of lipids from the gel filtration were very close in all cases, either for the 20 µl of lipids sample spiked into varying total volume or different volume of lipids volume diluted into the same 2 ml total volume. However, the recovery rate was as low as 43%, probably due to lipids-resin interaction.

One thing to be noted here is that the detergent concentration in all conditions above was determined by the volume of lipid stock used. When fake elution buffer containing 150 mM KCl, 20 mM HEPES and 4 mM DM was mixed with a different initial volume of 10 mM lipid stock solubilized by 30 mM DM, initial detergent concentration ranged from 4.3 mM to 5.4 mM. However, I tested the effect of the small range of detergent concentration difference by adding more detergent to the 2 ml total volume and 0.1 mM initial lipid concentration group to make it 5.3 mM and the lipid profile is similar to the profile when initial DM concentration was 4.3 mM. Figure 2.1 shows both 4.3 mM and 5.3 mM initial DM concentration is well above CMC of DM

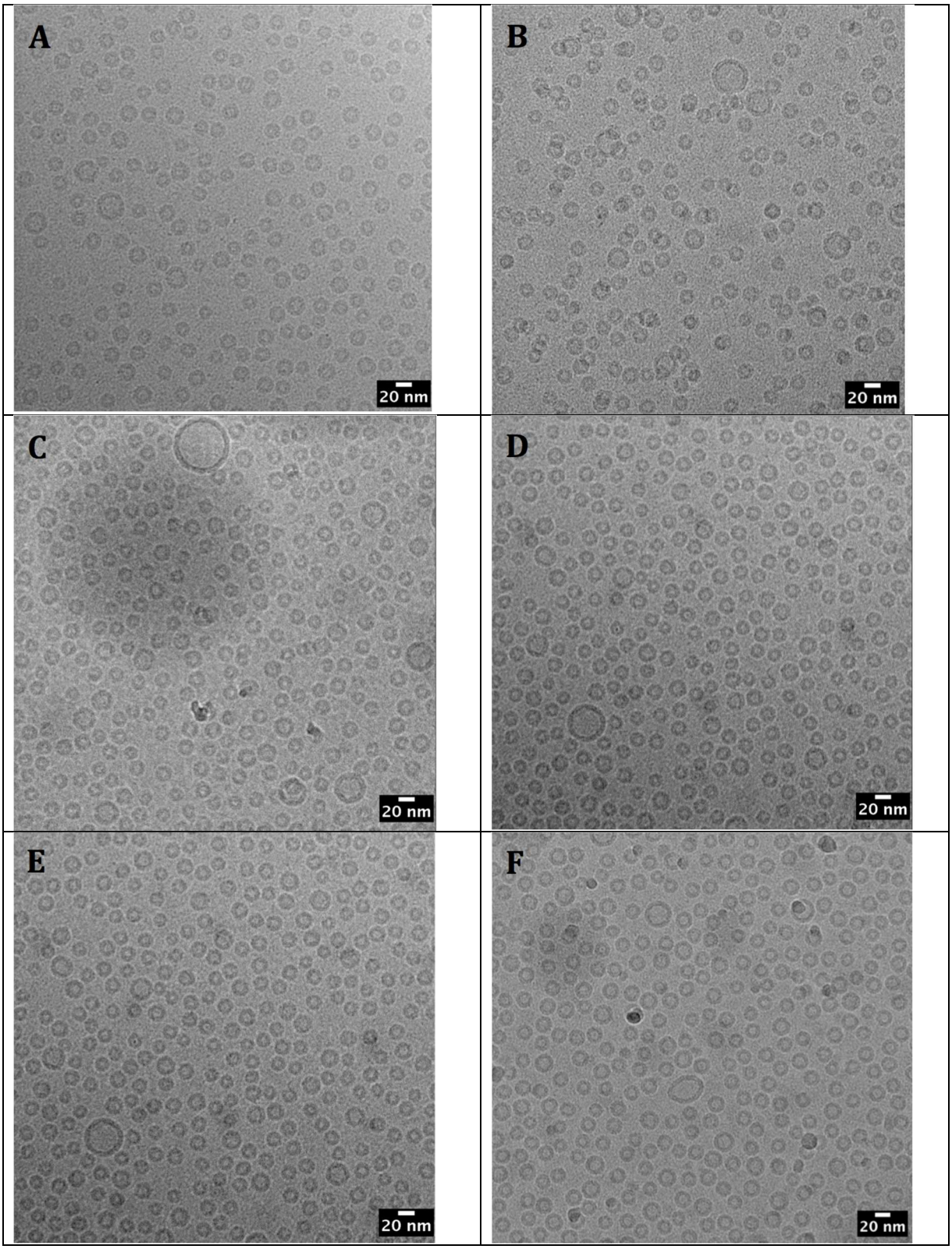

Figure 2.6 Cryo-EM images of liposomes formed with various loading volume and lipid amounts: (A) 0.25 ml and 0.8 mM lipid (B) 0.5 ml and 0.4 mM lipid (C) 1 ml and 0.2 mM lipid (D) 2 ml and 0.1 mM lipid (E) 2 ml and 0.2 mM lipid (F) 2 ml and 0.4 mM lipid.

so the reconstitution efficacy was in the plateau region with no big difference.

For all the conditions listed in table 2.2, the formed liposomes are all around 20 nm in diameter, which can be used for cryo-EM structural studies. When comparing the size distributions for each condition, no significant difference is observed.

I compared Sephadex G-25 and Sephadex G-50 as gel filtration medium to separate lipids solution. As Figure 2.7.A shown, Sephadex G-25 resin has a separation range of 1,000-5,000 Da for proteins while the G-50 has a separation range of 1,500-30, 000 Da. Both of them are generically ideal to exclude the liposome into matrix holes since the liposome is typically larger than 50 kDa.

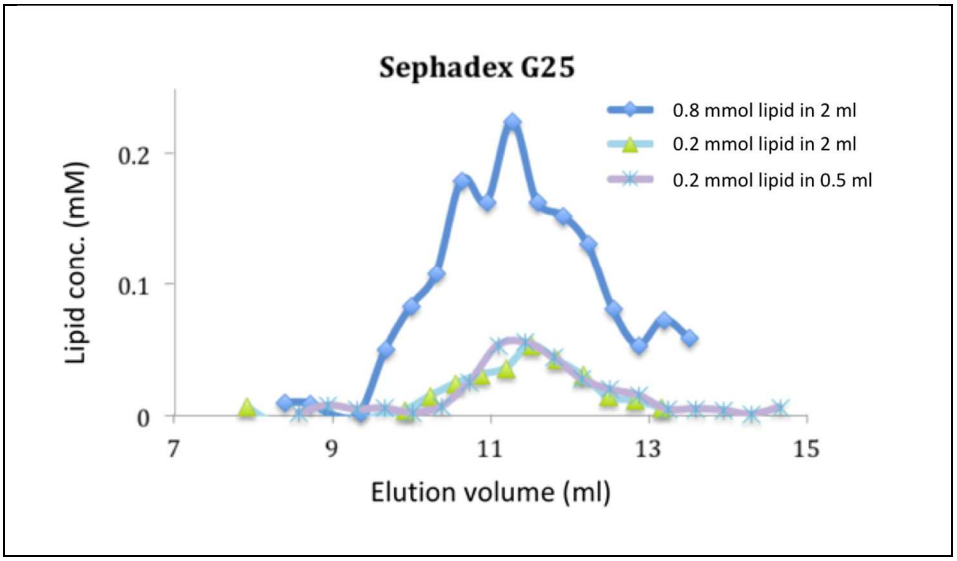

Figure 2.7 Lipid elution profiles for Sephadex G-25.

As shown in Figure 2.7, similar to Sephadex G-50 resin, the lipids elution profile on a 24 ml Sephadex G-25 resin gave elution peaks around 11 ml in all three conditions tested, and the recovery of lipids was also close to 50%. As for the liposome size distribution, Sephadex G-25 column gave a similar result as Sephadex G-50 column as shown in Figure 2.8.

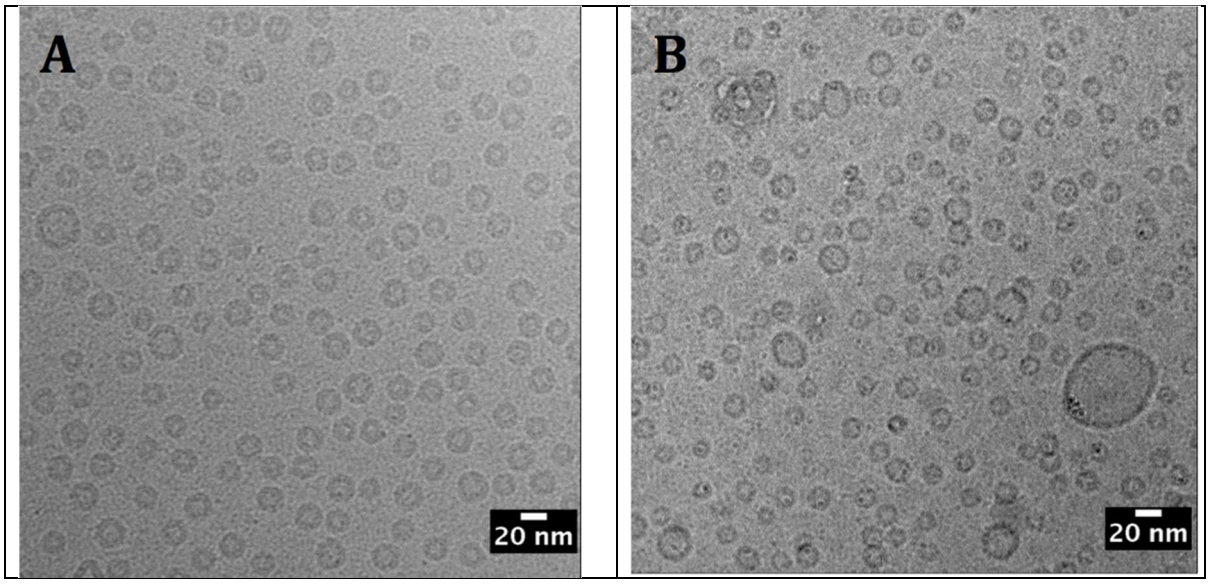

Figure 2.8 Cryo-EM images of (A) liposomes from Sephadex G-50 (B) liposomes from Sephadex G-25.

2.2.3 Reconstitution of BK protein

As the goal of my testing is to find the best gel filtration operating condition in the aspects of lipid recovery rate, liposome size and detergent separation competence, I found for a wide range of the parameters (total loading volume, initial lipid concentration) were all acceptable. Thus, I adjusted the parameters based on the BK protein purification condition. I chose to use Sephadex G-50 column with 0.25 ml/min flow rate and 2 ml total loading volume considering the collected tetrameric BK peak from Superose6 was 2 ml. As I expect to have 1-3 BK tetramers per liposomes, a lipid to protein ratio 1000:1 (5-6 BK tetramers on an average-sized liposomes based on calculation) was used.

Briefly, 2 ml of 0.1 mg/ml BK solubilized with 4 mM DM was mixed with lipids resulting in 0.2 mM final lipid concentration. After mixing at least 2 hr at 4°C, the mixture was then eluted at room temperature. The BK proteoliposomes were eluted right after void volume while FLAG peptides residuals were eluted around 20 ml of the 24 ml Sephadex G-50 as Figure 2.9.A shown.

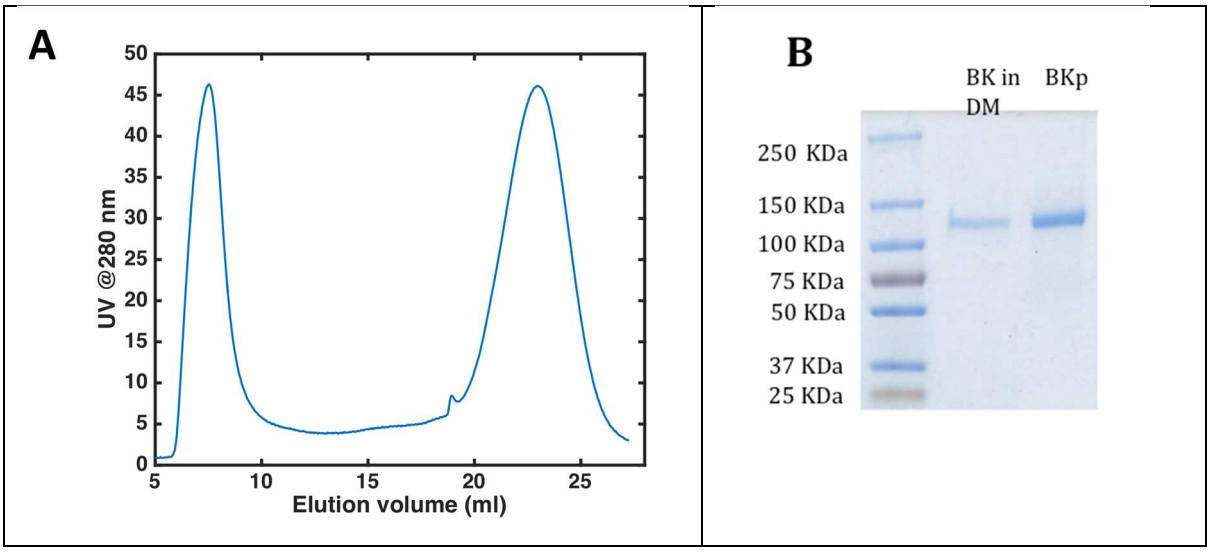

Figure 2.9 Characterization of BK reconstitution. (A) Elution profile for BK proteoliposomes reconstitution. The first peak right after void volume is BK proteoliposomes (BKp) and the second peak near the end of the column volume is FLAG peptides. (B) SDS Page of BK before reconstitution and after reconstitution.

Liposome size distribution

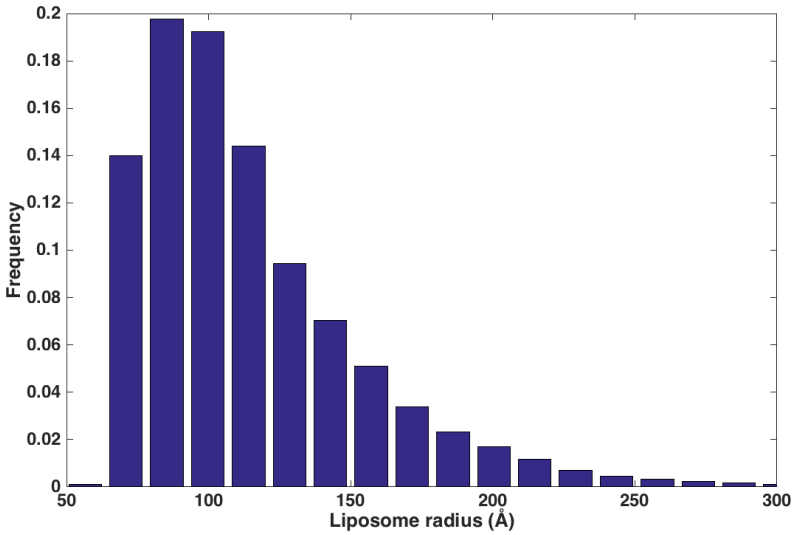

Figure 2.10 Histogram of BK proteoliposomes radius.

The average radius of BK proteoliposomes is 10.5 nm, with standard deviation at 4.2 nm. This distribution is similar to the size distribution of empty liposomes (see Figure 4.4.D). Recalled that for dialyzed liposomes, empty liposomes were much smaller than dialyzed BK proteoliposomes, gel filtration showed good reproducibility.

Lipid yield and protein yield

From lipid assay and SDS Page (see Figure 2.9.B), I calculated the recovery rate for lipid and protein and both were around 50%. This also means that the lipid to protein ratio did not change

during the reconstitution step. Given the average radius of BK proteoliposomes and lipid monomer area (60 $Å^2$), there were about 4 BK tetramers one liposome based on calculation for the final LPR at 1.3k: 1. After data collection and image processing, from 2786 images, there were 122,456 particles used for 3D Classification from 86,931 vesicles with 1.4 BK tetramers per liposome on average, which is 1/3 to the calculated value. One possible reason is that some BK got aggregated and did not go into the liposomes. Another possible reason is that BK proteoliposomes with higher copies of BK did not go into the holes of holey grid but stayed on the carbon region.

Protein orientation

In detergent-mediated reconstitution process, membrane proteins can be inserted in two orientations: inside-out and outside-out. Inside-out orientation means the intracellular region of the membrane protein, in our case, the gating ring of BK, is facing the external solution. Since I had no control of the orientation during the reconstitution, the percentage of each was determined computationally after image processing. With the lipids around the BK channels, the curvature of proteoliposomes could be used to tell the orientation visually. Computationally, a program in our lab MATLAB repertoire used the particle Euler angle and vesicle location to tell inside-out from outside-out. Roughly 85% of the BK channels were inserted inside-out, that is, the majority of

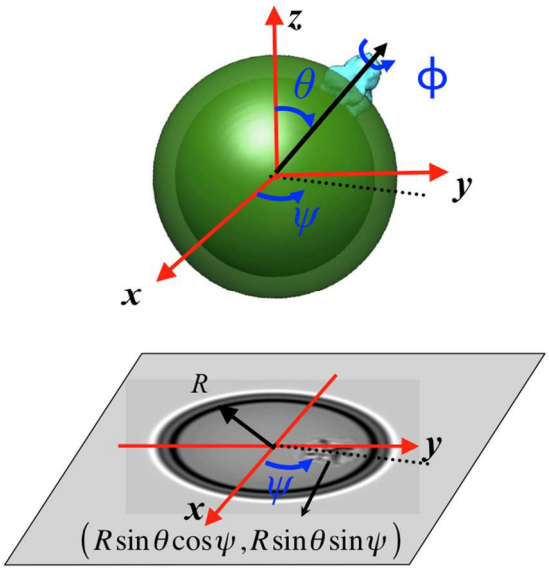

Figure 2.11 Cartoon showing particle orientation determination using liposome constraint.

BK had the large intracellular domain outside of the liposome. More of the visual presentations will be shown in chapter 5.

One possible reason for more BK channels to be inserted inside-out might lie in the fact that about 4/5 of the BK protein mass is in the large cytoplasmic domain. As the average size of proteoliposomes formed by gel filtration is small, the internal compartment of the liposome was less likely to hold the volume of the large gating ring.

This information about orientation population is very helpful when I designed experiments to trap BK in negative potential. Instead of making the inner leaflet of liposome negative charged, I made the inner leaflet positive charged so the majority of BK on the proteoliposomes would have a negative transmembrane potential while 15% of them would have a positive transmembrane potential. More of the sample preparation for a negative potential structural study will be discussed in chapter 3.

2.3 Materials and Methods

Materials

1-palmltoyl-2-oleoyl-sn-glycero-3-phophocoline (POPC) was from Avanti (Alabaster, Alabama). Detergent n-Decyl-β-D-maltopyranoside (DM) and n-Dodecyl-β-D-maltopyranoside (DDM) were obtained from Anatrace (Maumee, Ohio). Sephadex G-50 (DNA grade, fine), Sephadex G-25 (fine), Protease Inhibitor Cocktail (P8340), FLAG peptide (F3290), Anti-FLAG M2 Affinity Gel buffered aqueous glycerol (A2220), Perchloric Acid, HEPES, EDTA, Ammonium molybdate, L-Ascorbic acid and N-Methyl-D-glucamine (NMDG) were from Sigma Aldrich (St. Louis, MO). Econo-Column Chromatography Column (1.0*30 cm) was purchased from BioRad (Hercules, CA). Fetal Bovine Serum was from MilliporeSigma (Burlington, MA). UltraPure buffer-saturated Phenol was from Invitrogen (Calrsbad, CA). Penicillin Streptomycin and

Trpsin-EDTA (0.05%) were from Gibco (Grand Island, NY). Petri dish 150mm was from Corning (Corning, NY). Dialysis Membrane (12,000-14,000) was from Spectrumlab (Irving, TX). Disposable culture glass tubes, Sulfuric acid, Potassium Chloride, Monopotassium phosphate, Sodium Chloride, G418 Sulfate, Dulbecco's Modified Eagle's Medium (DMEM) were from Fisher Scientific (Hampton, NH).

2.3.1 Gel Filtration by gravity

A lipid-detergent mixture contains 0.2 mM lipid and 4 mM DM with or without 0.1 mg/ml BK is rotated at 4°C for 2 hour. Appropriate 0.25-2.0 ml of the lipid-detergent mixture is slowly loaded upon the top of Sephadex G-50 or G-25 column (hand packed in a 10 mm I.D x 300 mm height Econo column, 24 ml volume), which has been pre-equilibrated with running buffer A (150 mM KCl, 20 mM HEPES, pH 7.3). A valve blocks the column bottom until the sample loading is finished, and then the valve is open to drain off all top solution. This process is repeated twice with 1 ml running buffer loading prior to reconnecting the column back to a bottle filled with running buffer. Then the flow is driven by gravity and elution fractions are monitored by ÄKTA purifier system (GE Healthcare, Chicago, IL) and collected by Frac 920 (GE Healthcare, Chicago, IL) at 2 min per tube rate. The liposome is eluted out at an appropriate flow rate between 0.2-0.3 ml/min, which can be adjusted by changing the running buffer bottle relative height to the column and fraction collector. All the operation is done at Room Temperature.

2.3.2 Dialysis

A mixture contains 0.2 mM lipid and 4 mM DM with or without 0.1 mg/ml BK is rotated at 4°C for 2 hour. Then detergent is removed by dialysis against the buffer A containing 20 mM HEPES, pH 7.3, 150 mM KCl at 4 °C for 3-7 days (one day for each buffer change) in a 12-14 kD cut-off dialysis membrane bag.

2.3.3 Detergent Assay

Serial dilute 0.4 mM DM or DDM into 1.5 ml Eppendorf tubes to prepare detergent standard solutions from 0.006 mM to 0.2 mM. Transfer 1 ml of those detergent standard solutions to glass tubes for the following assay as standard curve. Dilute an aliquot of the detergent sample to 1 ml final volume with water. Add 100 µl of 50% Tris buffer-saturated phenol to the solution to make the final phenol concentration 2% (v/v). Add 2.5 ml of 98% sulfuric acid to the tubes and mix properly by vortex the tubes immediately after sulfuric acid addition.

Allow the samples in the test tubes to cool down to room temperature. Measure OD using UV-Vis spectrometer (Hitachi, Japan) at 490 nm for 3 times and use the average to calculate the concentration of detergent in the sample with the linear standard curve.

2.3.4 Lipid Assay

A series of Monopotassium phosphate KH_2PO_4 standards solution from 0.0625 mM up to 1.0 mM is made firstly, then 40 µl of those standards or sample aliquots pooled above were added into glass tubes. After adding 50 µl of perchloric acid to each tube, the solutions were vortexed fiercely and then refluxed at 180 °C in the hood for 60 min or until dry. After cooling down to room temperature, 0.9 ml of analytical solution (0.33 g L-ascorbic acid, 21 ml of Milli-Q water, 2.0 ml of phosphate reagent which was mixture of 5.04 g ammonium molybdate, 84 ml of Milli-Q water and 33 ml of 98% sulfuric acid) was added to these tubes and incubated at 80 °C for another 15 min prior to cooling down the tubes for optical density reading using UV-Vis spectrometer (Hitachi, Japan) at 820 nm for 3 times. The readout is analyzed corresponding to the standard curve produced with the standard solutions.

2.3.5 Cell culture and Protein purification

Full-length human *Slo* protein (GI: 507922) carrying an N-terminal FLAG tag was transfected into HEK-293 cells, and the stable cell lines expressing BK were established. BK protein was purified as previously described[41] with minor modifications. Briefly, cells were broken with Dounce tissue grinder. Cell debris and nuclei were removed by spinning down at 1,000 g for 15 min at 4°C. Supernatants were spun down at 38,400 g for 1 h at 4°C. Subsequently, pellets were mixed with the extraction buffer containing 16 mM DDM, 200 mM KCl, 50 mM Tris, 5 mM EDTA, 1% P8340 at pH7.4. The mixture was rotated at 4°C for 2 h. Detergent-resistant membranes were spun down at 38,400g for 30 min at 4°C. Supernatant was collected and diluted with the same volume of resuspension buffer without DDM. Then it was mixed with pre-washed anti-FLAG M2 affinity gel rotated at 4°C for 1 h for binding. After washing the gel three times with 10 bead volumes of washing buffer 1(200 mM KCl, 50 mM Tris, pH 7.4, 5 mM EDTA, 8 mM DDM, 1% P8340 at pH 7.4) and 5 bead volumes of washing buffer (200 mM KCl, 50 mM Tris, 5 mM EDTA, 4 mM DDM, 1% P8340 at pH 7.4), the beads were exchanged to washing buffer 3 without DDM (200 mM KCl, 50 mM Tris, 5 mM EDTA, 4 mM DM, 1% P8340 at pH 7.4). BK proteins were eluted with elution buffer (0.5 mg/ml FLAG peptide, 150mM KCl, 20 mM HEPES, 2mM EDTA, 4 mM DM, 1% P8340 at pH7.3) and concentrated. Superose6 (GE Healthcare, Chicago, IL) was used to further purify the proteins with150 mM KCl, 20 mM HEPES, 2 mM EDTA, 4 mM DM at pH7.3 as running buffer. The purified channels were then reconstituted into liposomes. For BK reconstitution for negative potential experiment, elution buffer and running buffer containing 150 mM N-Methyl-D-glucamine (NMDG) instead of 150 mM KCl.

Chapter 3. Proteoliposomes provided lipid environment for functional studies

3.1 Introduction

To study membrane protein structures using cryo-Electron Microscopy (cryo-EM), membrane proteins are usually extracted from cell membranes and dissolved in detergents. However, the use of detergent to solubilize membrane proteins always raises a concern whether the protein structure represents a biologically relevant state. As shown by both structural and functional studies, the lipid membrane environment plays an essential role in the structural integrity and activity of membrane proteins [50-55]. Therefore, it is critical to restore the lipid membrane environment of membrane proteins.

To restore the lipid membrane environment of BK, I reconstituted the BK channels into liposomes. There were several concerns about using this method: (1) Are the liposomes intact? (2) Are the BK channels functional in the form of proteoliposomes? (3) Can transmembrane voltage be applied to the bilayer?As Nernst equation puts it, the ions diffuse down an electrochemical gradient. Goldman-Hodgkin-Katz voltage equation is a more generalized form for different ions that is also applicable even when a membrane is not in equilibrium. Those equations provided a way for me to manipulate the transmembrane potential.

Nernst equation:

$$E = \frac{RT}{F} ln \frac{[ion]_{outside}}{[ion]_{inside}}$$

where R is the ideal gas constant, T is the temperature in Kelvin, F is Farady's constant

Goldmann equation:

$$E = \frac{RT}{F} \ln \left(\frac{\sum(P_1[ion1]_{outside} + P_2[ion2]_{outside})}{\sum(P_1[ion1]_{inside} + P_2[ion2]_{inside})} \right)$$

where P is the permeability for ion

Nernst equation and Goldman equation for monovalent ions.

3.2 Results and discussion

3.2.1 Liposomes are intact

To assess whether the liposomes are intact, a leakage assay was used. This assay reports the leakage of vesicles fluorometrically. As shown in Figure 3.1, a fluorophore called HPTX and a quencher called DPX are loaded together inside the liposome at the beginning and no fluorescence signal is detected. When the liposome bilayers get ruptured, some HPTS and DPX are leased to the external solution and are dissociated from each other. As HPTS is no longer quenched by DPX in the external solution, the fluorescence signal is then detected.

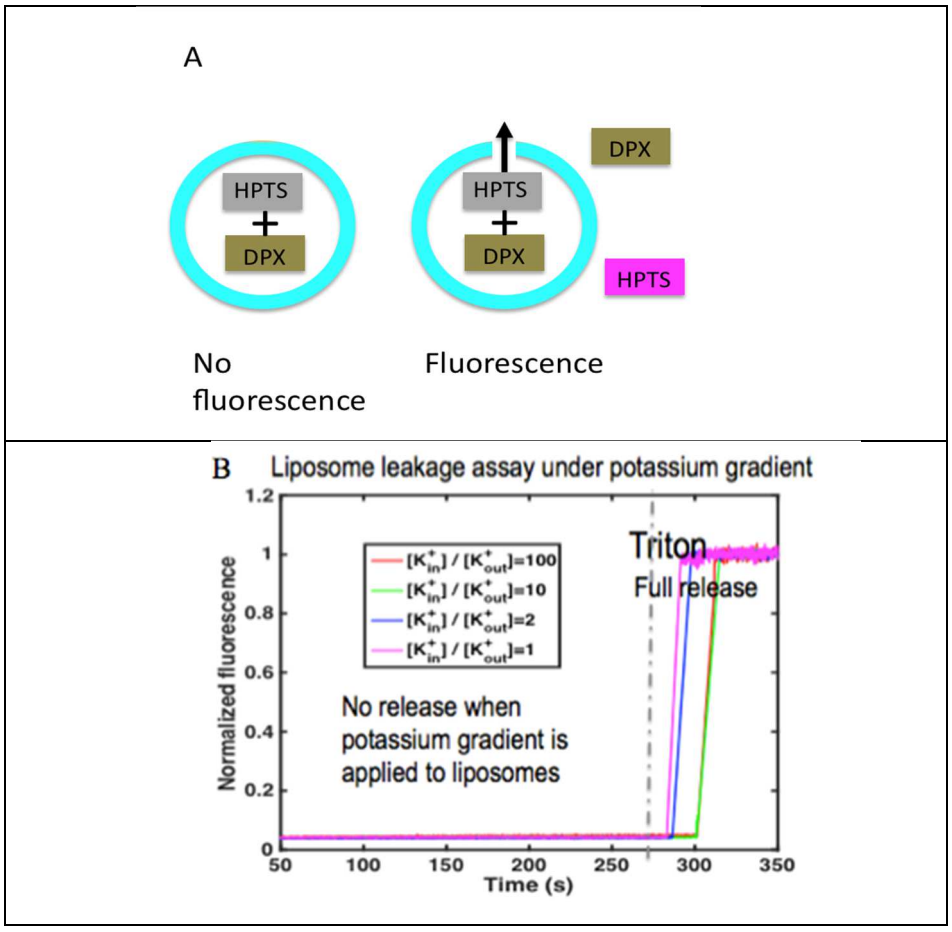

Figure 3.1 Liposome leakage assay. (A) Cartoon showing the dissociation of HPTS-DPX. (B) Traces for leakage assay under different potassium gradients with complete release by triton at the end.

Asymmetric buffer conditions were set up to test the integrity of liposome. Liposome solution preloaded with HPTS and DPX was 100 times diluted into buffers with different potassium concentrations. The internal solution contained 150 mM KCl while the external solution contained 1.5 mM -150 mM KCl and 148.5 mM – 0 mM NaCl with the same osmolality as the internal solution. No fluorescence signal was detected until 1% Triton was added to disrupt the liposome structure. The results showed that dilution of liposome solution to buffers with the same osmolality wouldn't disrupt the liposome integrity.

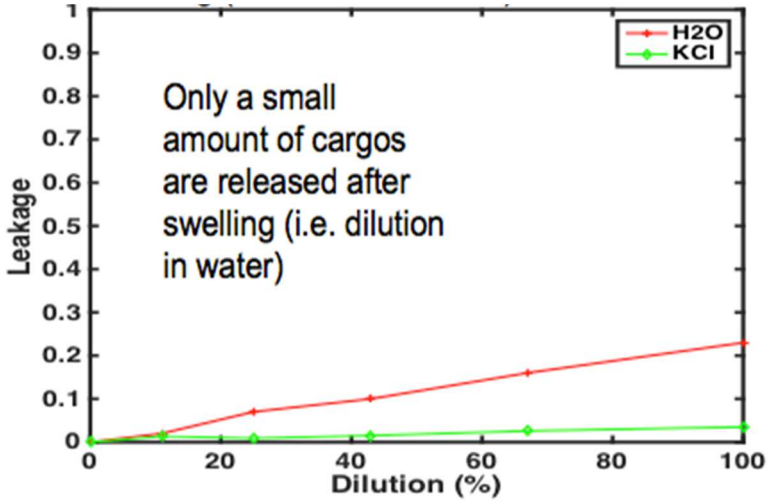

Figure 3.2 Normalized fluorescence when liposomes were sequential swelled in water.

To make liposome as round as possible for structural studies, sequential swelling was used. Repeated osmotic shocks were introduced by adding Milli-Q water step by step. A series of 11%, 14%, 18%, 24% and 33% (v/v) water, that is, 11%, 25%, 43%, 67% and 100% dilution, was added during the leakage assay measurements. As a comparison, the same amount of 150 mM KCl buffer was added as a control. The pH of all diluted buffer remained the same thanks to the HEPES in the initial buffer. After the 5-step swelling procedure, around 20% of liposome internal content was released after the addition of water while less than 5% content was released after the addition of KCl buffer. This result showed that liposomes integrity can be restored after small osmotic shock. It also indicated the internal solution contained around 120 mM KCl after 5-step swelling, while the KCl concentration in the external solution was decreased to 75 mM.

3.2.2 BK channels are functional in BK proteoliposomes

In the presence of a potassium gradient across the lipid membrane, functional BK channels allow the K^+ ions to cross the lipid membrane, thus resulting in a negative potential inside liposomes (Figure 3.3). The flux of the potassium ions can be monitored indirectly by the change of pH using a proton-sensitive dye ACMA[12,43,56,57].

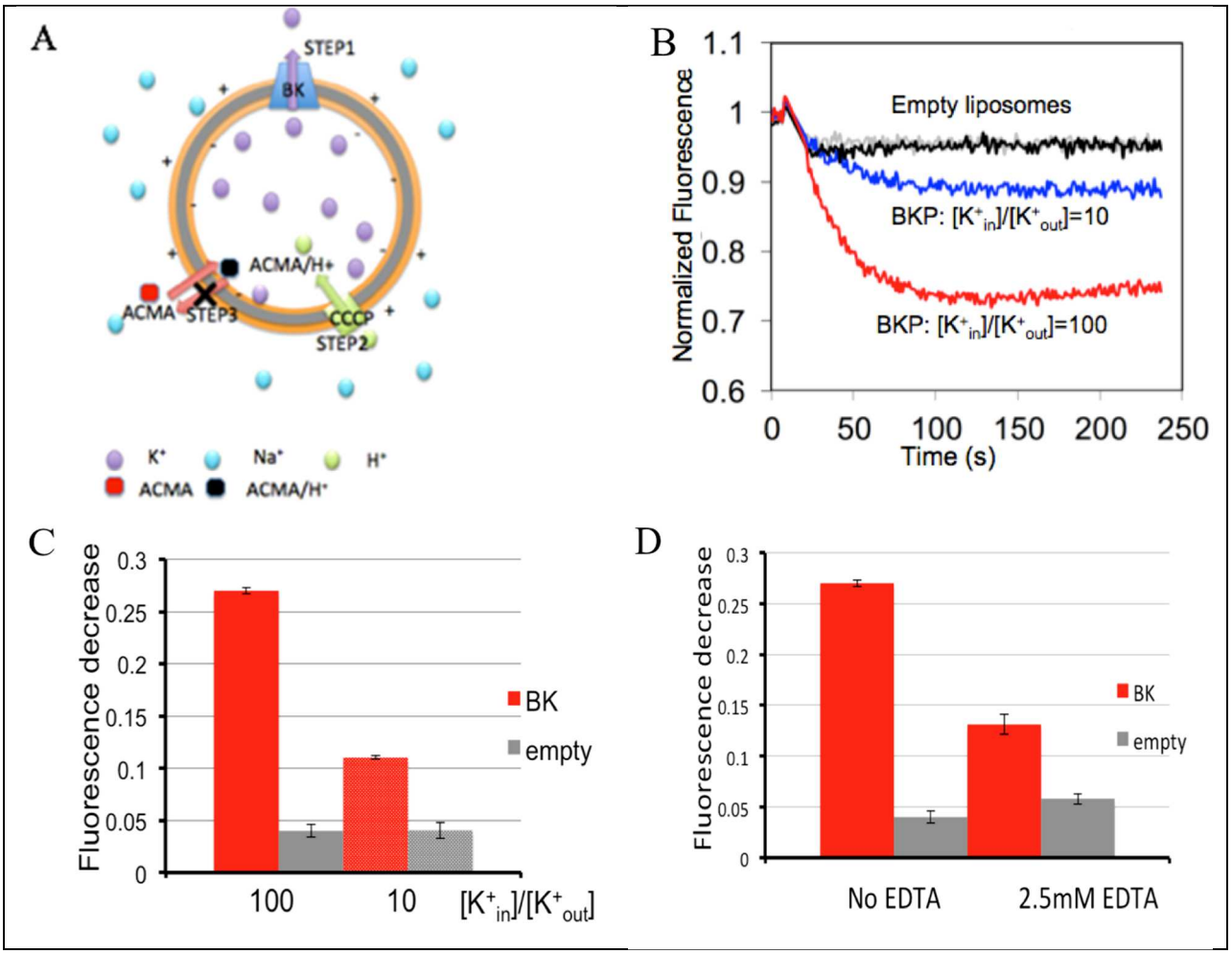

Figure 3.3 BK flux assay (A) Schematic representation. Liposomes (cyan) containing CCCP (proton ionophore) and BK channels were loaded with 150 mM KCl and diluted into the flux buffer containing 2 μM ACMA and 150 mM NaCl. (B) Representative fluorescence profiles showing the ACMA fluorescence quenching upon the addition of CCCP and with a100-fold and 10-fold potassium gradient. (C) Quenching percentages for proteoliposomes and empty liposomes with 100-fold and 10-fold potassium gradient. (D Quenching percentages for proteoliposomes and empty liposomes without or with EDTA added to the external solution.

As shown in Figure 3.3.A, at first a negative potential is established inside liposomes due to the exit of K^+ ions via BK channels. On the second step, protons flow down the electrical gradient via the protonophore (i.e. entering liposomes), carbonyl cyanide 3-chlorophenylhydrazone (CCCP). Finally, the fluorescence signal of ACMA is quenched by the pH change. When the K^+ gradient was decreased from 100 fold to 10 fold across the membrane, the transmembrane potential was expected to be about -60 mV, which would result in smaller quenching of ACMA. As physiological ligand Ca^{2+} opens BK channel, eliminating of free Ca^{2+} in the external solution by adding EDTA was expected to close the inside-out BK channels. These are exactly what have been observed. These results indicate that our reconstituted BK channels were functional.

3.2.3 Transmembrane Potential can be applied to liposomes

To confirm the absolute amplitude of the transmembrane potential, we used the hyperpolarization- activated cyclic nucleotide-gated (HCN2) channel as a model protein. HCN2 channel belongs to HCN family and the superfamily of voltage-gated potassium channels. The half-maximal voltage ($V_{1/2}$) is –94 mV for HCN2. When the transmembrane potential is lower than -120 mV, almost all the channels will be open.

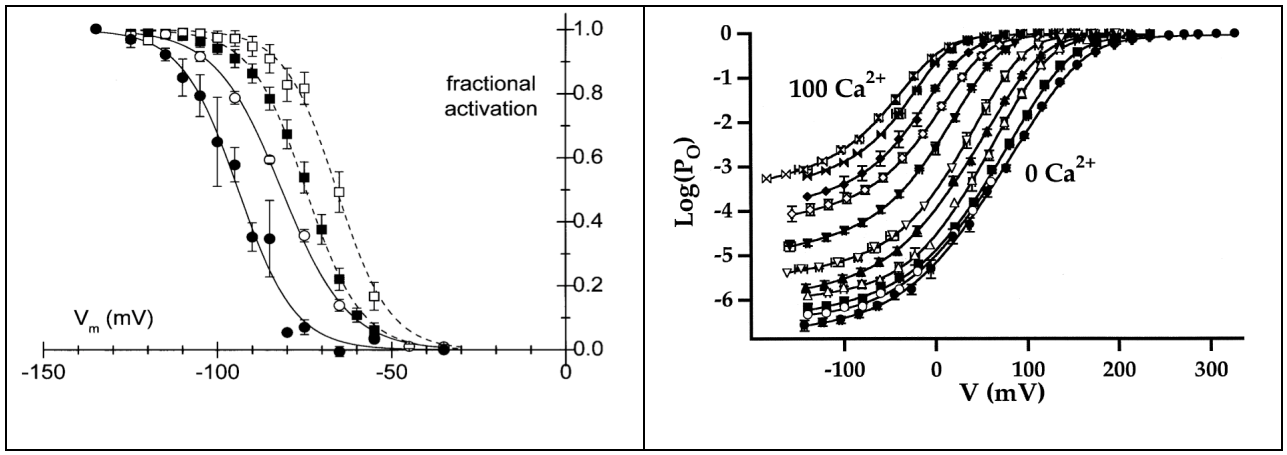

Figure 3.4 Voltage dependence of expressed HCN and BK. (left) Fractional activation curves of HCN2 (closed symbols) and HCN4 (open symbols) expressed in newborn cardiac myocytes (squares) and HEK 293 cells (circles) [58] (right) Fractional activation curves of BK with 0 -100 uM Ca^{2+} [59].

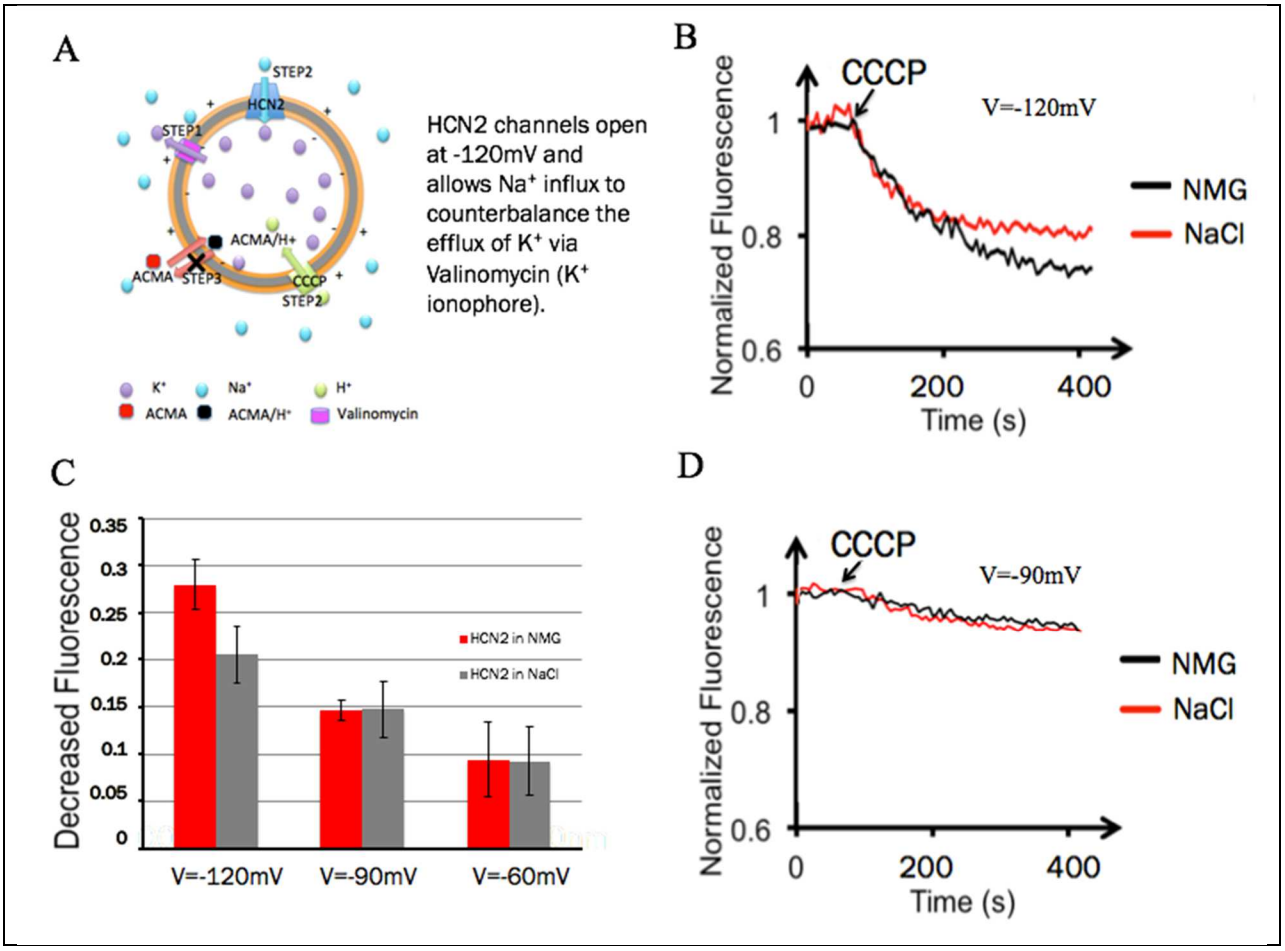

Figure 3.5 Validation of transmembrane potential. (A) Schematic of the HCN2 flux assay. Liposomes (cyan) containing Valinomycin (K^+ ionophore), CCCP (proton ionophore) and HCN2 channels were loaded with 150 mM KCl and diluted into the flux buffer containing 2 μM ACMA and 150 mM NaCl. (B) Representative fluorescence profiles showing the ACMA fluorescence quenching upon the addition of CCCP and valinomycin at -120 mV. (C) Quenching relation with different voltage. (D) Representative fluorescence profiles showing the ACMA fluorescence quenching upon the addition of CCCP and valinomycin at -90 mV.

To trigger the opening of HCN2 channels, HCN2 proteoliposomes containing 150 mM KCl were 100-fold/30-fold/ 10-fold diluted into buffer containing 150 mM NaCl or NMDG. And according to Nernst equation, this yielded transmembrane voltage of -123 mV/ - 92 mV/ -61 mV. With the addition of valinomycin, a potassium gradient was established. When the transmembrane potential was lower than -120 mV, HCN2 channels were open and Na^+ would flow inside to counterbalance the K^+ efflux and yielded a difference in NMDG and KCl group. However, when

HCN2 channels were kept closed due to depolarized transmembrane voltage, protons would flow into the liposomes, resulting a fluorescent signal quenching and no difference was observed. In summary, BK channels were proven to be functional on BK proteoliposomes and the amplitude of the transmembrane potential has been determined using the hyperpolarization-activated cyclic nucleotide-gated (HCN2) channel as a model protein. The liposomes remained intact and did not leak, thus the transmembrane potential held. This proves that the RSC method can be used to trap voltage-gated ion channels and voltage-sensitive proteins in desired functional states for structural analysis.

3.3 Materials and Methods

1-palmltoyl-2-oleoyl-sn-glycero-3-phophocoline (POPC) and 1-hexadecanoyl-2-(9Z-octadecenoyl)-sn-glycero-e-phospho-(1'-rac-glycerol) (sodium slat) (POPG) were from Avanti (Alabaster, Alabama). Valinomycin, 9-amino-6-chloro-2-methoxy acridine (ACMA) and Carbonyl cyanide 3-chlorophenylhydrazone (CCCP) were from Sigma Aldrich (St. Louis, MO). 8-Hydroxypyrene-1,3,6-Trisulfonic Acid (HPTS) and p-xylene-bis-pyridinium bromide (DPS) were from Invitrogen (Calrsbad, CA). Iberiotoxin was from Abcam (UK). Concentrator Amicon Ultra-4 and Amicon Ultra-2ml with 100KD cut-off were from MilliporeSigma (Burlington, MA).

3.3.1 Liposome swelling

To make liposomes as round as possible, a serial of small osmotic shocks are introduced by adding Milli-Q water to liposomes solution. For a 5-step swelling procedure, the added water volumes compared to the initial liposome solution volume are 11%, 14%, 18%, 24%, 33%. After each step of water addition, the sample is mixed by pipetting up and down and stays still on ice for at least half an hour.

3.3.2 Liposome leakage assay

To assess whether the K^+ gradient across the lipid membrane is decreased during the dilution of liposomes into a low K^+ solution, the leakage assay is carried out as previously described [60]. Briefly, POPC lipid in chloroform was dried and rehydrated with buffer containing 35 mM HPTS and 50 mM DPX with a lipid concentration at 10 mM. Then the lipid suspension was freeze-thaw for 10 times and run through a Mini Extruder (Avanti, Alamaba) with 50 nm Polycarbonate membrane filter for 20 times. The untrapped dye and quencher were removed by buffer exchange process. The fluorescence signal of HPTS can be detected once the liposome intact structure is disrupted with excitation wavelength at 550 nm and emission wavelength at 575 nm.

3.3.3 Liposome flux assay

POPC and POPG (1-palmitoyl-2-oleoyl-sn-glycero-3-phospho-(1'-rac-glycerol)) lipid mixture (3:1 molar ratio) in chloroform was dried under nitrogen for 30 min, and rehydrated and sonicated in Fisher Scientific FS20H Ultrasonic Cleaner (Fisher Scientific, Hampton, NH) in buffer A (20 mM HEPES, pH 7.3, 150 mM KCl) to a final lipid concentration at10 mM. The resulting solution was then mixed with purified BK channels to a final protein mixture containing 0.2 mM lipid and 4 mM DM. The mixture was rotated at 4 °C for 1 hour. Then detergent was removed by dialysis against the buffer A at 4 °C for 3-7 days (one day for each buffer change) in a 12-14 kDa cut-off dialysis membrane bag. Empty liposomes were prepared in the same manner without the addition of protein prior to dialysis.

To establish potassium gradient at 100 or 10 times across the membrane, empty liposomes or proteoliposome were 100-fold diluted into a buffer B containing 150 mM NaCl, 20 mM HEPES, pH 7.3 or buffer C containing135 mM NaCl, 15mM KCl, 20 mM HEPES, pH 7.3. ACMA stock

was added to a final concentration of 2 μM. Fluorescence intensity was measured every 1 sec using a Fluorolog®-3 Spectroflorometer (HORIBA Scientific, Edison, NJ) for a total of 800 sec with excitation at 395 nm and emission at 490 nm. CCCP was added to a final concentration of 1 μM after the first 100 s since ACMA addition, and valinomycin was added to a final concentration of 20 nM at 450 second. For EDTA experiments, 500mM EDTA-Na2 stock was used to bring the concentration of EDTA in the external solution to 2 mM.

3.3.4 Buffer exchange process for liposomes

To change the external solution for liposomes, one easy way is to use a concentrator. As the size of liposomes is larger than 50 kDa, 50 kDa cut-off concentrator is sufficient to separate the liposomes from the micelles. After washing of the concentrator with water and buffer A, around 2 ml of liposome solution in buffer A was added to the concentrator. The concentrator was centrifuged at 2 kg for 5 min. Then another 1.6 ml of buffer B was added and mixed with the left solution in the concentrator. Repeat this centrifugation and mixing steps for a few times until less than 0.1% of initial buffer A was left in the concentrator.

3.3.5 Liposome with bi-ionic buffer and valinomycin

To establish the negative potential, bi-ionic buffer condition that high concentration of KCl and high concentration of NaCl separated by lipid bilayers would be used. BK proteoliposomes for my structural study were formed by gel filtration using 150 mM NMG and 20 mM HEPES at pH 7.3 as running buffer. Empty liposomes for flux assay were formed by dialysis against 150 mM KCl, 20 mM HEPES buffer at pH 7.3. Then the buffer outside the liposome was exchanged to KCl solution with the same ionic strength for proteoliposomes or to NMG buffer for empty liposomes using a concentrator. Valinomycin was added to the liposome solution at valinomycin: lipid molar ratio at 1: 200. Then BK proteoliposomes were concentrated and swelled for cryo-

EM sample preparation and empty liposomes were used directly by adding ACMA and CCCP for flux assay without further dilution.

Chapter 4. Cryo-EM sample preparation for structural studies of BK

4.1 Introduction

Acquiring protein particles in liposomes for my project was challenging because the low yield of hBK expressed in HEK293 cells. For one purification process, 300 dishes of HEK293 cells grown in 150 mm Petri dish were used. Roughly 100ug of BK protein in the form of proteoliposomes was eluted in 4.5 ml of elution fractions after gel filtration from a 24 ml Sephadex G50 column (10 mm I.D x 300 mm height). The lipid concentration of proteoliposomes concentration was ~0.05 mM. If I follow the standard cryo-EM sample freezing method[61], that is, applying sample to a holey carbon grid once and blot immediately, there is hardly any liposomes in the holes. Single-particle reconstruction of cryo-EM specimens typically requires the acquisition of thousands of micrographs. To conquer the problem that liposomes don't go inside of holes, I have tried homemade substrates on traditional holey grid: either by growing crystal *in situ* or by floating an ultra-thin layer of continuous carbon on the holey carbon grids. Both methods increased the number of liposomes per image dramatically. A structure of BK was obtained at 8.1 Å with the help of crystal substrate.

Inspired by the multiple-blotting work[62], I applied the low concentration liposome sample multiple times, the density of particles was still not satisfactory and the low amount of proteoliposomes sample limits how many grids can be prepared each time. After lots of testing on empty liposomes, a simple method was developed. Only 2 µl of 2 mM liposome sample is required for one grid. Facilitated by this discovery, a 3.5 Å BK structure was determined.

4.2 Results and discussion

4.2.1 Using substrate to increase liposome density

Streptavidin is a 52.8 kDa protein with high affinity for biotin. Two-dimensional streptavidin crystals were proved to tether proteoliposomes decorated with biotinylated lipids to increase the proteoliposomes density in single images[63]. As shown in Figure 4.1.A, liposomes (1000:1 mol/mol POPC: biotincapped DOPE) were immobilized on streptavidin crystal after 3 min tethering in 100% humidity environment and the density of liposome was ~800 liposome/μm^2.

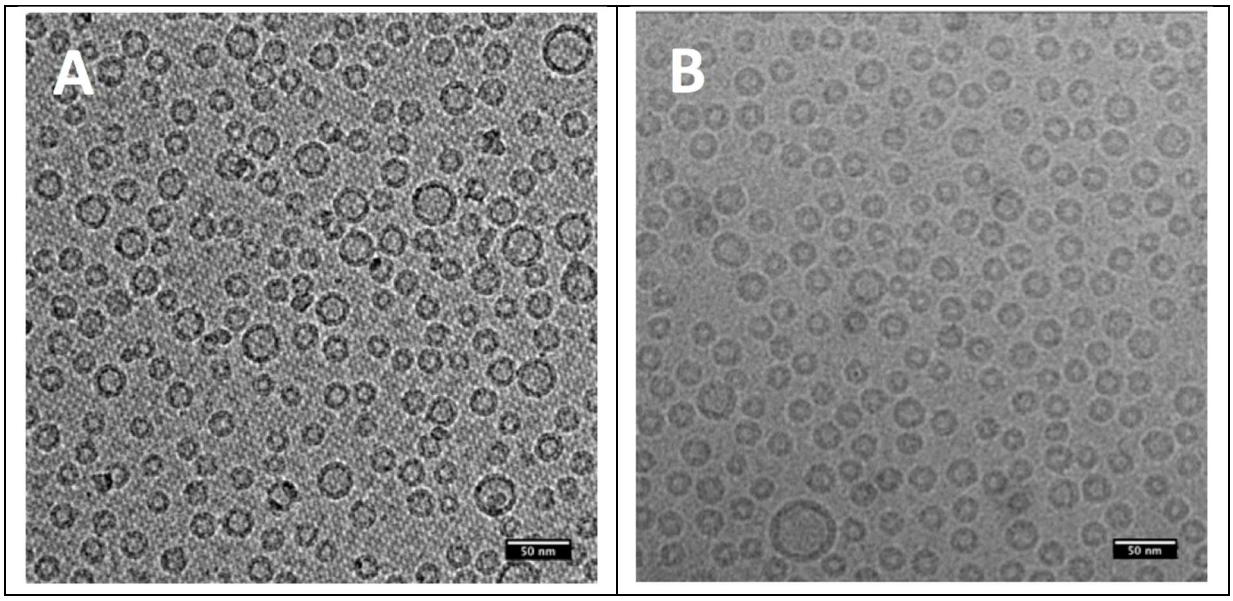

Figure 4.1 1mM liposome distribution (A) on 2D streptavidin crystal grid (B) on carbon grid with 3 min incubation.

Ultra-thin layer of carbon can also be used to increase the liposome density. As shown in Figure 4.1.B, let the liposome sample stay on a glow-discharged carbon grid for 3 min in 100% humidity environment yielded liposomes ~800 liposome/μm^2 in each image.

I also tried different wait time (incubation time), that is, the time between applying sample to grid and blotting. By increasing the incubation time from 15 s to 15 min, I can make 0.2 mM

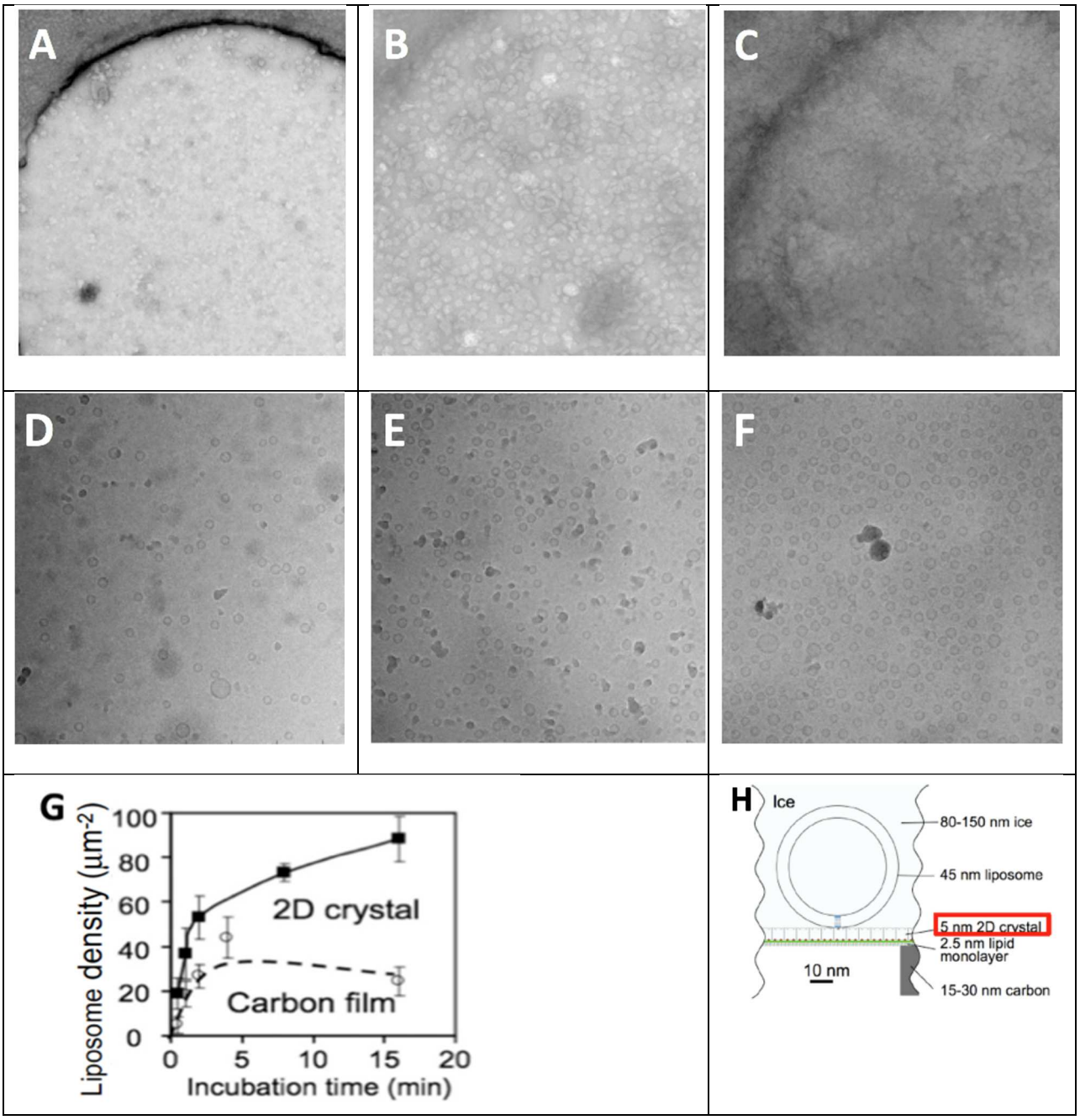

Figure 4.2 The dependence of average liposome density on the incubation time (A-C) Negative stained images of 0.2 mM liposomes incubated on crystal for 5 min, 10 min and 30 min. (D-F) Cryo-EM images of 0.2 mM liposomes incubated on continuous carbon for 1 min, 3 min and 6 min. All images from A to F have a dimension of 1.8 um*1.8 um. (G) Liposome (around 1 mM with DPhPC:biotin-capped DPPE 1:3600) density curve on crystal and carbon[63] (H) Cartoon showing the architecture of liposome tethering on crystal.

liposome (5 times diluted) solution collectable for Cryo-EM for both 2D crystal or streptavidin substrate. Previous study[63] showed the same trend as shown in Figure 4.2.G.

4.2.2 Using multiple blotting to increase liposome density

A study[62] has shown when sample were applied multiple times prior to freezing, more particles can go inside of the hole for a range of samples including octahedral protein cage O3-33, human adenovirus, coronavirus MHV spike glycoprotein ectodomain and yeast glucokinase-1.

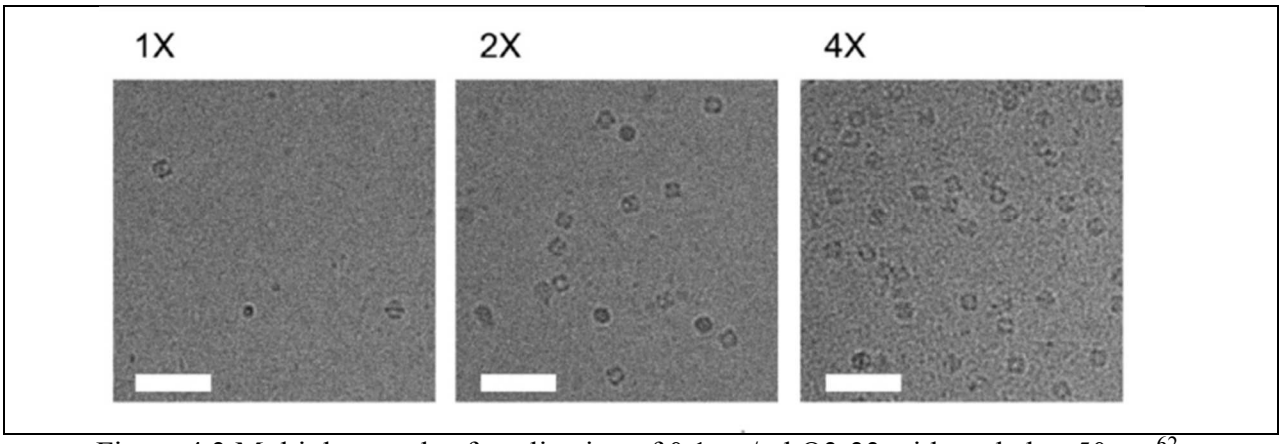

Figure 4.3 Multiple rounds of application of 0.1mg/ml O3-33 with scale bar 50 nm[62].

It's well known that liposomes are less likely to go inside holes. Instead, they tend to stay on the carbon region. I used the new multiple blotting technique with two sets of empty liposomes to optimize the procedure both at 2 mM phosphatelipid concentration. Their average diameters are similar to those of BK proteoliposomes generated by dialysis and by gel filtration. As shown in Figure 4.4, liposome A (also noted as E in the figures) has an average diameter at 54 nm, produced by extrusion through 50 nm polycarbonate

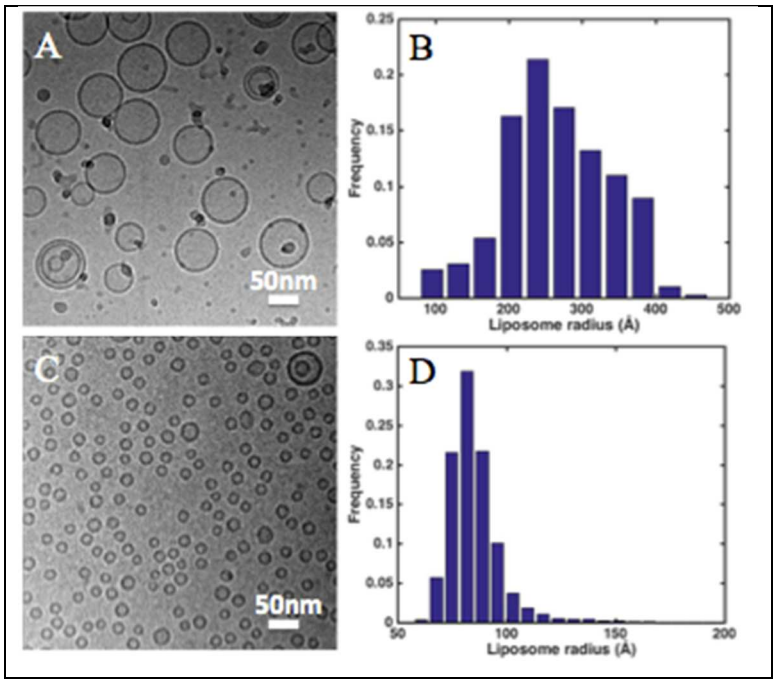

Figure 4.4 Cryo-EM images and histograms of (A&B) liposome A (C&D) liposome B.

membranes while liposome B (also noted as G in the figures) produced by gel filtration has an average diameter at 18 nm. As their phospholipid concentration is the same, the concentration of liposome is differed by 9 times, that is, liposome A has a liposome concentration at 66 nM (3.97×10^{16} liposome/L) while liposome B has a liposome concentration at 590 nM (3.55×10^{17} liposome/L). Liposome solution A or B was added to glow discharged holey grids and blotted immediately (15 s in between adding sample and blotting) before freezing or adding more rounds of liposome solution. After applying the liposome solution A or B three to six times, the liposome density increased to some extent compared to applying liposome solution once. As particle density should be around 300 – 1500 particles/μm^2 in hole region for cryo-EM data collection, multiple rounds of the sample application and blotting for liposomes might reach the lower end of requirement for particle density, but it is still not satisfactory.

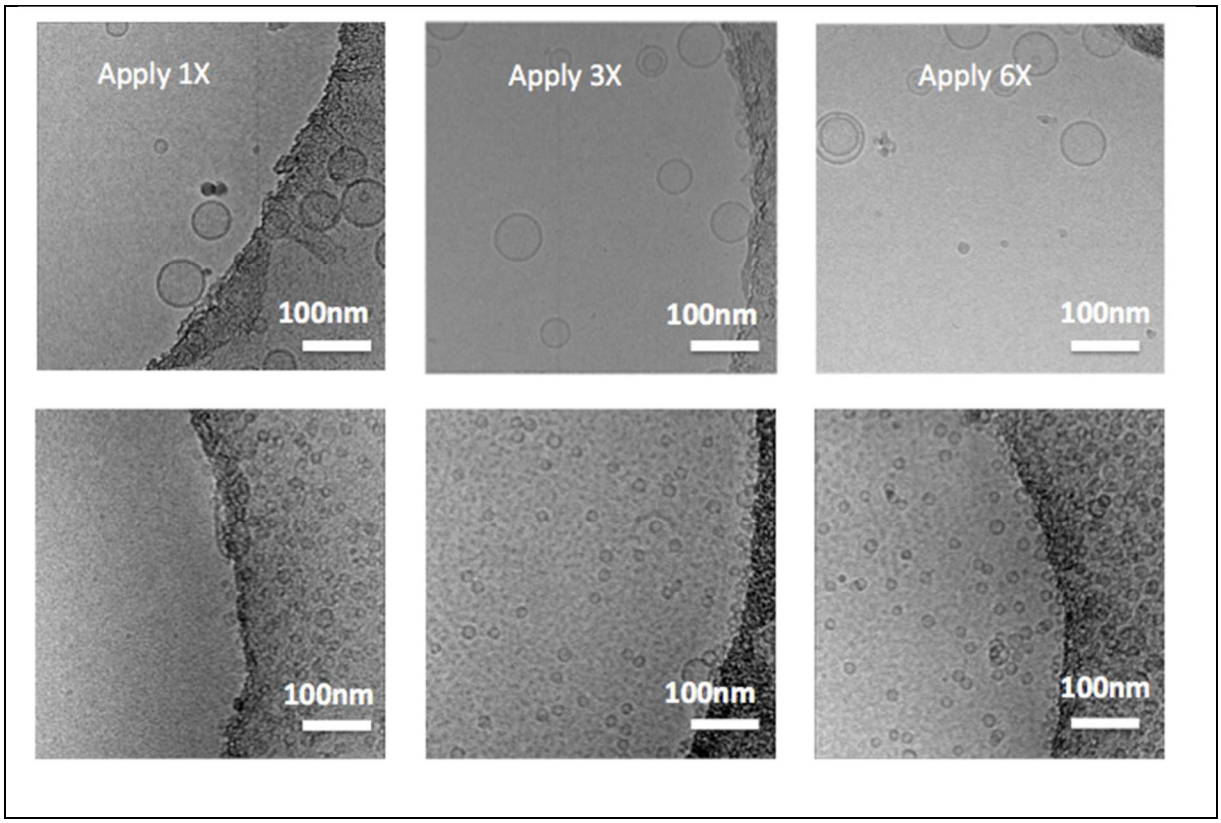

Figure 4.5 Upper row: apply liposome A once, three and six times. Lower row: apply liposome B once, three and six times.

4.2.3 Elongating wait time to increase liposome density

When use the multiple blotting technique as described previously, liposomes were still reluctant to populate the holes and remained adsorbed on the carbon region. However, when I increased the wait time from 1 min to 10 min, the liposome density inside of the holes increased dramatically for both liposome A and liposome B as shown in Figure 4.6.

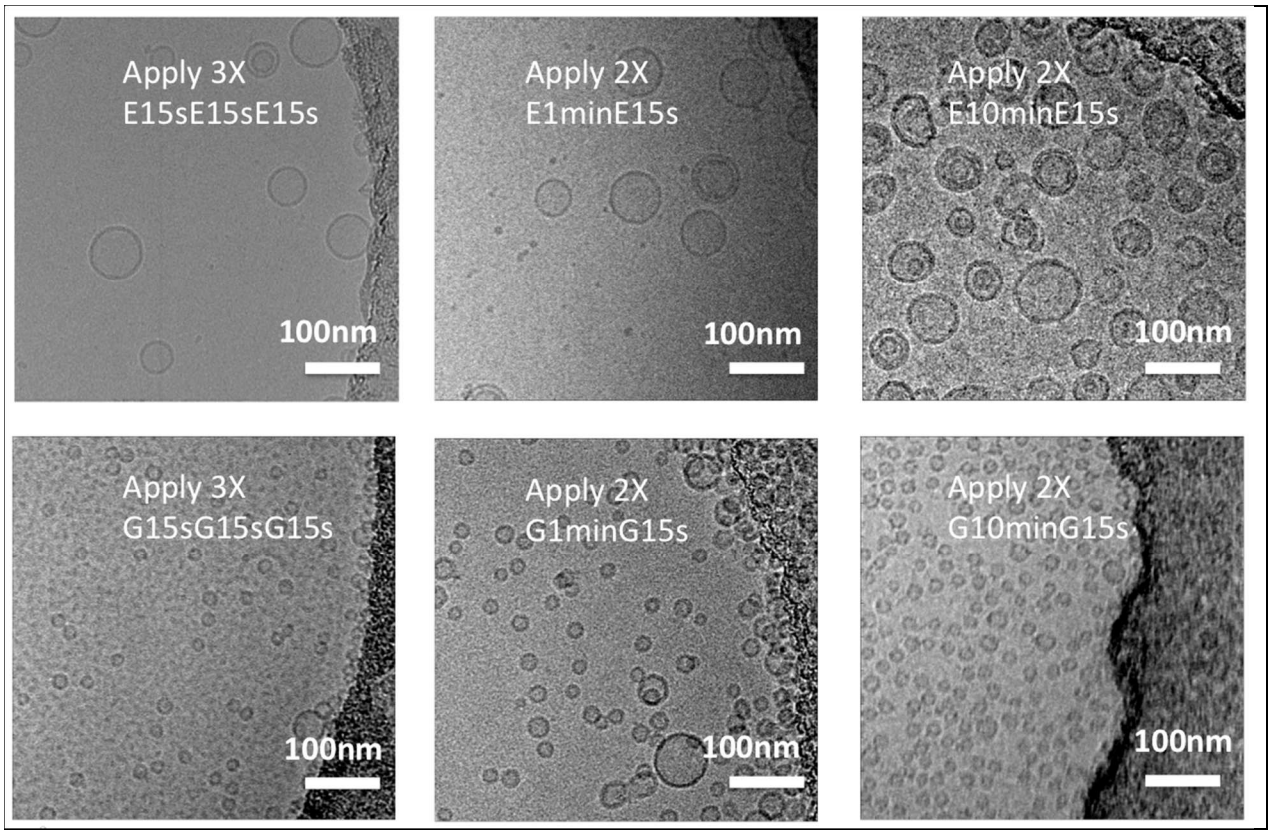

Figure 4.6 Increased wait time improves particle density. The upper row shows applying liposome A three times with 15s wait time and twice with 1 min and 10 min wait time. The lower row shows applying liposome B three times with 15s wait time and twice with 1 min and 10 min wait time.

To track whether the increased liposomes came from the first round or the second round of sample application, I applied liposome A in the first round of sample application and liposome B in the second round. Three different wait time: 1 min, 5 min and 10 min were tested.

From Figure 4.7, it is observed that when wait time was 1 min, the carbon region of grid was not fully occupied by liposomes and neither big (liposome A) or small (liposome B) liposomes

populated in the holes. With longer wait time, the carbon region became saturated, and more and more liposomes went into the holes. With longer wait time, the liposomes distributed more towards the center of the hole.

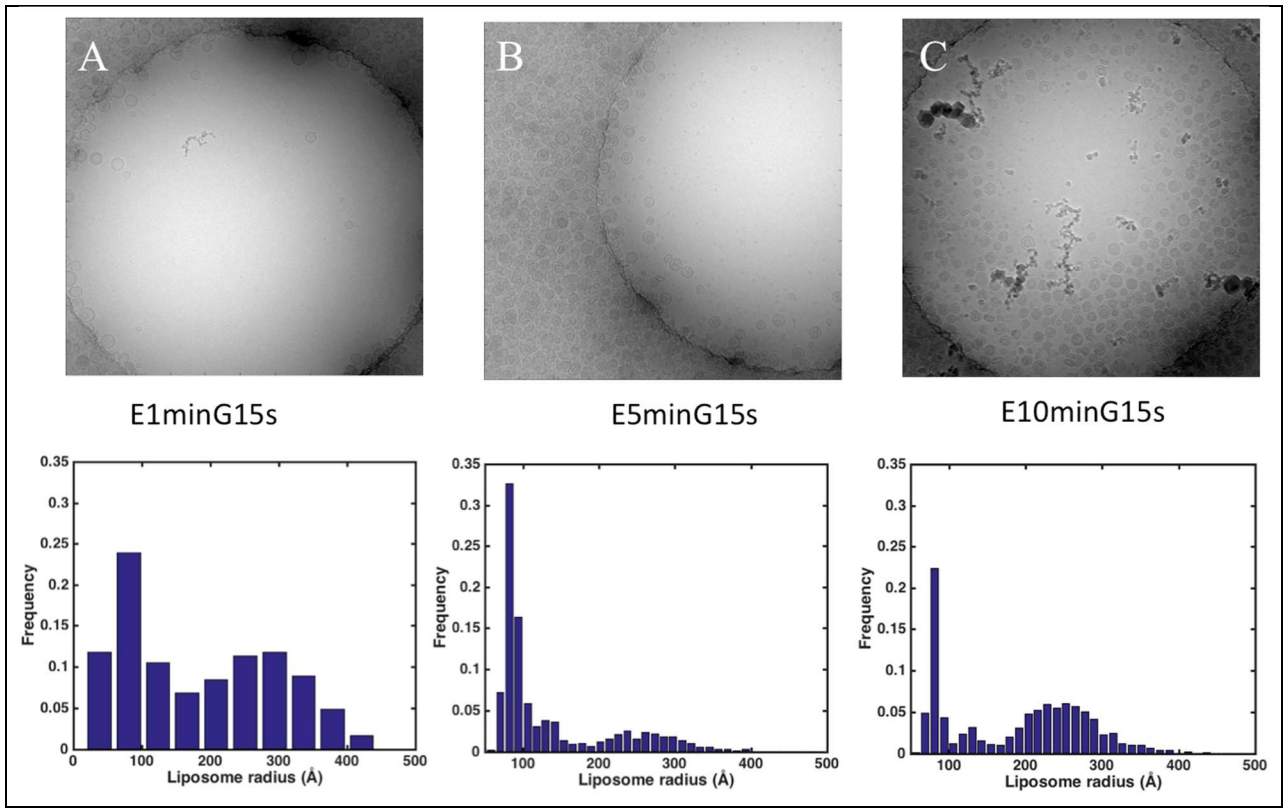

Figure 4.7 Cryo-EM image representatives and histograms calculated from 5 holes of sample prepared with (A) 1 min (B) 5 min (C) 10 min wait time. Holes are 2 um in diameter.

In addition, there was a shift of liposome size among different wait time. With longer wait time, there were more large liposomes. As the diameter of liposome A and B differs a lot as shown in Figure 4.4, the overlap of size is negligible. Thus, I assigned liposome with a diameter larger than 30 nm to liposome A and smaller than 30 nm to liposome B. In this way, whether the increased liposomes came from the first round of sample application or the second round of sample application can be answered.

Interestingly, as Figure 4.8.B illustrated, when the wait time increased, liposome A coverage in the hole increased up to 18%. As for liposome B,the coverage of the hole only increased to 2 %

from 0.1% with longer wait time. And the counts of liposome B for 5 min and 10 min samples were very similar, with 235 (± 61) for 5 min and 202 (± 30) for 10 min. The reason might lie in that when wait time is only 1 minute, the carbon region is not fully saturated so some liposome B from the second addition will need to go to the carbon region. While for 5 min and 10 min samples, both carbon regions were saturated so the amounts of liposome B in the holes were similar.

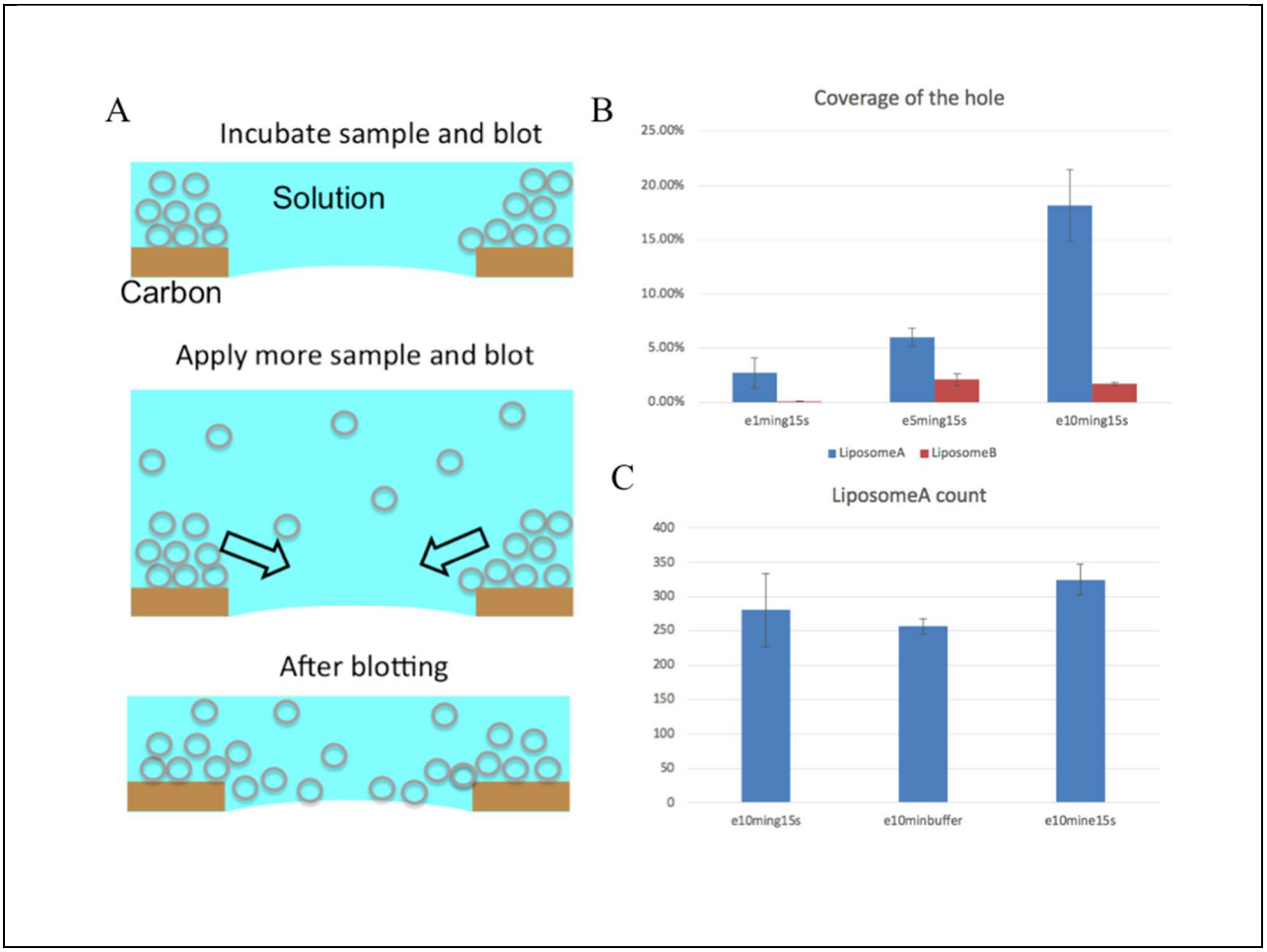

Figure 4.8 Liposome distribution during multiple blotting (A) cartoon showing the hypothesis (B) liposome A and liposome B coverage percentage with different wait time (C) liposome A average counts with different second application condition.

Our hypothesis why liposome A populated with longer wait time is that liposome A occupied all carbon regions and then started to pile up during the wait time in the first round. Then the newly added liposomes B distributed equally inside and outside of the holes. When the grid was blotted

finally, the piled-up liposome A were flushed to the holes, resulting in an increased number of liposome A (Figure 4.8.A). In summary, we thought that it might not be the addition of the second round of sample but the force introduced by blotting that increased liposome A into the holes.

To further test this hypothesis, I used buffer instead of liposome A solution for the second application (Figure 4.9) and compared the result with another round of liposome application. Decent number of liposomes was seen inside the hole in both cases. As Figure 4.8.C showed, the counts of liposome A with liposome B, buffer and liposome A are 280 (±53), 256 (±11) and 325 (±22). With liposome A as the second application, the average liposome A count was only slightly bigger.

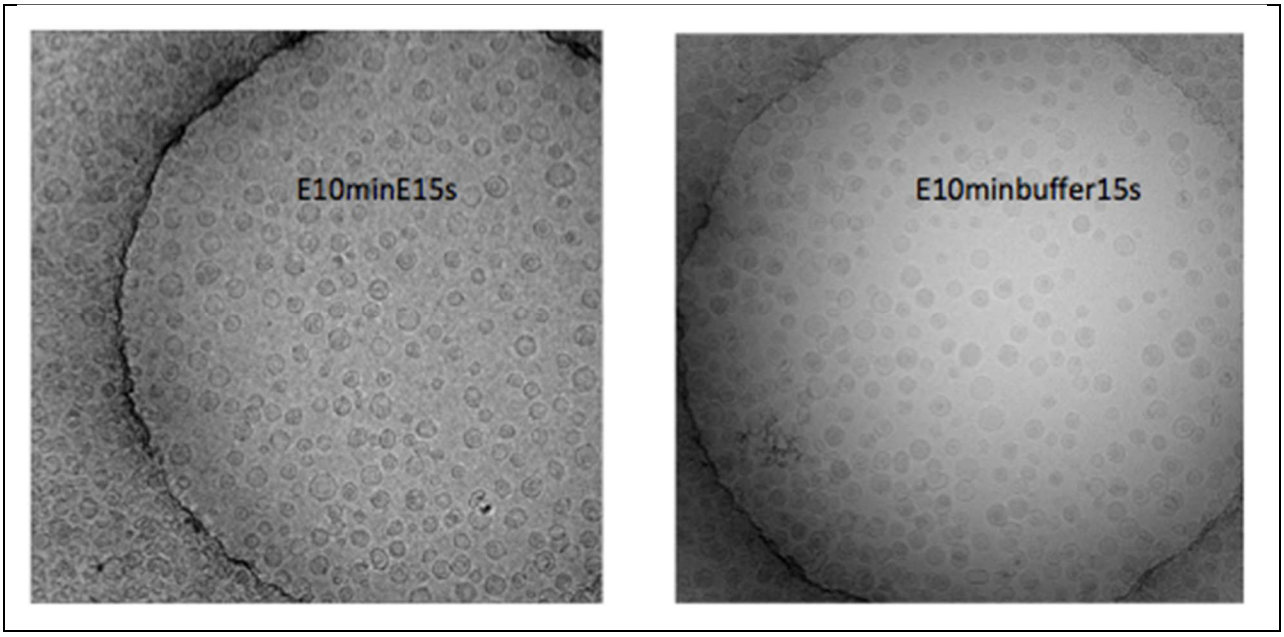

Figure 4.9 Cryo-EM images of liposome A with 10 min wait time and (A) liposome A (B) buffer as the second application. Holes are 2 um in diameter.

It's worth noting that although the Vitrobot (FEI, OR) was set up at 100% humidity, the open of the chamber for tweezers movement and some inaccuracy in humidifier made the actual humidity less than 100%. As long as the relative humidity is less than 100%, there will be net water transport from the specimen to the environment (dehydration). One easy fix for the small

osmotic imbalance is to add buffer or sample with slightly lower salt concentration. The concentration change can follow the 5-step swelling gradient: 11%, 14%, 18%, 24%, and 33%.

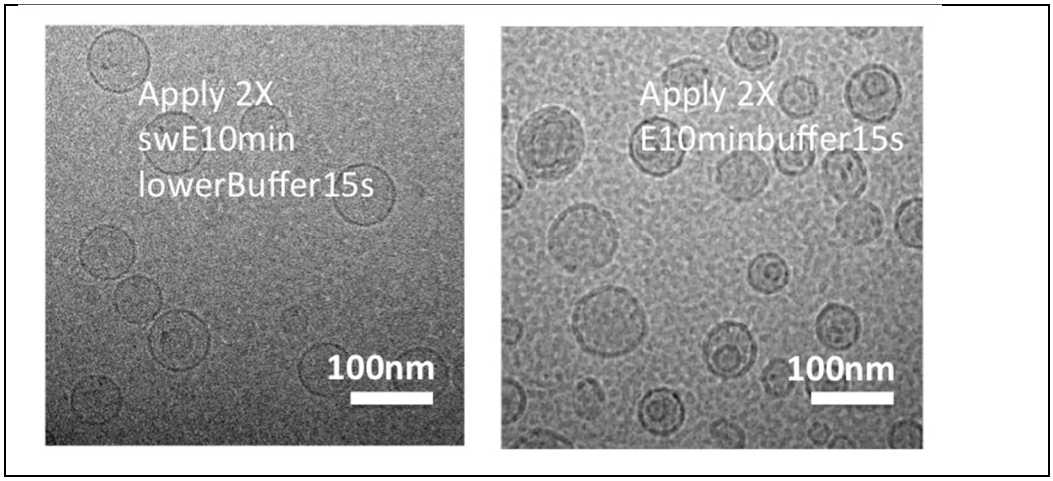

Figure 4.10 Cryo-EM images of 4-step swelled liposome A with addition of 50% buffer and nonswelled liposome A with 100% buffer.

4.2.4 Applying vitrification methods to BK proteoliposomes

To compare the image quality for different grids, the same BK proteoliposomes sample at 1 mM lipid concentration was applied to 2D streptavidin crystal, continuous carbon grids as well as holey grid with increased wait time. All three conditions were imaged at 62 e/ $Å^2$. As shown in Figure 4.11.A and B, only a few liposomes show strong signal of protein particles. Compared with 4.11.C where most of the liposomes show 1-3 particles per liposome, only 1/6 of liposomes on Figure 4.11.A shows particles. One possible reason is the tendency of liposome tethering might be greater for empty liposomes than for proteoliposomes so that empty liposomes get concentrated on the crystal substrate. Also, from previous BK data analysis, several classes of bound and free streptavidin would appear in the classification as shown in Figure 4.12.

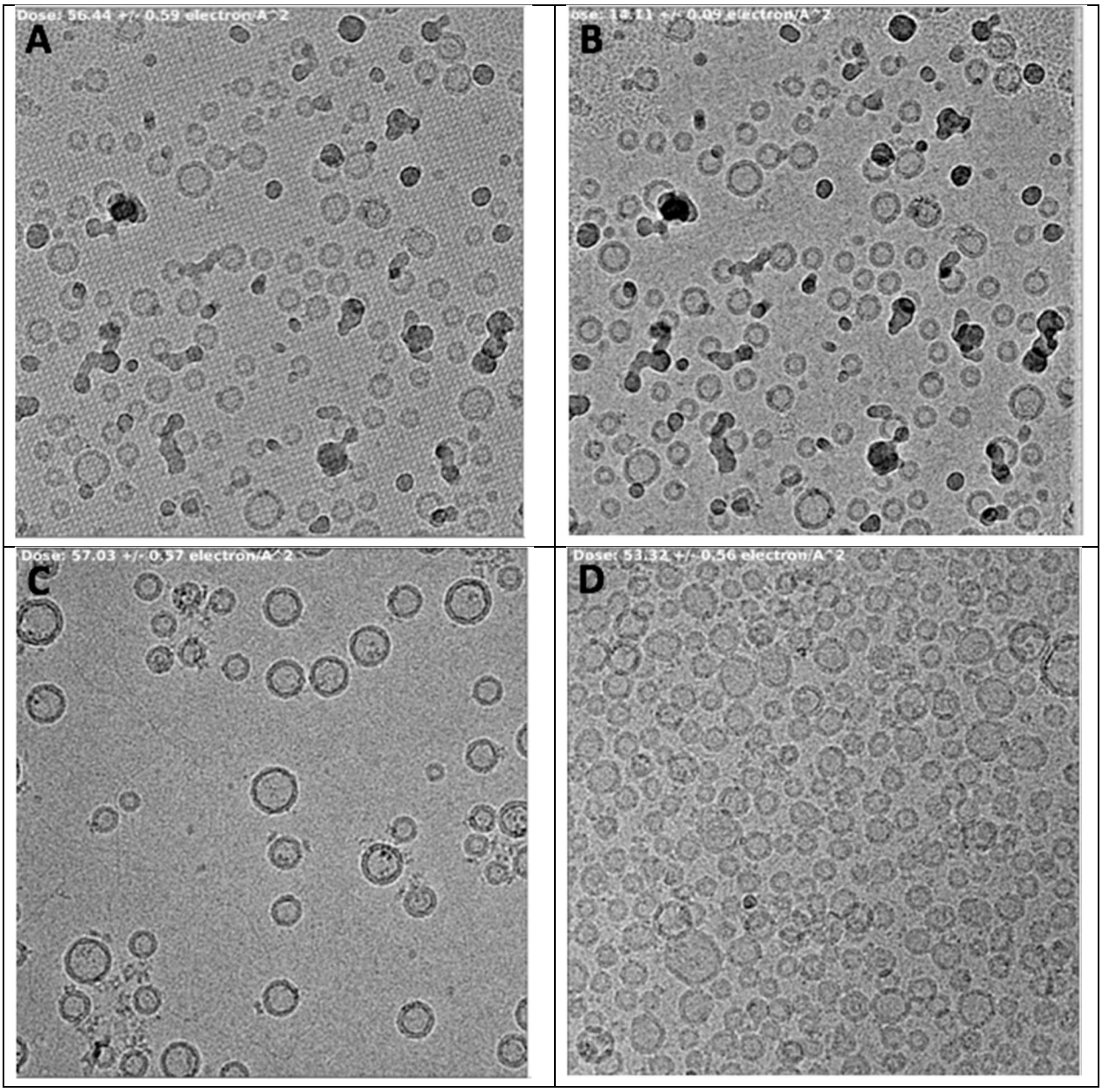

Figure 4.11 1 mM BK proteoliposomes (A) on 2D crystal (B) on 2D crystal with crystal information subtracted from the image (C) in holey (D) on continuous carbon.

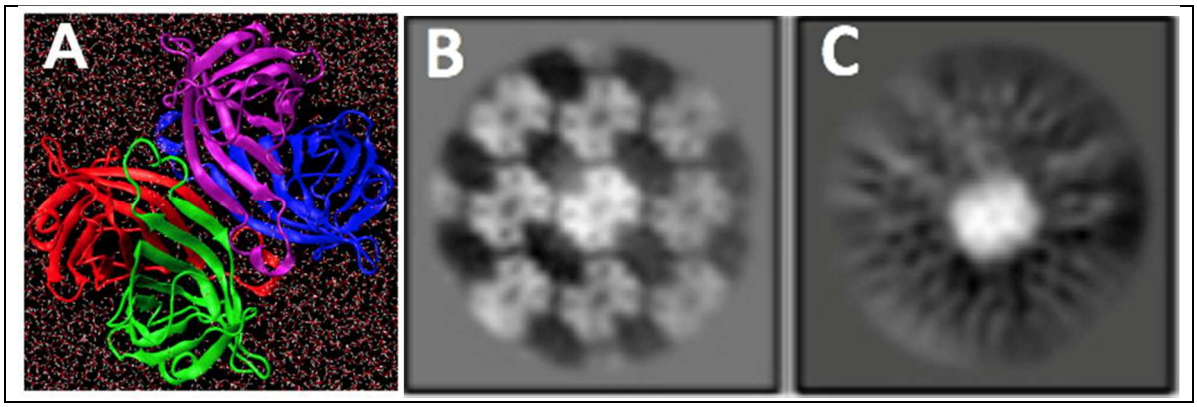

Figure 4.12 (A) Molecular representation of hydrated streptavidin tetramer with box size 5.82 nm[63]. (B & C) 2D class averages of (B) streptavidin crystal (bound streptavidin) (C) free streptavidin. Box size is 32nm.

As shown in Figure 4.11.D, most of the particles identified were in the side views but particles in the top views was hard to find. Also, the ice thickness in Figure 4.11.D should be thinner or similar to that of Figure 4.11.C, so the extra loss electron came from the carbon substrate. Study has shown when the ice thickness increases from 300 Å to 450 Å, the obviously detectable protein particles become undetectable in images recorded by a CCD camera[64]. As proteoliposomes were imaged instead of protein molecules themselves, the ice thickness was chosen to be thick enough to embed proteoliposomes, which results in the ice thickness between 300 and 800 Å, already in the thick range of cryo-EM sample. Having an extra layer of carbon makes the contrast even worse.

The final proteoliposomes cryo-EM sample preparation condition is applying 2 µl of 2 mM proteoliposomes to a glow-discharged CFlat grid once. After 7-10 min and blotting, another 2 µl buffer itself is applied before finally blotting and freezing. When collect data, energy filter can be used to increase the signal to noise ratio as the ice thickness is a little bit thicker. This effect has been studied extensively [65-69]. Energy filtering uses an aperture to remove inelastically scattered electrons, thus reduces background noise. Energy filtering also increases the amplitude

contrast of proteins embedded in amorphous ice from 2.7% to 6.9% [66]. Micrograph below is an example of BK proteoliposomes collected with energy filter.

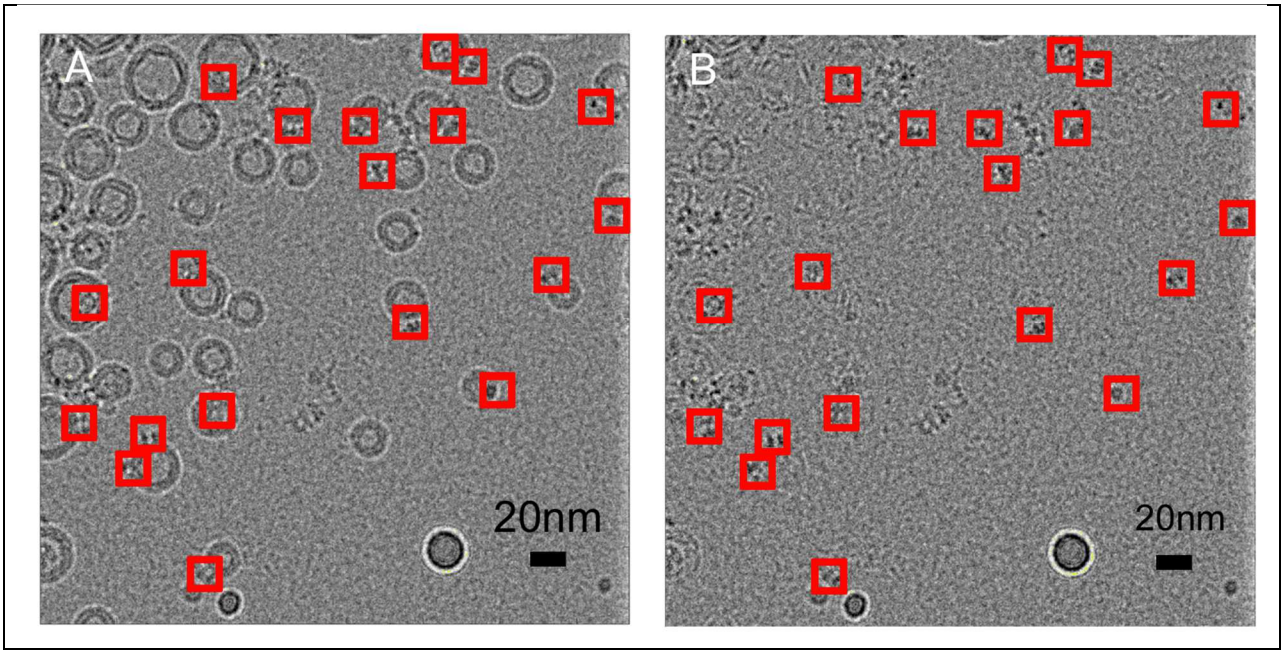

Figure 4.13 A typical micrograph of BK proteoliposomes before and after vesicle subtraction. Red boxes highlight protein particles.

As Figure 4.13 shown, the protein contrast is similar to the contrast of lipid bilayers on the micrograph before vesicle subtraction. The vesicle subtraction program subtracted membrane profile averaged from hundreds of empty liposomes. After computationally removal of vesicle signal as described before[41], only the signal of BK protein is left on the image. Figure 4.14 shows the 3D model of a liposome and a representative liposome from cryo-EM micrograph.

Particle picking and initial Classification will be carried out with the vesicle-subtracted images. More results of Classification and 3D reconstruction will be discussed in the next chapter.

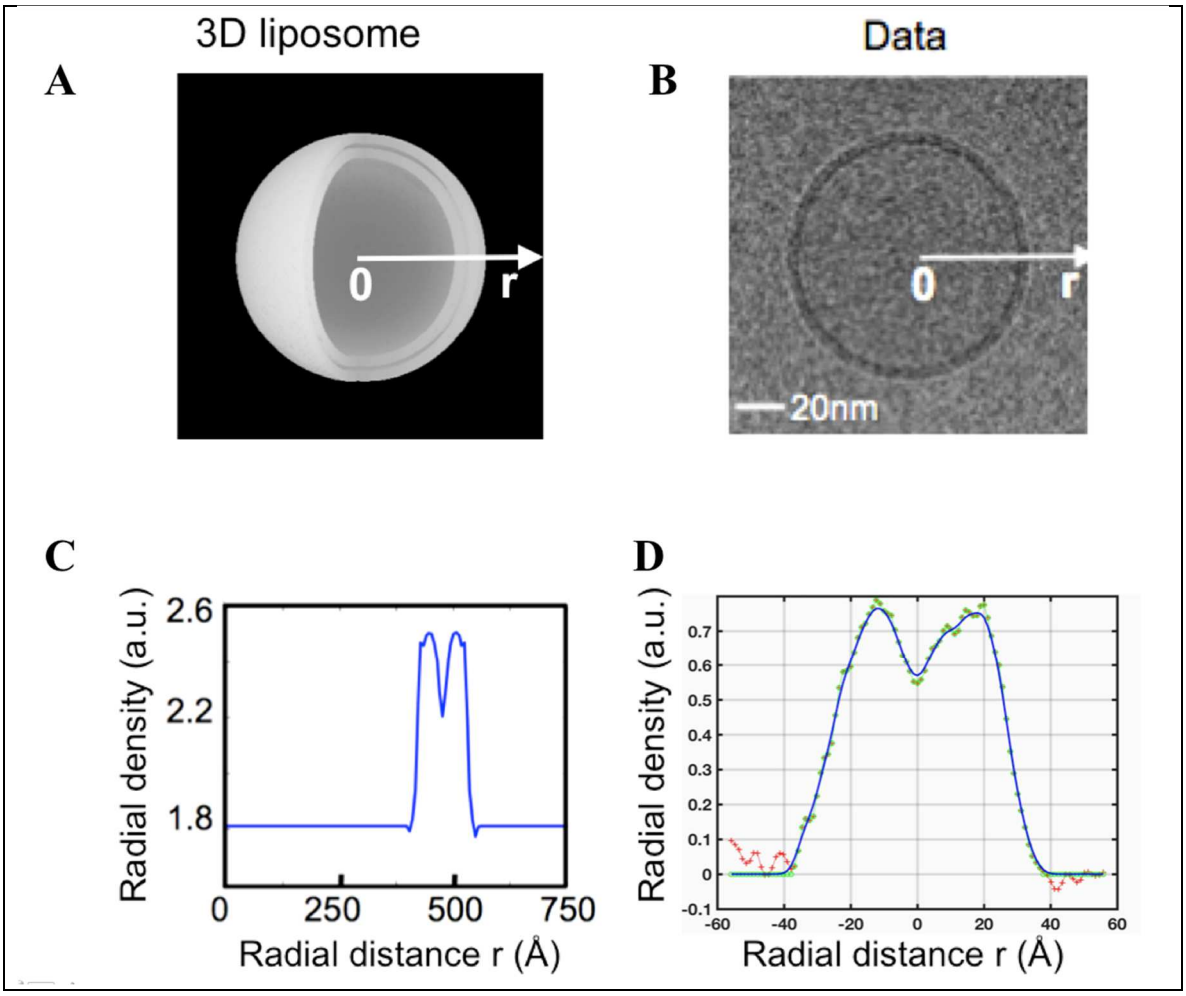

Figure 4.14 Vesicle models (A) 3D liposome model (B) liposome from real micrograph (C) radial average of 3D liposome model along z axis with the center of liposome as coordinate origin (D) membrane profile averaged from 200 liposomes with the center of bilayers as coordinate origin (red line is original data points, green line is data throwing away points out of bilayer region and blue line is filtered curve).

In conclusion, increasing wait time is cost-effective and simple enough to have desired density of liposome for cryo-EM studies. We believe this procedure will help people image liposomes and make liposomes system a more popular native environment for structural studies of membrane proteins.

4.3 Materials and Methods

Lipid 1,2-dioleoyl-sn-glycerol-3-phosphocholine (DOPC) and 1,2- dioleoyl-sn-glycerol-3-phosphoethanolamine-N- (Cap Biotinyl) (Sodium salt) (Biotincapped-DOPE) were from Avanti (Alabaster, Alabama). Streptavidin was from New England Biolabs (Ipswich, MA). CFlat R2/2 holey carbon grids and uranyl acetate powder were from EMS (Hatfield, PA). Quantifoil R2/2 holey grids were from Quantifoil Micro Tools GmbH (Germany). Continuous carbon grids were either homemade or from Zhongjingkeyi Films Technology (China).

4.3.1 Glow discharge

Continuous carbon grids or holey grids are put onto a 55 mm glass bottom dish with carbon side of the grids up. Place the glass dish into PELCO easiFlow Glow Discharge Cleaning System (Ted Pella, Redding, California) and apply 20 μA current for 20 s in vacuum to make the carbon surface hydrophilic.

4.3.2 Negative staining

Apply 4 μl of sample to the carbon side of a glow-discharged grid and wait for 1 min. Blot the excess solution then apply 4 μl of 2% uranyl acetate and wait another 1 min. Blot the staining solution completely and store the grid in a grid box in vacuum.

4.3.3 Vitrification and imaging

A FEI Vitrobot Mark IV vitrobot (FEI, Hillsboro, OR) is used to sample vitrification. Humidity is set at 100% at 22°C all the time. After applying 2 μl of liposome sample to a glow-discharged CFlat grid, we wait certain amount of wait time (1-10min) before using filter paper to adsorb excess amount of solution from the grid. Then another 2 μl of solution with or without liposome is applied to the grid and let on grid for 10-20s. The grid is then blotted and plunged

immediately. Samples were imaged on FEI G2 F20 (FEI, Hillsboro, OR) equipped with Eagle 4k camera (FEI, Hillsboro, OR), FEI T12 (FEI, Hillsboro, OR) equipped with a Gatan US4000 CCD camera (Gatan, Pleasanton, CA) and FEI G2 F20 (FEI, Hillsboro, OR) equipped with a Gatan K2 direct detector (Gatan, Pleasanton, CA).

4.3.4 Streptavidin crystal growth and liposome tethering

Two-dimensional (2D) streptavidin crystals were grown at room temperature as previously described[63]. Briefly, Quantifoil R2/2 holey grids were washed in hexane to remove polymer residuals. 4 µl of 0.5 mg/ml Streptavidin solution in 50 mM HEPES, 150 mM NaCl, pH 7.3 solution was applied to the grid with a layer of a lipid mixture (0.5 mg/ml DOPC and 0.5 mg/ml biotincapped-DOPE in chloroform) directly and kept on the grid in a humid chamber for 20 min. Then the grids were then washed 1 time in 50 mM HEPES, 150 mM NaCl, pH 7.3 solution and 3 times in 20 mM HEPES, 150 mM KCl, pH 7.3 which had the same contents as the running buffer for liposomes. Then the crystal was incubated with 8 µl of BK proteoliposome suspensions for 10-40 min to allow binding. The sample was blotted at room temperature and immediately fast-frozen in liquid ethane for cryo-EM. For negative staining, 4 µl of 2% uranyl acetate was added to the grid after liposome tethering and the excess solution was blotted after one minute.

4.3.5 Motion Correction

Raw image stacks recorded in super-resolution mode from K2 direct detector were motion corrected and binned by a factor of 2 using UCSF MotionCor2 algorithm[70]. Briefly, the program divided the image to 5*5 small windows and track movements between frames in each window. A weighting factor based on how many electrons have been exposed was applied to each frame.

4.3.6 Crystal and Vesicle subtraction computationally

The periodic 2D streptavidin crystal information was removed computationally as described[63], and the liposome membrane contribution was removed using a model based on the average POPC membrane profile from 200 liposomes. The model was obtained using the Hankel transform as described[71].

Chapter 5. Structure of BK in liposomes

5.1 Introduction

Here we expressed and purified the BK channels from HEK293 cells stably expressing FLAG-tagged human *Slo1* (*hSlo*), reconstituted them into lipid vesicles, and imaged using cryo-EM. The structure was being determined to 3.5 Å using the RSC method. The gating ring adopts C2 symmetry, which has not been observed in other *Slo* channels. This improvement in resolution from 17 Å[41] is largely due to the increased size of the dataset (more than 100,000 particles vs the ~8,000 used in previous study [41]), as well as the use of the direct-electron-detector camera to record cryo-EM images and the optimization of sample preparation procedure.

5.2 Results and discussion

5.2.1 Data Collection and image processing

Sample of swelled BK proteoliposomes were flash frozen in a Vitrobot MarkIV with 7-10 min wait times as Chapter 4 described. An FEI Titan Krios equipped with a K2 Summit Detector and Energy filter with a 20 eV slit was used for imaging. Micrographs were collected by K2 at super-resolution mode with pixel size at 0.525 Å/pixel and 0.2 s/frame for a total of 43 frames. The total electron dose was 60 e/Å^2 and dose-fractionated super-resolution image stacks (0.525 Å/pixel) were motion-corrected with MotionCorr2 [70]. Each frame in the image stack was divided into 5x5 patches for anisotropic image motion. The parameters of the contrast transfer function (CTF) were estimated by CTFFIND4 [72].

Following the motion correction, the liposome contribution was removed with a model based on the average POPC membrane profile as described in Chapter 4. Then, approximately 5,000 particles from 350 images were manually selected to generate templates representing different views for automated particle selection. The autopicked particles were manually inspected to

remove false positives, resulting in approximately 275,295 particles from 2,786 micrographs. Then 122,456 of the 275,295 particles classified into high-abundance classes were then subjected to the RELION 3D classification algorithm using the initial model, resulting in one major class with 113,000 particles.

Table 5.1 Data collection conditions

Condition	**Detail**
TEM	FEI Titan Krios
Detector	Gatan K2 Summit
Pixel Size	0.525 A/super-resolution pixel
Energy filter	20 eV
Dose	62 e/ $Å^2$
Dose rate	7.2 e/pixel/s
Exposure time	8.6 s
Image	2,786
Particles Autopicked	275,295
Particles for 3D classification	122,456
Particles for final reconstruction	114,362

5.2.2 2D Classification

Ideally, a 3D reconstruction would contain an entire proteoliposome. Unfortunately the variability of liposome size precludes the merging of their images as shown in Figure 2.10 (see page 27); instead we fitted and subtracted a model[71] of the membrane contribution to each image. The resulting liposome-subtracted protein particles were classified using RELION[73]. Some structural details were visible in the 2D classes (see Figure 5.1). The presence of lipid membrane was confirmed in the 2D classes from original cryo-EM images using the orientation information determined with liposome-subtracted images.

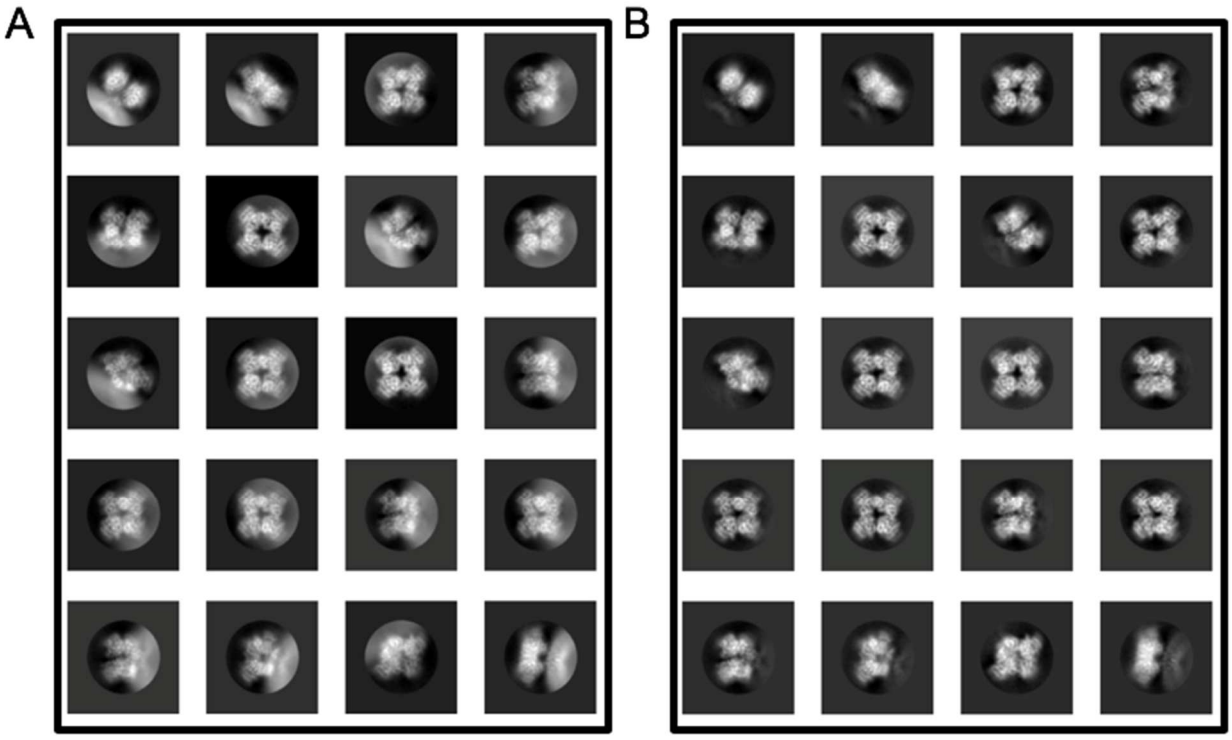

Figure 5.1 2D classification of BK proteoliposomes (A) 2D class averages before vesicle subtraction. (D) 2D class averages after vesicle subtraction. Box size is 27 nm, and the circular mask is 17 nm in diameter.

5.2.3 Symmetry

The reconstruction of BK structure was carried out without symmetry employed at first.

Surprisingly, a two-fold rotational symmetry was observed (Figure 5.3). Rotational symmetry Cn

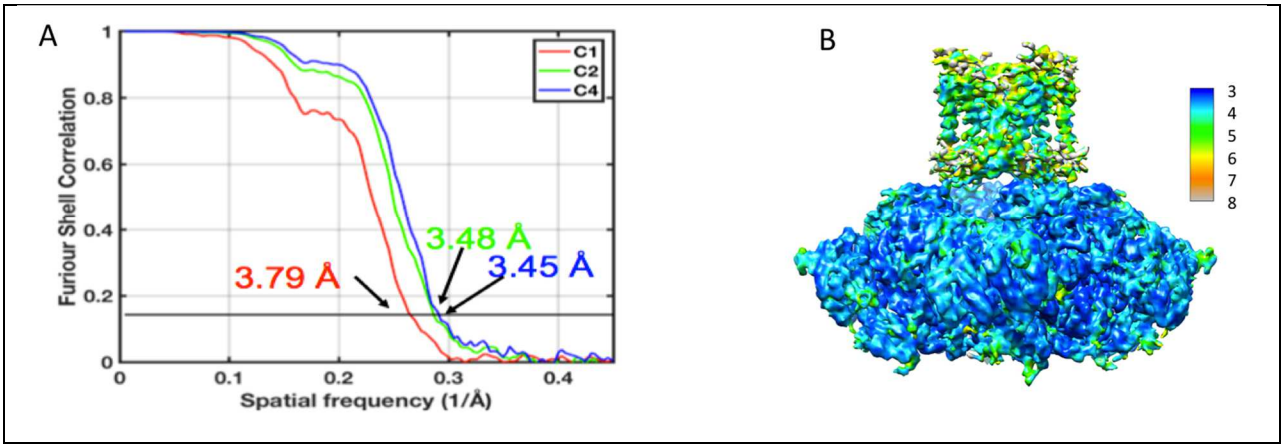

Figure 5.2 Resolution of hBK maps. (A) Fourier shell correlation curve with C1, C2 and C4 symmetry imposed. (B) Local resolution with C2 symmetry imposed calculated from ResMap[74].

means a shape looks the same when it is rotated by 360/n degree. The resolution of determined EM density map increased from 3.79 Å to 3.48 Å when a C2 was imposed. However, the resolution only changed a little (from 3.48 Å to 3.45 Å) when a C4 was imposed. This supports the presence of a C2 symmetry instead of a C4 symmetry.

Due to the rotational flexibility of the transmembrane (TM) domain as observed in aSlo1 in EDTA[13], the TM helices will be displaced depending on the distance to the ion-conducting pore. Thus only Helices S5, S6 and pore domain was determined with the gating ring to high resolution with C2 symmetry as shown in Figure 5.4.A.

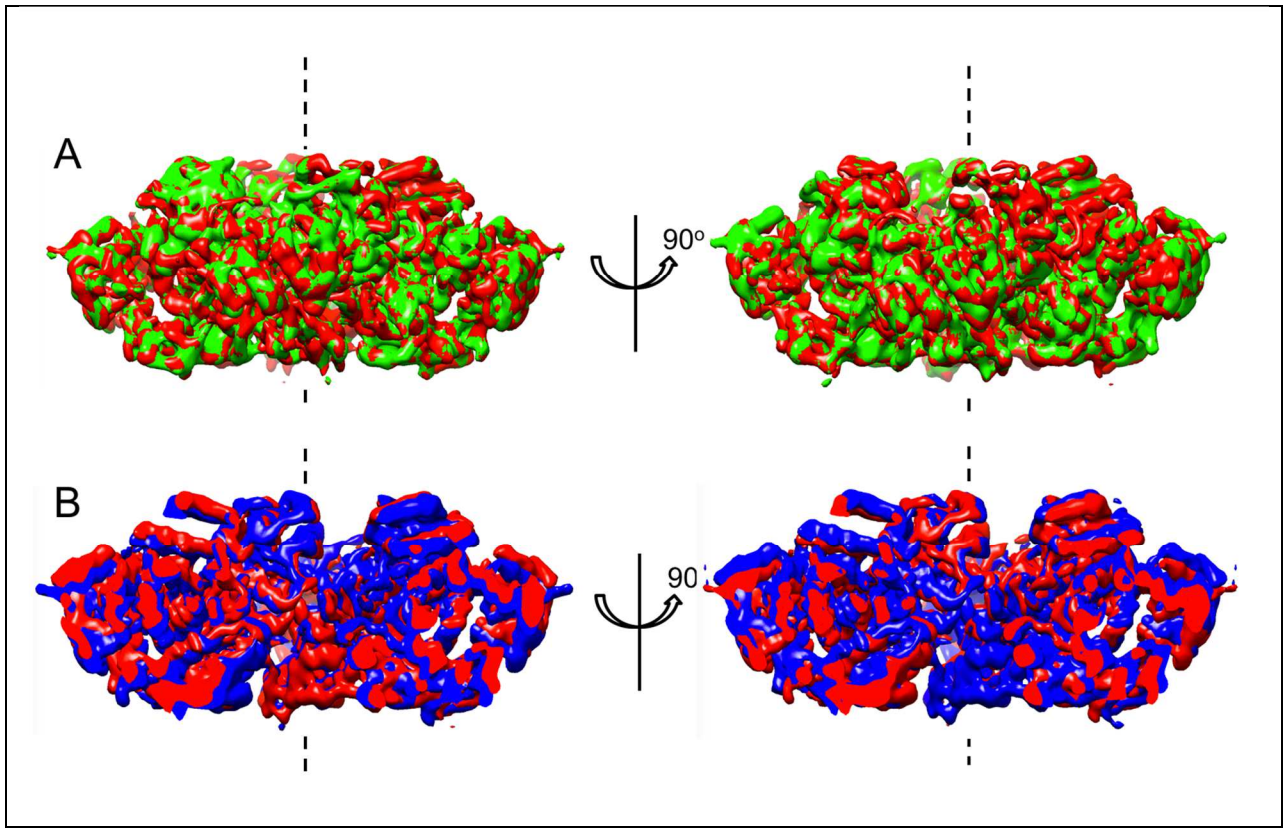

Figure 5.3 Comparison of hBK structure with C1 and C2 symmetry imposed. (A) Side views of hBK C2 structure (red) and hBK C1 structure (green) (B) Side views of hBK C2 structure (red) overlaid with the same structure turned by 90°(blue). Rotation axis is shown as the dashed line.

5.2.4 Gating Ring

In the C2 symmetry structure, the central opening of the gating ring defined as the distance between C_α atoms of Val 785 in opposing subunits differs by 2.7 Å in two directions (see Figure 5.4.B). The shoulder helix J moves by about 5 Å from two opposing subunits, termed as hBK High, to the other two opposing subunits, termed as hBK Low.

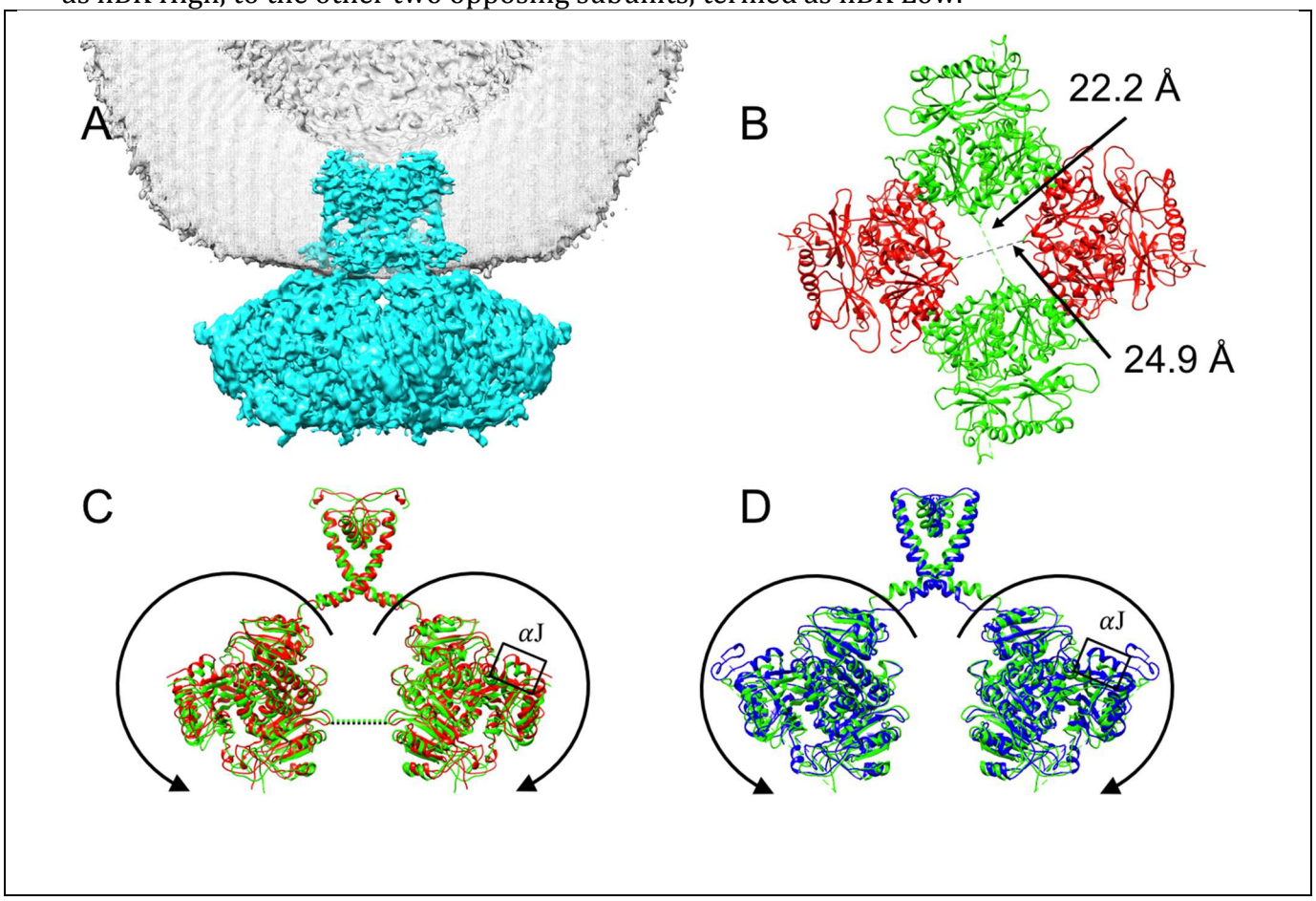

Figure 5.4 The structure of hBK in liposomes. (A) hBK cryo-EM density map. Lipid membrane is shown in mesh. For clarity, only half of the lipid membrane is shown. (B) Intracellular view of the gating ring in hBK. hBK High and Low are shown in red and green, respectively. The diagonal distances between the C_α atoms of the Val 785 are indicated. (C) Superposition of hBK High (red) and Low (green) subunits (red). The circular arrows mark the relative movement from hBK High to Low subunits. (D) Superposition of hBK Low (green) subunits and two opposing subunits in ligand-free aSlo1 (blue, PDB: 5tji[13]). The circular black arrows mark the major movement from ligand-free aSlo1 to hBK Low subunits.

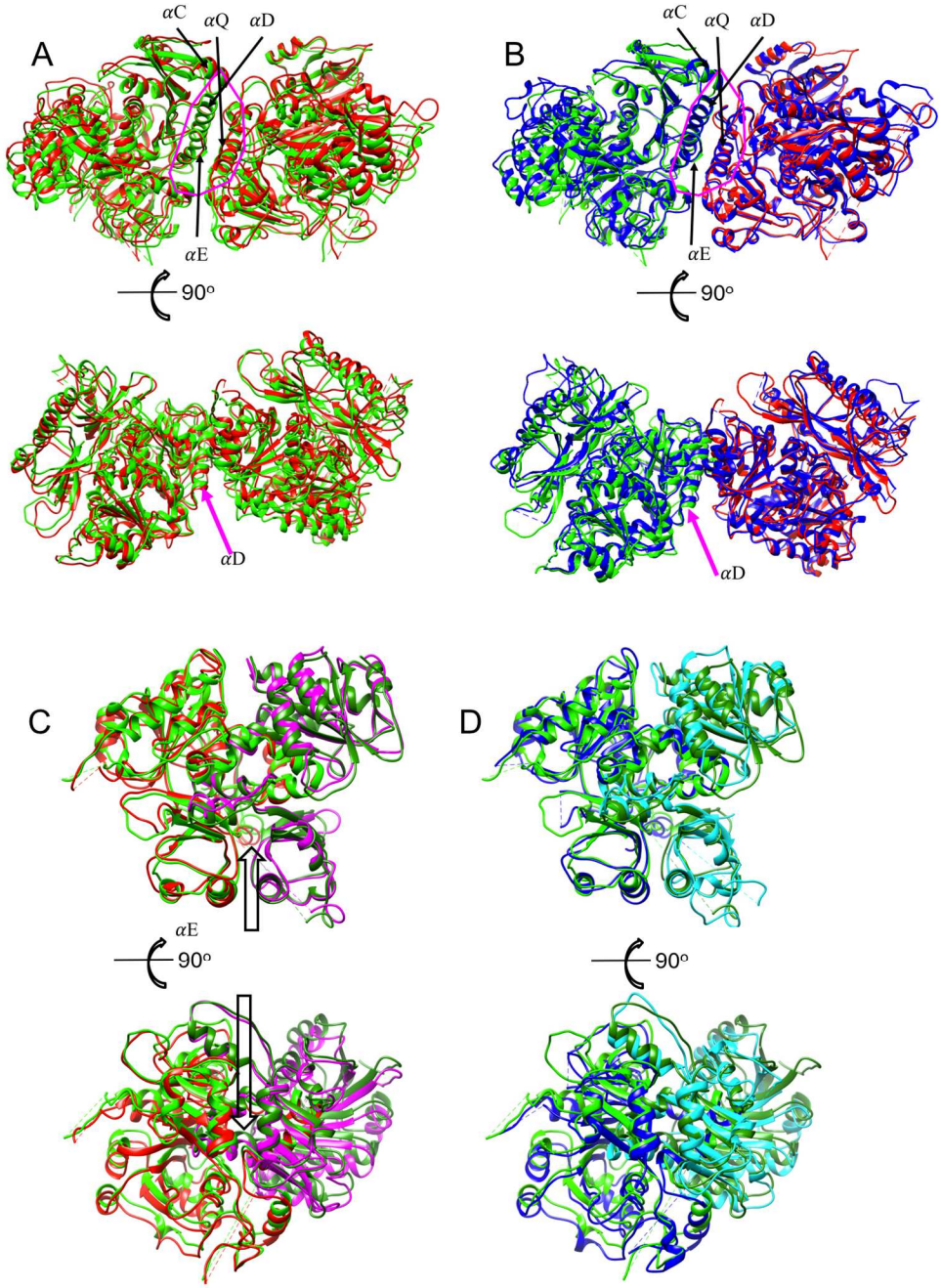

Figure 5.5 Ribbon representations of assembly and flexible interfaces (A) Superposition of the assembly interfaces formed between hBK High (red) and Low (green) subunits and between hBK Low and High subunits (B) Superposition of the assembly interfaces formed between hBK Low (green) and High (red) subunits and two opposing subunits in ligand-free aSlo1. (C) Superposition of the flexible interfaces between RCK1 and RCK2 in hBK High (RCK1: magenta and RCK2: red) and Low (RCK1: dark green and RCK2: green). (D) Superposition of the flexible interfaces between RCK1 and RCK2 in hBK Low (RCK1: dark green and RCK2: green) and in ligand-free aSlo1 (RCK1: cyan and RCK2: blue).

The two opposing hBK Low subunits rotates around the center of mass: the top N-lobe open like the petals of a flower, the middle shoulder helix (αJ) moves downward about 5 Å (see Figure 5.4.C), and the bottom C-terminus moves toward the central 2-fold symmetry axis. This movement is comparable to the movement of the gating ring between the ligand-free and liganded aSlo1 structures: the ligand-free gating ring moves ~5 Å away from the TM region. To accommodate the movement of hBK Low subunits, the assembly interface between the Low and High subunits moves inward toward the central symmetry axis by about 2 Å (see Figure 5.5.A&B). However, the conformation of the assembly interfaces was maintained: the assembly interface between the High and Low neighboring subunits is similar to that between Low and High subunits, and is similar to that in ligand-free aSlo1. On the contrary, the flexible interface between RCK1 and RCK2 domains in hBK High differs from that in hBK Low subunits (Figure 5.5.C) and that in ligand-free aSlo1 (Figure 5.5.D). In short, the assembly interface moves as a rigid body while the flexible interface deforms to accommodate the conformational difference between hBK High and Low subunits.

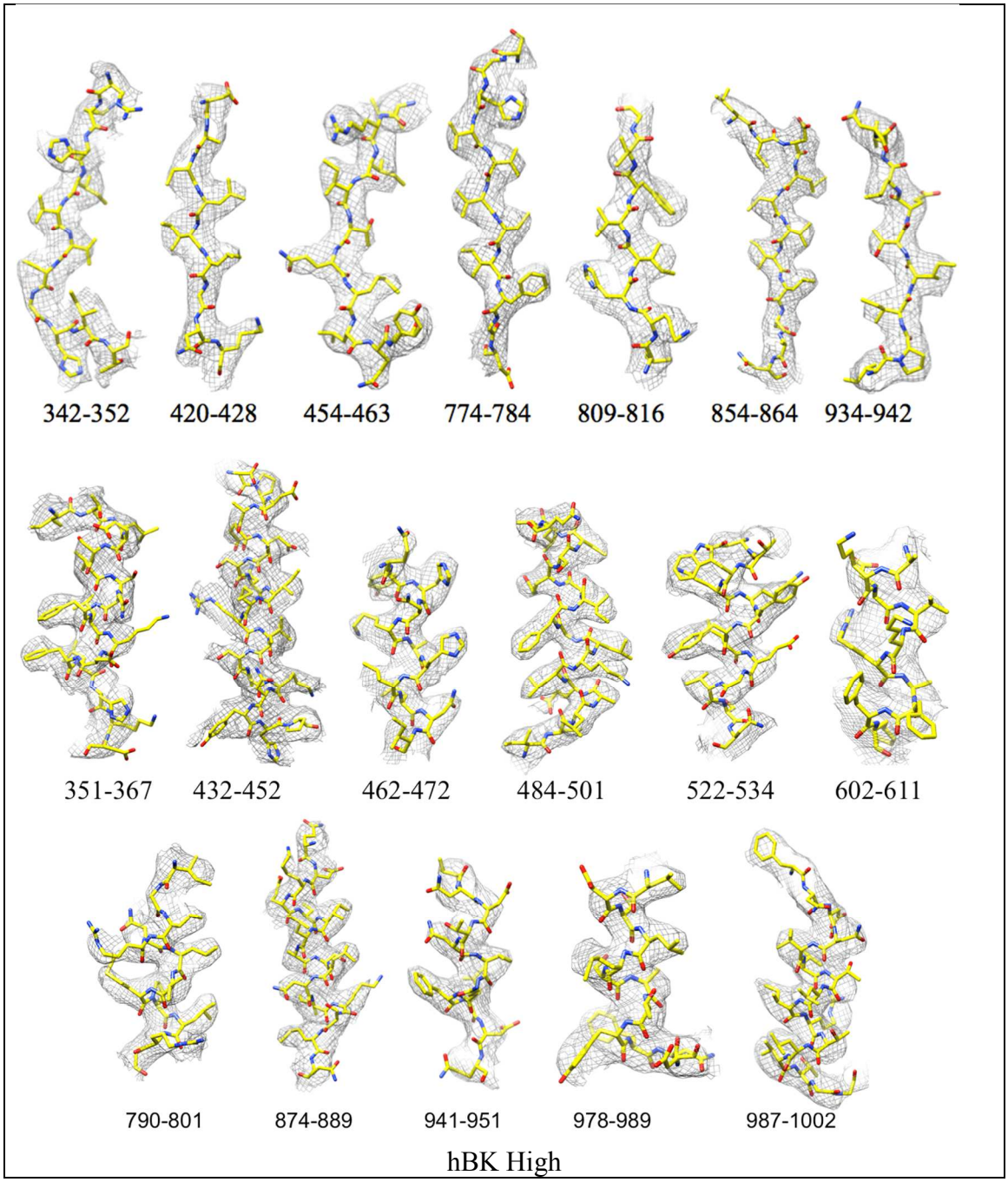
342-352
420-428
454-463
774-784
809-816
854-864
934-942
351-367
432-452
462-472
484-501
522-534
602-611
790-801
874-889
941-951
978-989
987-1002

hBK High

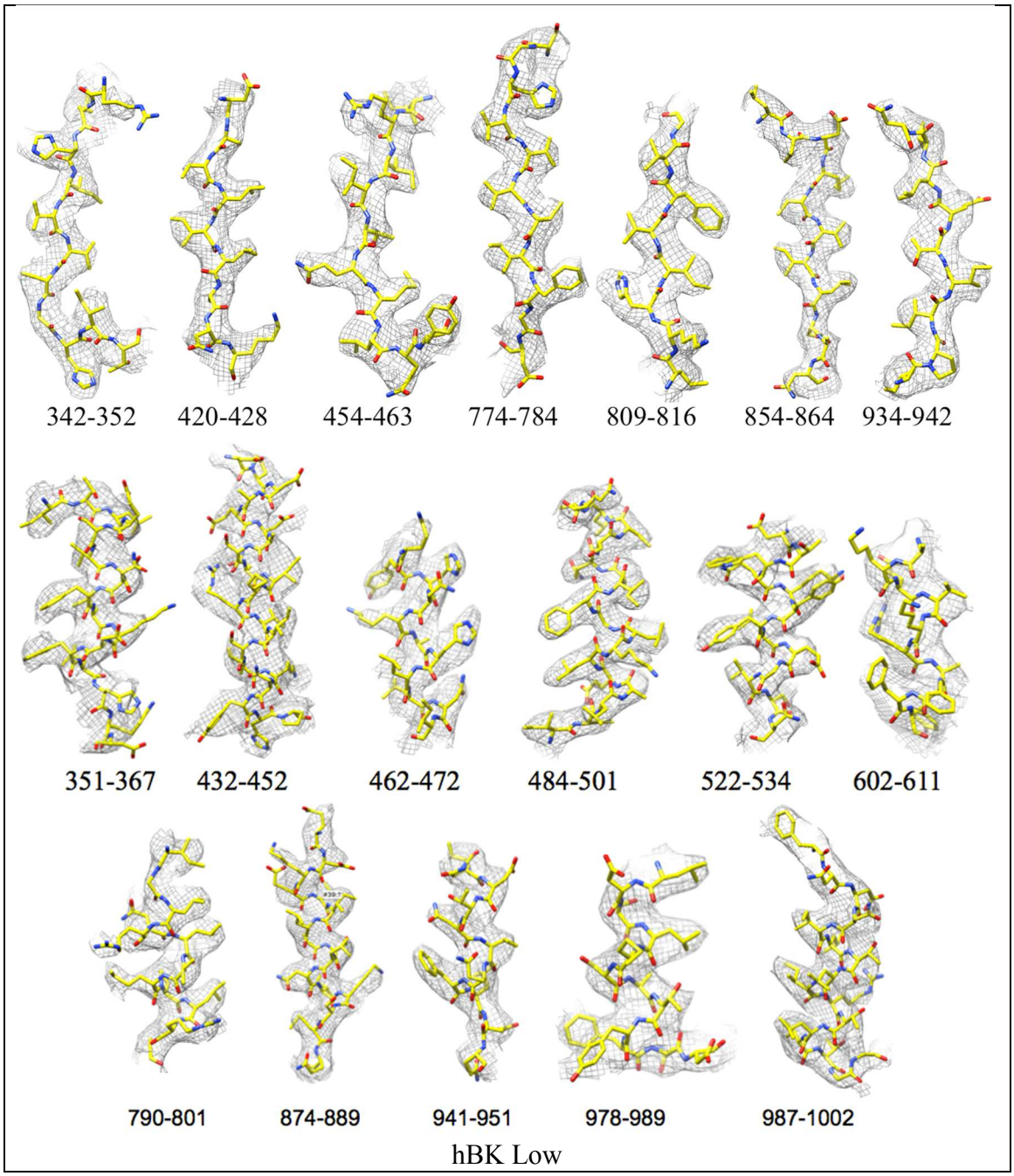

Figure 5.6 Representative segments of cryo-EM density in the gating ring. Numbers are the residue numbers in human BK.

5.2.5 Calcium-binding sites

In the absence of calcium, the gating ring in hBK was expected to be in a loose conformation as observed in ligand-free aSlo1 and adopts a four-fold symmetry. Surprisingly, the conformation in

ligand-free hBK is different: it adopts a two-fold symmetry (see Figure 5.4.B). The Ca^{2+} bowl adopts a similar conformation as seen in ligand-free aSlo1. As these sites are near the assembly interface, the Ca^{2+} bowl in hBK Low subunit near the High and Low interface situated at the same position, while the Ca^{2+} bowl in hBK High subunit near the Low and High interface moves inward with the assembly interface. The second high-affinity Ca^{2+} binding site in RCK1 in hBK High adopts a similar conformation as in ligand-free aSlo1. As G523 in aSlo1 is replaced by S533 in hBK, the distances to the side chain of S533 were about 3 Å shorter that those to the

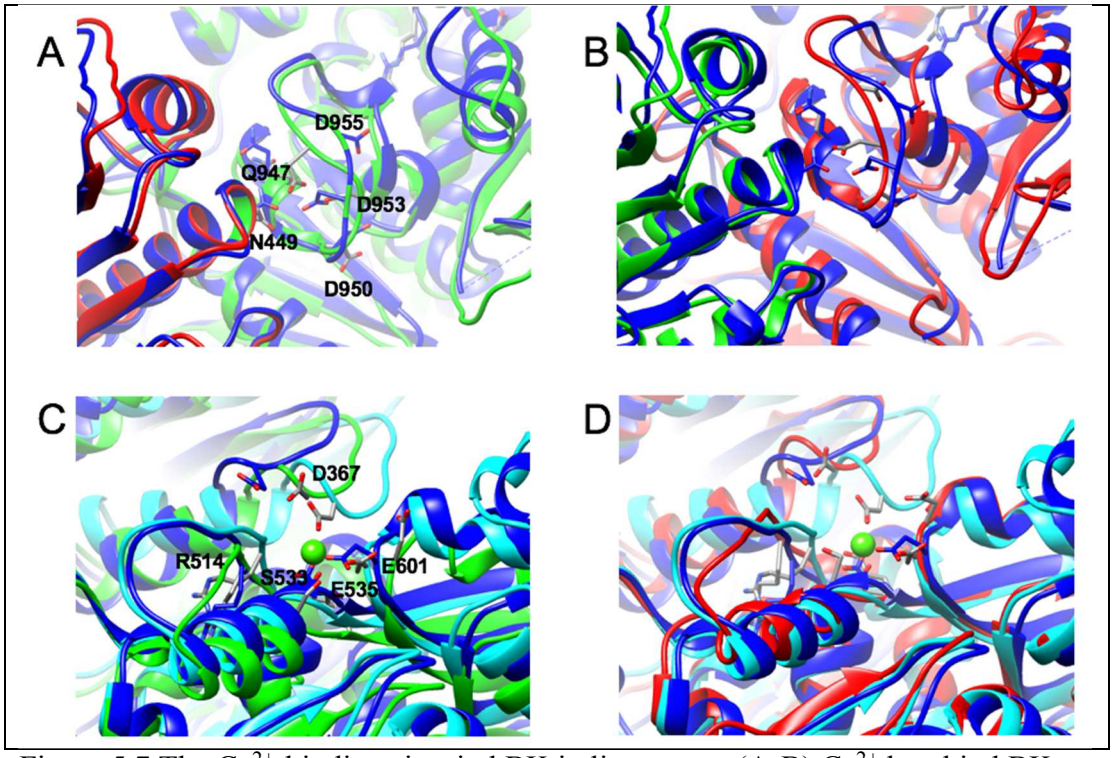

Figure 5.7 The Ca^{2+}-binding sites in hBK in liposomes. (A-B) Ca^{2+} bowl in hBK Low (green) and High (red) subunits. For comparison, ligand-free aSlo1 (blue, PDB: 5tji) is superimposed. The Ca^{2+} binding residues, N449, D950, D953, D955, and Q947 (N438, D902, D905, D907, Q899 in aSlo1), are labeled. (C-D) RCK1 Ca^{2+}-binding site in hBK Low (green) and High (red) subunits. For comparison, ligand-free aSlo1 (blue) and liganded aSlo1 (cyan) is superimposed and green spheres represent Ca^{2+} ions. The Ca^{2+} binding residues, R514, S533, E601, D367, and E535 (R503, G523, E591, D356, E525 in aSlo1), are labeled.

backbone carbonyl of S533. This suggests that the side chain of S533 instead of the backbone carbonyl may contribute to Ca^{2+} binding. Due to the movement of the hBK Low subunit, the

RCK1 Ca^{2+}-binding site in hBK Low moves outward by ~3 Å. However, the conformation is the same as that in hBK High. In short, the RCK1 Ca^{2+}-binding sites adopts a similar conformation in hBK High and Low subunits and move as a rigid body.

5.2.6 TM region

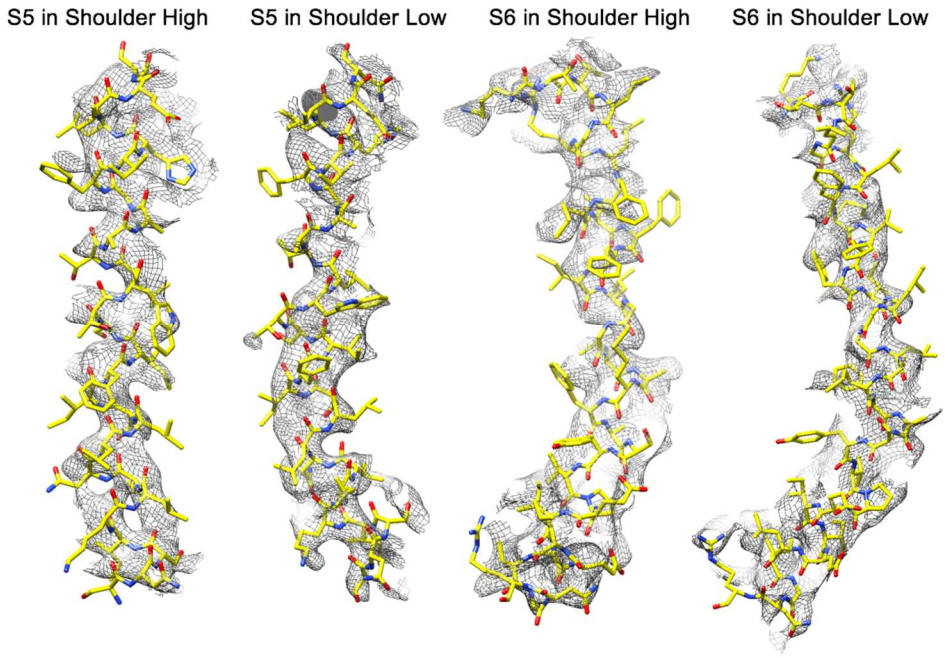

Figure 5.8 Cryo-EM density map superimposed with model for S5 and S6 with C2 symmetry.

Due to the rotational flexibility of the transmembrane (TM) domain as observed in ligand-free aSlo1[13], helices S0-S4 cannot be well resolved in the EM density map with a C2 symmetry. Therefore, a C4 symmetry was applied. The transmembrane region of hBK, containing the pore domains and VSDs is expected to be similar to that seen in ligand-free aSlo1. In ligand-free aSlo1, the TM region was flexible, and an 8-degree rotation about the central four-fold axis of the channel was observed among the four EM density maps. When reconstituted in liposomes, the TM region of hBK rotates 4 degrees further (i.e. the TM region rotates by 12 degrees clockwise compared with that in aSlo1) as shown in Figure 5.10. The helix S0 observed in ligand-free aSlo1 is not visible in hBK as it is the furthest to the central four-fold axis (the signal

of helix S0 in ligand-free aSlo1 is also much weaker than the rest of the TM helices). As shown in Figure 5.10.A, the VSD in ligand-free aSlo1is more compact compared with that in hBK in liposomes. As the lipid membrane in liposome is fluidic, the protein has more flexibility, thus the VSDs adopt a more extended conformation in my study.

Upon rotating the aSlo1 TM region by 12 degrees, the pore domain of aSlo1 overlapped with that of hBK (Figure 5.10.B). As this pore domain is closer to the central four-fold axis of the channel and experience less blurring, the intensity is much stronger that the intensity in the VSD regions. Thus, the pore domain is visible in the reconstruction with a C2 symmetry. The intracellular helix bundle crossing of hBK forms a parallelogram instead of a square in aSlo1 (Figure 5.10.C, D&E). This is due to the movement of the RCK domains in the gating ring region (Figure 5.4.C). As the signal in the TM region was decreased by the subtraction of lipid membrane densities, the signal is not strong enough for 3D classification. Thus only the positions of the helices S1 to S4 were determined.

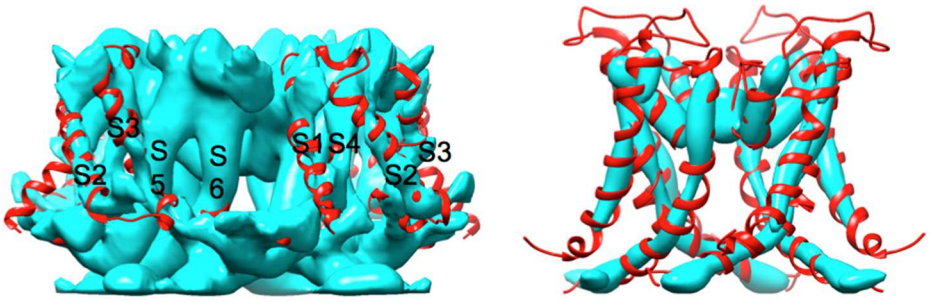

Figure 5.9 TM region of hBK with the model built in Phenix[75]. (A) TM region of hBK at low contour level. (B) The pore domain of hBK.

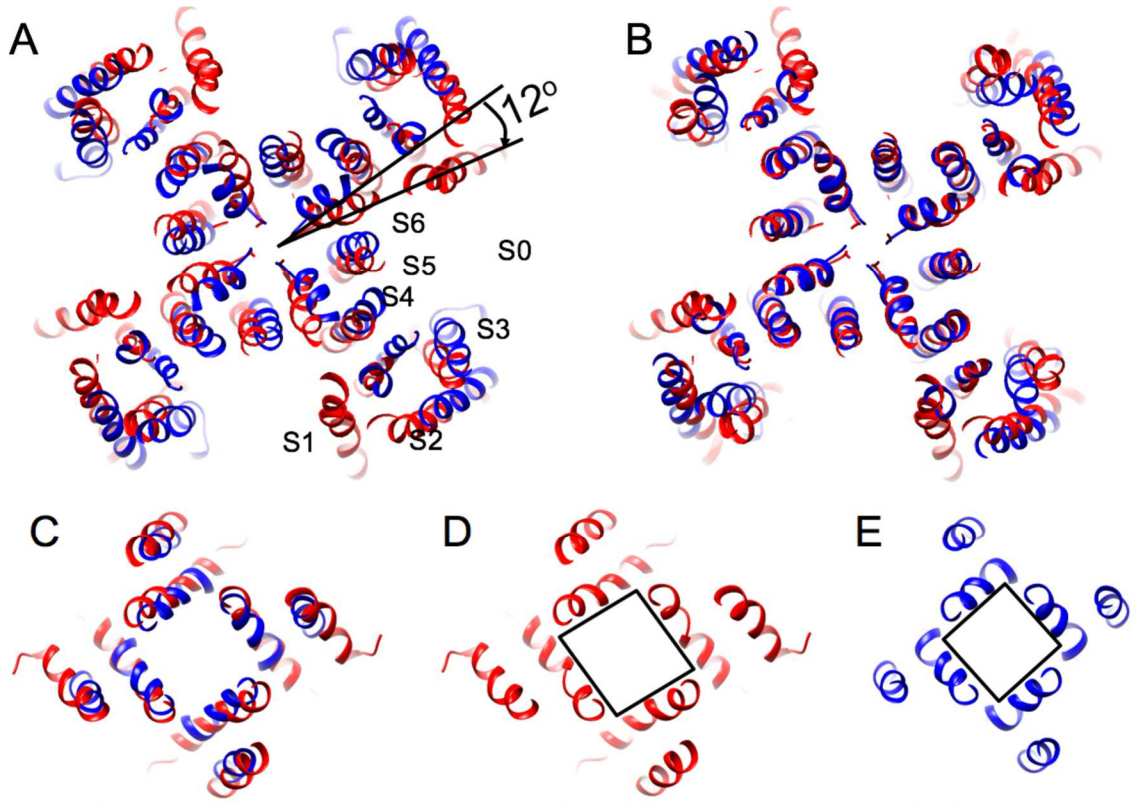

Figure 5.10 Comparison of the TM region in hBK and aSlo1. (A) The TM region in hBK (red) is rotated by 12 degrees clockwise with respect to that of aSlo1 (blue). (B) aSlo1 was rotated by 12 degrees to overlay with hBK. (C) Superposition of the intracellular helix bundle crossing region of hBK(red) and aSlo1(blue) (D&E) the intracellular helix bundle crossing region of hBK and aSlo1. Note: all views are extracellular views.

5.2.7 Effects of membrane curvature

The proteoliposomes used for structure determination ranged from 15 to 70 nm in diameter (Figure. 2.10, see page 27). The question therefore arises, whether the membrane curvature in vesicles of different sizes would affect the observed BK structure, especially the C2 symmetry. To address this question, three BK structures were reconstructed from small (15-19 nm), intermediate (19-25 nm) and large (25-70 nm) BK proteoliposomes respectively (Table 5.2). The gating ring region agrees well in the three reconstructions, and all show the C2 symmetry. A parallel reconstruction performed using the same angle assignments but with the liposome

information unsubtracted particle images, illustrates the curved membrane as Figure 5.11 shown. For examination of the TM region, C4 symmetry was applied as discussed before to get the position and VSD helixes then C2 symmetry was applied to assess the curvature effect on electron density (Figure 5.10.B). The reconstructions from BK reconstituted in intermediate and large liposomes show similar VSD helices in addition to the pore region as that in the reconstructions from BK reconstituted in all the liposomes. The pore region in the reconstruction from BK reconstituted from small liposomes agrees well with other reconstructions, but the VSD region is much noisier. Thus the membrane curvature only affects the VSD region when the liposomes are smaller than 19 nm.

Table 5.2 TM region in different size of liposomes

group	#particles	Mean (std) of radius	Resolution (C2)
small	40,574	8.0nm(0.7nm)	4.05A
medium	40,669	10.5nm(0.8nm)	4.05A
large	41,213	16.0nm(4.2nm)	4.15A
all	122,456	11.5nm(4.2nm)	3.86A

As shown by the structure of TRPV1 in nanodiscs[76],KV1.2[77], the tightly bound lipid molecules rearrange themselves to accommodate the structure of the protein. The lipid headgroups may move close to the bilayer center compared with an averaged lipid membrane. As the membrane profile used for vesicle subtraction has peaks in lipid headgroup regions and a dip at the bilayer center (see Figure 4.14.D, page 56), in that case, there would be a residue near the bilayer center, whereas there would be over-subtraction in the regular headgroup regions. Thus the leftover density due to the vesicle subtraction should be only shown near the bilayer center, and should be shorter than 10 Å. However, the helix S0 density observed in the EM map is even longer than the membrane thickness. Therefore, the helix S0 density is not due to the artifact from the vesicle subtraction.

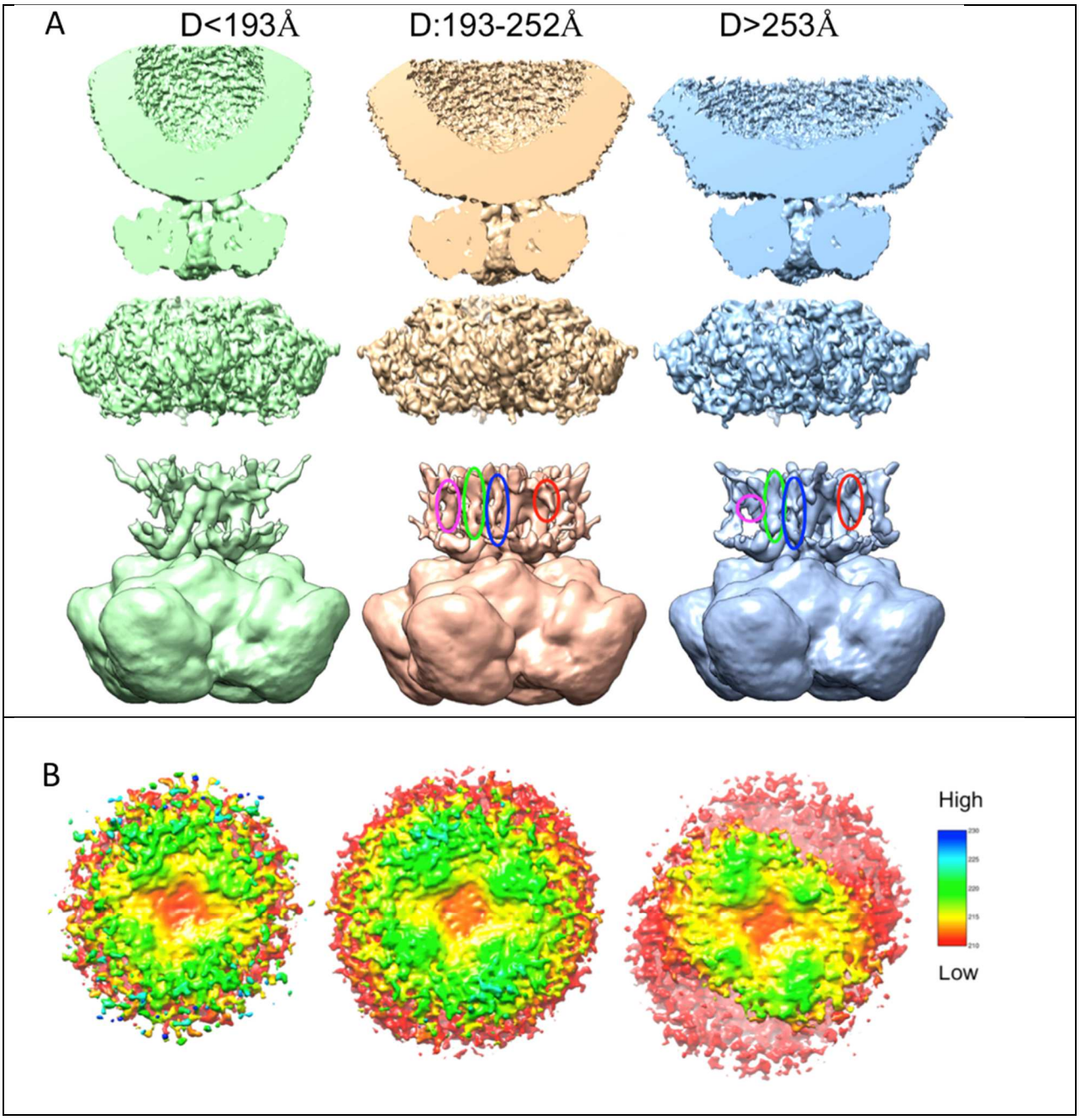

Figure 5.11 Effect of liposome size on BK structure. (A) Top row: cutaway views of BK in liposomes. Middle row: gating ring of BK. Bottom row: 3D view of BK with TM helices marked. Red, green, blue and magenta ellipses mark helices S1 to S4, respectively. (B) electron density of TM region for BK in small, intermediate and large liposomes.

5.2.8 Conclusions

Here, we reconstituted hBK (KCNMA1) channels into liposomes. As a first step, the transmembrane potential was set to zero (i.e. no transmembrane potential) and no ligand (Ca^{2+})

was present. Surprisingly, the ligand-free hBK was trapped in a state, different from the structure of ligand-free aSlo1 in detergents. The structure of hBK shows a two-fold symmetry instead of a common four-fold symmetry observed in other K^+ channels. Half of the assembly interfaces and the Ca^{2+} binding sites in the gating ring move with respect to the other half interfaces and Ca^{2+} binding sites in hBK and those in ligand-free aSlo1. The flexible interfaces between RCK1 and RCK2 domains differ in hBK High and Low subunits to accommodate the movement of the hBK Low subunits. Despite of the movements of interfaces, the local conformation of the interfaces and Ca^{2+} binding sites remains the same in all four subunits. As for the TM region, a large rotation (12^o counter clockwise) with respect to the gating ring is observed in hBK and overall TM adopts a more extended arrangement.

5.3 Materials and Methods

Software packages MATLAB 2015b (MathWorks, Natick, MA), RELION (REgularised Likelihood OptimisatioN) (MRC, UK) and CryoSPARC (STRUCTURA, CA) were used to process the motion-corrected images.

5.3.1 CTF estimation

The parameters of the contrast transfer function were estimated by CTFFIND4 [72].

5.3.2 Particles Autopicking

Images with vesicles subtracted were used for Autopicking in RELION. Around 10 class averages from manual-picked particles were used as autopicking templates. . The automated picked particles were screened using homemade MATLAB (MathWorks) programs to exclude particles more than 80 Å away from any liposome, which resulted in 275,295 particles from 2,786 micrographs.

5.3.3 Classification using RELION

The goal in 2D classification here is to only eliminate ice particles or unsubtracted lipid vesicles. To do that, two parallel runs of RELION 2D classification were carried out for the autopicked particles with 100 classes and 170 Å mask and 25 rounds of iterations. After selection of good classes from each run, the selections were combined and one copy of duplicated particles was eliminated. One more round of 2D cleaning was followed before going through 3D classification. In 3D classification, the electron density map from aSlo1[22] was filtered to 60 Å and used as the initial model. Two parallel runs of 3D classification with either C4 or C1 symmetry were carried out with 6 groups.

5.3.4 Reconstruction using RELION

Particles from the selection of 3D classification were given C1/C2/C4 symmetry for RELION autorefine with aSlo1[22] electron density map filtered to 60 Å as initial model and 200 Å mask. The reconstructed map was sharpened using RELION Postprocessing with auto B factor determination. To show the position of the membrane, the particle stack was replaced with the stack extracted from non-liposome-subtracted micrographs using RELION.

5.3.5 Reconstruction using cryoSPARC

Particles and image stack from the selection of 3D classification from RELION was given C1/C2/C4 symmetry for cryoPARC homogeneous Refinement.

5.3.6 Model building

The initial model of hBK was predicted using SWISS-MODEL[78]. Then the structure was docked into the EM map, and flexible loops were removed manually using UCSF Chimera[7]. Then a mask extending by 3 pixels and with a soft edge of 8 pixels was created in RELION, and applied

to the EM map. The masked EM map was using for flexible fitting using MDFF [79] with a C2 symmetry. The refined structure was further refined in real space using phenix.real_space_refine[75]. Geometric and secondary structure restraints were tightly maintained throughout refinement to minimize over fitting.

Bibliography

1 <http://blanco.biomol.uci.edu/mpstruc> (

2 Doerr, A. Membrane protein structures. *Nature Methods* **6**, 35, doi:10.1038/nmeth.f.240 (2008).

3 Miller, C. Ion channels: doing hard chemistry with hard ions. *Curr Opin Chem Biol* **4**, doi:10.1016/S1367-5931(99)00068-X (2000).

4 Armstrong, C. M. & Hille, B. Voltage-Gated Ion Channels and Electrical Excitability. *Neuron* **20**, 371-380, doi:https://doi.org/10.1016/S0896-6273(00)80981-2 (1998).

5 Doyle, D. A. *et al.* The Structure of the Potassium Channel: Molecular Basis of K+ Conduction and Selectivity. *Science* **280**, 69 (1998).

6 Coetzee William, A. *et al.* Molecular Diversity of K+ Channels. *Annals of the New York Academy of Sciences* **868**, 233-255, doi:10.1111/j.1749-6632.1999.tb11293.x (2006).

7 Pettersen, E. F. *et al.* UCSF chimera - A visualization system for exploratory research and analysis. *J Comput Chem* **25**, 1605-1612 (2004).

8 Patel, A. J. & Honoré, E. Molecular physiology of oxygen-sensitive potassium channels. *European Respiratory Journal* **18**, 221 (2001).

9 Choe, S. Potassium channel structures. *Nature Reviews Neuroscience* **3**, 115, doi:10.1038/nrn727 (2002).

10 Ketchum, K. A., Joiner, W. J., Sellers, A. J., Kaczmarek, L. K. & Goldstein, S. A. N. A new family of outwardly rectifying potassium channel proteins with two pore domains in tandem. *Nature* **376**, 690, doi:10.1038/376690a0 (1995).

11 Whorton, M. R. & MacKinnon, R. Crystal Structure of the Mammalian GIRK2 K(+) Channel and Gating Regulation by G-Proteins, PIP(2) and Sodium. *Cell* **147**, 199-208, doi:10.1016/j.cell.2011.07.046 (2011).

12 Brohawn, S. G., del Mármol, J. & MacKinnon, R. Crystal Structure of the Human K2P TRAAK, a Lipid- and Mechano-Sensitive k+ Ion Channel. *Science* **335**, 436 (2012).

13 Hite, R. K., Tao, X. & MacKinnon, R. Structural basis for gating the high-conductance Ca2+-activated K+ channel. *Nature* **541**, 52, doi:10.1038/nature20775 (2016).

14 Wu, J. *et al.* Structure of the voltage-gated calcium channel Cav1.1 at 3.6 Å resolution. *Nature* **537**, 191, doi:10.1038/nature19321 https://www.nature.com/articles/nature19321 - supplementary-information (2016).

15 Kuang, Q., Purhonen, P. & Hebert, H. Structure of potassium channels. *Cellular and Molecular Life Sciences* **72**, 3677-3693, doi:10.1007/s00018-015-1948-5 (2015).

16 Wulff, H., Castle, N. A. & Pardo, L. A. Voltage-gated Potassium Channels as Therapeutic Drug Targets. *Nature reviews. Drug discovery* **8**, 982-1001, doi:10.1038/nrd2983 (2009).

17 Latorre, R. *et al.* Molecular Determinants of BK Channel Functional Diversity and Functioning. *Physiological Reviews* **97**, 39-87, doi:10.1152/physrev.00001.2016 (2016).

18 Cook, N. S. The pharmacology of potassium channels and their therapeutic potential. *Trends in Pharmacological Sciences* **9**, 21-28, doi:https://doi.org/10.1016/0165-6147(88)90238-6 (1988).

19 A. L. Hodgkin, F. R. S., A. F. Huxley. Propagation of electrical signals along giant nerve fibres. *Proceedings of the Royal Society of London. Series B - Biological Sciences* **140**, 177 (1952).
20 Kim, D. M. & Nimigean, C. M. Voltage-Gated Potassium Channels: A Structural Examination of Selectivity and Gating. *Cold Spring Harbor Perspectives in Biology* **8**, a029231, doi:10.1101/cshperspect.a029231 (2016).
21 Schwiening, C. J. A brief historical perspective: Hodgkin and Huxley. *The Journal of Physiology* **590**, 2571-2575, doi:10.1113/jphysiol.2012.230458 (2012).
22 Yellen, G. The voltage-gated potassium channels and their relatives. *Nature* **419**, 35, doi:10.1038/nature00978 (2002).
23 Bezanilla, F. The Voltage Sensor in Voltage-Dependent Ion Channels. *Physiological Reviews* **80**, 555-592, doi:10.1152/physrev.2000.80.2.555 (2000).
24 Ma, Z., Lou, X. J. & Horrigan, F. T. Role of Charged Residues in the S1–S4 Voltage Sensor of BK Channels. *The Journal of General Physiology* **127**, 309 (2006).
25 Pallotta, B. S., Magleby, K. L. & Barrett, J. N. Single channel recordings of Ca2+-activated K+ currents in rat muscle cell culture. *Nature* **293**, 471, doi:10.1038/293471a0 (1981).
26 Marty, A. Ca-dependent K channels with large unitary conductance in chromaffin cell membranes. *Nature* **291**, 497, doi:10.1038/291497a0 (1981).
27 Atkinson, N. S., Robertson, G. A. & Ganetzky, B. A component of calcium-activated potassium channels encoded by the Drosophila slo locus. *Science* **253**, 551 (1991).
28 Kaczmarek, L. K. *et al.* International Union of Basic and Clinical Pharmacology. C. Nomenclature and Properties of Calcium-Activated and Sodium-Activated Potassium Channels. *Pharmacological Reviews* **69**, 1 (2017).
29 Hite, R. K. *et al.* Cryo-electron microscopy structure of the Slo2.2 Na+-activated K+ channel. *Nature* **527**, 198, doi:10.1038/nature14958 (2015).
30 Hite, R. K. & MacKinnon, R. Structural Titration of Slo2.2, a Na+-Dependent K+ Channel. *Cell* **168**, 390-399.e311, doi:https://doi.org/10.1016/j.cell.2016.12.030 (2017).
31 Lee, C.-H. & MacKinnon, R. Activation mechanism of a human SK-calmodulin channel complex elucidated by cryo-EM structures. *Science* **360**, 508 (2018).
32 Jiang, Y., Pico, A., Cadene, M., Chait, B. T. & MacKinnon, R. Structure of the RCK Domain from the E. coli K+ Channel and Demonstration of Its Presence in the Human BK Channel. *Neuron* **29**, 593-601, doi:https://doi.org/10.1016/S0896-6273(01)00236-7 (2001).
33 Jiang, Y. *et al.* Crystal structure and mechanism of a calcium-gated potassium channel. *Nature* **417**, 515, doi:10.1038/417515a https://www.nature.com/articles/417515a - supplementary-information (2002).
34 Yuan, P., Leonetti, M. D., Pico, A. R., Hsiung, Y. & MacKinnon, R. Structure of the Human BK Channel Calcium-Activation Apparatus at 3.0 Å Resolution. *Science* **329**, 182 (2010).
35 Tao, X., Hite, R. K. & MacKinnon, R. Cryo-EM structure of the open high-conductance Ca2+-activated K+ channel. *Nature* **541**, 46, doi:10.1038/nature20608 (2016).
36 Cui, J., Yang, H. & Lee, U. S. Molecular mechanisms of BK channel activation. *Cellular and Molecular Life Sciences (CMLS)* **66**, 852-875 (2009).

37 Horrigan, F. T. & Aldrich, R. W. Coupling between voltage sensor activation, Ca2+ binding and channel opening in large conductance (BK) potassium channels. *J. Gen. Physiol.* **120**, 267-305 (2002).

38 Gribkoff, V. K., Starrett J.E, Jr. & Dworetzky, S. I. Maxi-K potassium channels: Form, function, and modulation of a class of endogenous regulators of intracellular calcium. *Neuroscientist* **7**, 166-177 (2001).

39 Jiang, Y. X. *et al.* Crystal structure and mechanism of a calcium-gated potassium channel. *Nature* **417**, 515-522 (2002).

40 Yuan, P., Leonetti, M. D., Hsiung, Y. & MacKinnon, R. Open structure of the Ca2+ gating ring in the high-conductance Ca2+-activated K+ channel. *Nature* **481**, 94-97, doi:http://www.nature.com/nature/journal/v481/n7379/abs/nature10670.html - supplementary-information (2012).

41 Wang, L. & Sigworth, F. J. Structure of the BK potassium channel in a lipid membrane from electron cryomicroscopy. *Nature* **461**, 292-295, doi:10.1038/nature08291 (2009).

42 Tanaka, J. C., Eccleston, J. F. & Barchi, R. L. Cation selectivity characteristics of the reconstituted voltage-dependent sodium channel purified from rat skeletal muscle sarcolemma. *Journal of Biological Chemistry* **258**, 7519-7526 (1983).

43 Su, Z., Brown, E. C., Wang, W. & MacKinnon, R. Novel cell-free high-throughput screening method for pharmacological tools targeting K+ channels. *Proceedings of the National Academy of Sciences* **113**, 5748 (2016).

44 Nakao, S., Ebata, H., Hamamoto, T., Kagawa, Y. & Hirata, H. SOLUBILIZATION AND RECONSTITUTION OF VOLTAGE-DEPENDENT CALCIUM-CHANNEL FROM BOVINE CARDIAC-MUSCLE - CA-2+ INFLUX ASSAY USING THE FLUORESCENT DYE QUIN2. *Biochimica Et Biophysica Acta* **944**, 337-343, doi:10.1016/0005-2736(88)90503-2 (1988).

45 Ramos-Franco, J. *et al.* Single-channel function of recombinant type 2 inositol 1,4,5-trisphosphate receptor. *Biophysical Journal* **79**, 1388-1399 (2000).

46 Jensen, K. H., Brandt, S. S., Shigematsu, H. & Sigworth, F. J. Statistical modeling and removal of lipid membrane projections for cryo-EM structure determination of reconstituted membrane proteins. *Journal of Structural Biology* **194**, 49-60, doi:https://doi.org/10.1016/j.jsb.2016.01.012 (2016).

47 Epstein, M. & Racker, E. Reconstitution of carbamylcholine-dependent sodium ion flux and desensitization of the acetylcholine receptor from Torpedo californica. *Journal of Biological Chemistry* **253**, 6660-6662 (1978).

48 Wang, L. & Tonggu, L. Membrane protein reconstitution for functional and structural studies. *Science China Life Sciences* **58**, 66-74, doi:10.1007/s11427-014-4769-0 (2015).

49 Rigaud, J.-L., Pitard, B. & Levy, D. Reconstitution of membrane proteins into liposomes: application to energy-transducing membrane proteins. *Biochimica et Biophysica Acta (BBA) - Bioenergetics* **1231**, 223-246, doi:https://doi.org/10.1016/0005-2728(95)00091-V (1995).

50 Schmidt, D., Jiang, Q. X. & MacKinnon, R. Phospholipids and the origin of cationic gating charges in voltage sensors. *Nature* **444**, 775-779 (2006).

51 Gonen, T. *et al.* Lipid-protein interactions in double-layered two-dimensional AQP0 crystals. *Nature* **438**, 633-638 (2005).

52 Long, S. B., Tao, X., Campbell, E. B. & MacKinnon, R. Atomic structure of a voltage-dependent K^+ channel in a lipid membrane-like environment. *Nature* **450**, 376-383 (2007).

53 Hilgemann, D. W. Getting ready for the decade of the lipids. *Annu. Rev. Physiol.* **65**, 697-700, doi:10.1146/annurev.physiol.65.092101.142453 (2003).

54 Hille, B., Dickson, E. J., Kruse, M., Vivas, O. & Suh, B.-C. Phosphoinositides regulate ion channels. *Biochim. Biophys. Acta* **1851**, 844-856, doi:10.1016/j.bbalip.2014.09.010 (2015).

55 Lee, A. G. Biological membranes: the importance of molecular detail. *Trends Biochem. Sci.* **36**, 493-500, doi:10.1016/j.tibs.2011.06.007 (2011).

56 Miller, A. N. & Long, S. B. Crystal structure of the human two-pore domain potassium channel K2P1. *Science* **335**, 432-436, doi:10.1126/science.1213274 (2012).

57 Li, M., Tonggu, L., Tang, L. & Wang, L. Effects of N-glycosylation on hyperpolarization-activated cyclic nucleotide-gated (HCN) channels. *Biochem. J.* **466**, 77-84, doi:10.1042/BJ20140692 (2015).

58 Qu, J., Altomare, C., Bucchi, A., DiFrancesco, D. & Robinson, R. B. Functional comparison of HCN isoforms expressed in ventricular and HEK 293 cells. *Pflügers Archiv* **444**, 597-601, doi:10.1007/s00424-002-0860-7 (2002).

59 Horrigan, F. T. & Aldrich, R. W. Coupling between Voltage Sensor Activation, Calcium Binding and Channel Opening in Large Conductance (BK) Potassium Channels. *The Journal of General Physiology* **120**, 267 (2002).

60 Lee, K.-D., Pitas, R. E. & Papahadjopoulos, D. Evidence that the scavenger receptor is not involved in the uptake of negatively charged liposomes by cells. *Biochimica et Biophysica Acta (BBA) - Biomembranes* **1111**, 1-6, doi:https://doi.org/10.1016/0005-2736(92)90267-P (1992).

61 Frederik, P. M. & Hubert, D. H. W. in *Methods in Enzymology* Vol. 391 431-448 (Academic Press, 2005).

62 Snijder, J. *et al.* Vitrification after multiple rounds of sample application and blotting improves particle density on cryo-electron microscopy grids. *Journal of Structural Biology* **198**, 38-42, doi:https://doi.org/10.1016/j.jsb.2017.02.008 (2017).

63 Wang, L., Ounjai, P. & Sigworth, F. J. Streptavidin crystals as nanostructured supports and image-calibration references for cryo-EM data collection. *Journal of structural biology* **164**, 190-198, doi:10.1016/j.jsb.2008.07.008 (2008).

64 Stagg, S. M. *et al.* Automated cryoEM data acquisition and analysis of 284742 particles of GroEL. *Journal of Structural Biology* **155**, 470-481, doi:https://doi.org/10.1016/j.jsb.2006.04.005 (2006).

65 Langmore, J. P. & Smith, M. F. Quantitative energy-filtered electron microscopy of biological molecules in ice. *Ultramicroscopy* **46**, 349-373, doi:10.1016/0304-3991(92)90024-E (1992).

66 Yonekura, K., Braunfeld, M. B., Maki-Yonekura, S. & Agard, D. A. Electron energy filtering significantly improves amplitude contrast of frozen-hydrated protein at 300 kV. *J. Struct. Biol.* **156**, 524-536, doi:http://dx.doi.org/10.1016/j.jsb.2006.07.016 (2006).

67 Yonekura, K., Maki-Yonekura, S. & Namba, K. Quantitative comparison of zero-loss and conventional electron diffraction from two-dimensional and thin three-dimensional protein crystals. *Biophys. J.* **82**, 2784-2797 (2002).

68 Angert, I., Burmester, C., Dinges, C., Rose, H. & Schröder, R. R. Elastic and inelastic scattering cross-sections of amorphous layers of carbon and vitrified ice. *Ultramicroscopy* **63**, 181-192, doi:10.1016/0304-3991(96)00036-8 (1996).

69 Feja, B. & Aebi, U. Determination of the inelastic mean free path of electrons in vitrified ice layers for on-line thickness measurements by zero-loss imaging. *J. Microsc.* **193**, 15-19, doi:10.1046/j.1365-2818.1999.00436.x (1999).

70 Zheng, S., Palovcak, E., Armache, J.-P., Cheng, Y. & Agard, D. Anisotropic Correction of Beam-induced Motion for Improved Single-particle Electron Cryo-microscopy. *bioRxiv*, doi:10.1101/061960 (2016).

71 Wang, L., Bose, P. S. & Sigworth, F. J. Using cryo-EM to measure the dipole potential of a lipid membrane. *PNAS* **103**, 18528-18533, doi:10.1073/pnas.0608714103 (2006).

72 Rohou, A. & Grigorieff, N. CTFFIND4: Fast and accurate defocus estimation from electron micrographs. *J. Struct. Biol.* **192**, 216-221, doi:https://doi.org/10.1016/j.jsb.2015.08.008 (2015).

73 Scheres, S. H. W. RELION: Implementation of a Bayesian approach to cryo-EM structure determination. *J. Struct. Biol.* **180**, 519-530, doi:dx.doi.org/10.1016/j.jsb.2012.09.006 (2012).

74 Kucukelbir, A., Sigworth, F. J. & Tagare, H. D. Quantifying the local resolution of cryo-EM density maps. *Nature Methods* **11**, 63, doi:10.1038/nmeth.2727 https://www.nature.com/articles/nmeth.2727 - supplementary-information (2013).

75 Adams, P. D. *et al.* PHENIX: a comprehensive Python-based system for macromolecular structure solution. *Acta Crystallographica Section D* **66**, 213-221, doi:doi:10.1107/S0907444909052925 (2010).

76 Gao, Y., Cao, E., Julius, D. & Cheng, Y. TRPV1 structures in nanodiscs reveal mechanisms of ligand and lipid action. *Nature* **534**, 347-351, doi:10.1038/nature17964 (2016).

77 Long, S. B., Tao, X., Campbell, E. B. & MacKinnon, R. Atomic structure of a voltage-dependent K+ channel in a lipid membrane-like environment. *Nature* **450**, 376, doi:10.1038/nature06265 (2007).

78 Waterhouse, A. *et al.* SWISS-MODEL: homology modelling of protein structures and complexes. *Nucleic Acids Res.* **46**, W296-W303, doi:10.1093/nar/gky427 (2018).

79 Trabuco, L. G., Villa, E., Schreiner, E., Harrison, C. B. & Schulten, K. Molecular dynamics flexible fitting: A practical guide to combine cryo-electron microscopy and X-ray crystallography. *Methods* **49**, 174-180, doi:10.1016/j.ymeth.2009.04.005 (2009).

VITA

Lige Tonggu was born in Beijing, the capital city of China. She studied Chemical Engineering and Industrial Bioengineering at Tsinghua University and earned a Bachelor of Science degree in 2011. After college, she moved to Seattle and studied under supervision of Dr. Hong Shen in the department of Chemical Engineering of the University of Washington and earned a Master's degree. She continued her graduate-school study under supervision of Dr. Liguo Wang in the department of Biological Structure. Her main research focus for graduate studies was the structure of potassium ion channels, and she gained extensive experience on mammalian cell culture, protein purification, cryo-EM sample preparation and data processing. In 2018, she earned a Doctor of Philosophy in Molecular and Cellular Biology in the University of Washington.